

May 2022

The Effects of an R103Q Mutation on the Chemical and Physical Properties of the Enzyme Cytochrome C Nitrite Reductase (ccNiR)

Shahama Alam
University of Wisconsin-Milwaukee

Follow this and additional works at: <https://dc.uwm.edu/etd>

 Part of the [Biochemistry Commons](#), and the [Chemistry Commons](#)

Recommended Citation

Alam, Shahama, "The Effects of an R103Q Mutation on the Chemical and Physical Properties of the Enzyme Cytochrome C Nitrite Reductase (ccNiR)" (2022). *Theses and Dissertations*. 2859.
<https://dc.uwm.edu/etd/2859>

This Dissertation is brought to you for free and open access by UWM Digital Commons. It has been accepted for inclusion in Theses and Dissertations by an authorized administrator of UWM Digital Commons. For more information, please contact scholarlycommunicationteam-group@uwm.edu.

THE EFFECTS OF AN R103Q MUTATION ON THE CHEMICAL AND
PHYSICAL PROPERTIES OF THE ENZYME CYTOCHROME C NITRITE
REDUCTASE (ccNiR)

by
Shahama Alam

A Dissertation Submitted in
Partial Fulfilment of the
Requirements for the Degree of

Doctor of Philosophy
in Chemistry

at
The University of Wisconsin-Milwaukee
May 2022

ABSTRACT

THE EFFECTS OF AN R103Q MUTATION ON THE CHEMICAL AND PHYSICAL PROPERTIES OF THE ENZYME CYTOCHROME C NITRITE REDUCTASE (ccNiR)

by

Shahama Alam

The University of Wisconsin-Milwaukee, 2022
Under the Supervision of Professor A. Andrew Pacheco

Cytochrome c Nitrite Reductase (ccNiR) is a periplasmic homodimeric decaheme enzyme that catalyzes the reduction of nitrite to ammonium in a process that involves six electrons and eight protons. The project described herein explored the properties of the *Shewanella oneidensis* R103Q ccNiR variant and compared them to the properties of the wild type enzyme. Under standard assay conditions, which use the strong reducing agent methyl viologen monocation radical (MV_{red}) as an electron source, the R103Q variant still catalyzes reduction of nitrite to ammonium, albeit with an MV_{red} turnover rate that is 20% of the wild type's ($780 \pm 50 \text{ s}^{-1}$ vs $4510 \pm 90 \text{ s}^{-1}$ for the wild type). Unlike the H257Q ccNiR variant described in an earlier study, R103Q's MV_{red} turnover rate was the same whether the electron-accepting substrate was nitrite or hydroxylamine (H257Q ccNiR's MV_{red} turnover rate is almost zero when nitrite is the electron acceptor but approaches that of the wild type when reducing hydroxylamine). The mechanistic implications of this observation are discussed.

Nitrite-loaded R103Q ccNiR's behavior under weakly reducing conditions differs substantially from that of the wild type, though it is still capable of catalyzing reduction of nitrite to nitric oxide when *N,N,N',N'*-tetramethyl-*p*-phenylenediamine (TMPD) or hexaammineruthenium(II) (Ru^{II}) is the electron donor (the nitric oxide turnover rate is higher

when the stronger Ru^{II} reductant is used). Regardless of the weak reductant used, a reduced R103Q ccNiR species with a characteristic UV/Vis absorbance spectrum is generated in an exponential process, with a half-life of about 30 minutes; the species is generated somewhat faster when pure Ru^{II} is the electron donor than when the weaker TMPD is used. A species with very similar UV/Vis spectra is seen when H257Q is reduced under mild conditions. On the other hand, when the nitrite-loaded wild type ccNiR is reduced under mild conditions (applied potentials above 0 mV vs SHE), the nitrite-loaded active site is converted to a species that has been identified as the 2-electron reduced {FeNO}⁷; this species has a substantially different UV/Vis spectrum from that obtained when R103Q or H257Q are reduced.

When 400 μ M pure Ru^{II} is used as the electron donor to reduce nitrite-loaded R103Q ccNiR, UV/Vis stopped-flow studies show that one of the bis-His ligated low-spin hemes is reduced on the millisecond timescale ($t_{0.5} \sim 20$ ms) and before the active site, which reduces with a half-life of about 1s to generate an active site species that is tentatively assigned as [Fe_{H1}^{II}(NO₂⁻)]; that is, a ferrous heme with nitrite as axial ligand. The remaining ferrous bis-His ligated heme is exponentially re-oxidized with a half-life of ~ 120 s, after which the active site slowly evolves to the species with distinctive UV/Vis spectrum described above. This species may be a non-catalytic form of the active site, in which case a major role of the residues R103 and H257 may be to prevent its formation.

TABLE OF CONTENTS

1. Introduction.....	1
1.1. The nitrogen cycle in respiration and environmental processes.....	1
1.2. Structural overview of cytochrome <i>c</i> nitrite reductase (ccNiR).....	5
1.3. Cytochrome <i>c</i> Nitrite reductase (ccNiR) reaction mechanism.....	8
1.3.1. Overview.....	8
1.3.2. Structural and computational analyses of the ccNiR mechanism.....	10
1.3.2.1. Nitrite activation at the ccNiR active site.....	10
1.3.2.2. The Possible Pathways for the First N–O Bond Cleavage.....	12
1.3.2.3. Heme iron-nitrosyl intermediates and the second N – O bond cleavage.....	14
1.3.3. Detection of catalytic intermediates under weakly reducing conditions.....	17
1.4. Specific objectives of this thesis.....	20
1.5. References.....	21
2. Purification and preliminary characterization of the ccNiR variant.....	25
2.1 Overview	25
2.2. Materials and Methods	25
2.2.1. General materials	25
2.2.2. General instrumentation.....	26
2.2.3. Overview of Transformation of the R103Q mutant plasmid into <i>S. Oneidensis</i> TSP cells.....	26
2.2.4. Large scale <i>S. oneidensis</i> ccNiR harvesting and purification for active site	

Variant R103Q from TSP-C cells	27
2.2.4.1. Bulk culture preparation and harvesting.....	27
2.2.4.2. Purification of wild type R103Q ccNiR from S. Oneidensis TSP-C cells..	28
2.2.5. The Pyridine Hemochrome assay	31
2.2.6. Methyl viologen assays of ccNiR nitrite reduction activity	32
2.2.7. Methyl viologen assays of ccNiR hydroxylamine reduction activity.....	33
2.3. Results.....	34
2.3.1. Pyridine Hemochrome assay determination of the R103QccNiR	
Extinction coefficient.....	34
2.3.2. Dependence on MV_{red} concentration of ccNiR-catalyzed reduction	
of nitrite by MV_{red}	40
2.3.3. Dependence on nitrite concentration of ccNiR-catalyzed reduction of	
nitrite by MV_{red}	42
2.3.4. Dependence on hydroxylamine concentration of ccNiR-catalyzed	
reduction of hydroxylamine by MV_{red}	42
2.4. Discussion	45
2.5. References.....	48
3. Electrochemical characterization of the R103Qccnir Variant and a comparative	
Study with wild type ccNiR.....	50
3.1. Overview.....	50
3.2 Materials and methods.....	50
3.2.1. General Materials.....	50

3.2.2. General instrumentation.....	51
3.2.3. UV/Visible Spectropotentiometric titrations of R103Q ccNiR in the Presence of the strong field ligand nitrite.....	51
3.3. Results	53
3.3.1. UV/Vis spectropotentiometric experiment with nitrite and mediators only.	53
3.3.2. UV/Vis spectropotentiometric experiments with <i>S. oneidensis</i> R103QccNiR.	58
3.4. Discussion	60
3.5. References	66
4. Reactivity of Nitrite-Loaded R103QccNiR with <i>N, N, N', N'</i>-tetramethyl-<i>p</i>-phenylenediamine (TMPD)	68
4.1. Overview.....	68
4.2. Materials and methods.....	69
4.2.1. General Materials.....	69
4.2.2. General instrumentation	69
4.2.3. Reduction of nitrite-loaded <i>S. oneidensis</i> R103QccNiR by TMPD	70
4.2.4. Catalase purification and handling.....	70
4.3. Results.....	71
4.3.1. Steady-state analysis of R103Q ccNiR-catalyzed reduction of nitrite by TMPD.....	71
4.3.2. NO [•] trapping experiments.....	78

4.4. Discussion.....	80
4.5. References.....	82
5. Reactivity of Nitrite-Loaded R103QccNiR with Hexaammineruthenium(II).....	84
5.1. Overview	84
5.2. Experimental procedures	85
5.2.1. General materials.....	85
5.2.2. Buffer and stock solution preparation.....	85
5.2.3. Reduction of nitrite loaded R103Q ccNiR by hexaammineruthenium(II)....	86
5.2.3.1. Long timescale kinetics experiments.....	86
5.2.3.2. stopped-flow experiments.....	86
5.3. Results.....	88
5.3.1. Reactivity of nitrite loaded R103Q ccNiR with pure hexaammineruthenium(II) on the time scale of hours.....	88
5.3.2. Stopped-flow investigation of nitrite-loaded R103Q ccNiR's reactivity with pure hexaammineruthenium(II).....	95
5.3.3. Reactivity of nitrite-loaded R103Q ccNiR with 1:1 Ru ^{II} :Ru ^{III} on the time scale of hours.....	99
5.4. Discussion.....	103

5.5 References.....	106
6. Conclusion and Suggestions for Further Study.....	107
References.....	111

LIST OF FIGURES

Figure 1.1. The various steps of the biochemical nitrogen cycle. Dinitrogen fixation, yellow arrow; assimilatory ammonification, orange arrows; organic nitrogen pools, pink arrows; denitrification, blue arrows; dissimilatory nitrate reduction to ammonium (DNRA), green arrows; nitrification, black arrows; anaerobic ammonium oxidation, gray arrows; denitrification/intra-aerobic methane oxidation, violet arrows.....	2
Figure 1.2. (a) Homodimeric structure of <i>S. oneidensis</i> ccNiR (UniprotKB Q8EAC7). ³² each protomer contains five heme centers (hemes 1–5). (b) Heme arrangement within one of the ccNiR protomers. Electrons are believed to enter the protein via heme 2 (green). The four bis-His- ligated hemes conduct electrons to the heme 1 active site that has the unusual lysine ligated to it (light green).....	6
Figure 1.3. <i>S. oneidensis</i> ccNiR active site showing heme 1 (blue), the three conserved amino acid residues, Arg103, Tyr206, and His257, that are known to be important for catalytic activity (red sticks), and the unusual proximal axial ligand, Lys123 (green sticks).....	8
Figure 1.4. Working hypothesis, in schematic form, of the pathway by which nitrite reduction to ammonia is catalyzed by ccNiR (adapted from Ref. ⁴³). The overall rate limiting step in the process is shown to be the final 2-electron reduction, based on the studies of Bykov and Neese, ² and on the fact that ammonia is not produced at applied potentials above $\sim -0.1V$, even when its formation should be thermodynamically favored.....	18
Figure 2.1. Large scale (45 L) <i>S. oneidensis</i> culture for large scale purification of R103Q ccNiR. A carboy used for this culture was immersed in a water bath. A thermostat maintained the constant optimum temperature (30 °C). To keep the culture aerated and to avoid cell settling, two fritted sparging tubes inside of the carboy provided compressed air circulation that continuously agitated the culture (Figure reproduced from ref. 1 with permission).....	29
Figure 2.2. Outline of the pyridine hemochrome assay procedure. The bis-pyridine ligated heme obtained in the alkaline pyridine solution is called the “pyridine hemochrome”. ¹⁰	35
Figure 2.3. Extinction coefficient spectra of oxidized and reduced <i>c</i> -heme pyridine hemochrome, along with the reduced – oxidized extinction coefficient difference spectrum. Generated from the data tables provided in ref. 10.....	36
Figure 2.4. Reduced – oxidized difference spectrum of pyridine hemochrome derived from ccNiR, fit with the known extinction coefficient difference spectrum of <i>c</i> -heme pyridine hemochrome. ¹⁰ The pyridine hemochrome concentration was obtained from the fit.....	36
Figure 2.5. (a) Comparison between the R103QccNiR extinction coefficient spectrum (blue line) and that of wtccNiR (red line). (b) $\epsilon(R103QccNiR) - \epsilon(wtccNiR)$ difference spectrum.....	39

Figure: 2.6. WtccNiR-catalyzed reduction of nitrite by MV_{red} at varying MV_{red} concentrations ($k_{app} \equiv V_0/[ccNiR]$). Blue circles are the experimentally obtained values at each MV_{red} concentration. This set of experiments was performed at pH 7.0 in the presence of 70 pM - 100 pM wtccNiR and 0-100 μ M MV_{red}. The solid red line was obtained by averaging the k_{app} values, while the dashed lines represent the standard deviation from the average ($k_{app} = 3600 \pm 850 \text{ s}^{-1}$).....41

Figure: 2.7. R103QccNiR-catalyzed reduction of nitrite by MV_{red} at varying MV_{red} concentrations. Red circles are the experimentally obtained values at each MV_{red} concentration. This set of experiments was performed at pH 7.0 in the presence of 10-200 nM R103QccNiR, 0-100 μ M MV_{red}, and 1mM nitrite. The solid red line was obtained by averaging the k_{app} values, while the dashed lines represent the standard deviation from the average41

Figure 2.8. WtccNiR-catalyzed reduction of nitrite by MV_{red} at varying nitrite concentrations. Blue circles are the experimentally obtained values at each nitrite concentration, while the red curve is the least-squares fit of the data to the rectangular hyperbola Eq 2.2. This set of experiments was performed at pH 7.0 in the presence of 54 pM wtccNiR and 100 μ M MV_{red}. The least-squares fit yielded the parameter values $K_{m2} = (2.4 \pm 0.6) \times 10^{-5} \text{ M}$, $k_{cat2} = 4510 \pm 90 \text{ s}^{-1}$ ($k_{app} \equiv V_0/[ccNiR]$; Section 2.3.2).....43

Figure 2.9. R103QccNiR-catalyzed reduction of nitrite by MV_{red} at varying nitrite concentrations. Blue circles are the experimentally obtained values at each nitrite concentration, while the red curve is the least-squares fit of the data to the rectangular hyperbola Eq 2.2. This set of experiments was performed at pH 7.0 in the presence of 10-110 nM R103QccNiR and 100 μ M MV_{red}. The least-squares fit yielded the parameter values $K_{m2} = (4.7 \pm 0.9) \times 10^{-4} \text{ M}$ and $k_{cat2} = 780 \pm 50 \text{ s}^{-1}$ ($k_{app} \equiv V_0/[ccNiR]$; Section 2.3.2).....43

Figure 2.10. WtccNiR-catalyzed reduction of hydroxylamine by MV_{red} at varying hydroxylamine concentrations. Blue circles are the experimentally obtained values at each hydroxylamine concentration, while the red curve is the least-squares fit of the data to the rectangular hyperbola Eq 2.3. This set of experiments was performed at pH 7.0 in the presence of 54 pM wtccNiR and 100 μ M MV_{red}. The least-squares fit yielded the parameter values $K_{m3} = (2.1 \pm 0.7) \times 10^{-2} \text{ M}$ and $k_{cat3} = 3100 \pm 300 \text{ s}^{-1}$; ($k_{app} \equiv V_0/[ccNiR]$; Section 2.3.2).....44

Figure 2.11. R103QccNiR-catalyzed reduction of hydroxylamine by MV_{red} at varying hydroxylamine concentrations. Blue circles are the experimentally obtained values at each hydroxylamine concentration, while the red curve is the least-squares fit of the data to the rectangular hyperbola Eq 2.3. This set of experiments was performed at pH 7.0 in the presence of 10-110 nM R103QccNiR and 100 μ M MV_{red}. The least-squares fit yielded the parameter values $K_{m3} = (2.7 \pm 0.5) \times 10^{-2} \text{ M}$ and $k_{cat3} = 600 \pm 30 \text{ s}^{-1}$; ($k_{app} \equiv V_0/[ccNiR]$; Section 2.3.2).....45

Figure 3.1. The Apparatus used for the Spectro-potentiometric titrations of wild type and R103QccNiR experiments (reproduced with permission from ref. ⁵). The ash-colored bar is the auxiliary electrode, the white one is the Ag/AgCl reference electrode, and the black bar is the

working electrode. The cuvette was filled from the bottom using a syringe, until the upper reservoir contained enough solution for the electrodes to sit in. The transparent gold mesh is sandwiched between the two plates of the demountable cuvette.....52

Figure 3.2. (a) UV/Vis spectral changes observed upon exposing a solution containing nitrite and the mediators from Table 3.1, but no enzyme, to progressively lower applied potentials. The blue lines are the experimentally obtained spectra, the red ones were calculated using the equations of Scheme 3.1. For clarity, only select spectra are shown. (b) Blue circles: an absorbance difference vs. applied potential slice taken at 600 nm from the spectra in (a); solid red line: least-squares best fit obtained by fitting the data to the Scheme 3.1 equations.....54

Figure 3.3. Spectral components S obtained from fitting the Figure 3.2a data with the Scheme 3.1 equations, along with the midpoint potentials at which each component appeared. The arrows point to distinctive difference maxima that, together with the associated midpoint potentials, could be used to assign each spectral component to a specific mediator or set of mediators (see main text for details).....56

Figure 3.4. (a) UV/Vis spectral changes (with mediator contributions subtracted) observed upon exposing a solution initially containing 79 μM R103QccNiR, 5 mM nitrite, and the mediators listed in Table 3.1, to progressively lower applied potentials. The blue lines are the experimentally obtained spectra, the red ones were calculated using the equations of Scheme 3.2. For clarity, only select spectra are shown. (b) Blue circles: an absorbance difference vs. applied potential slice taken at 409 nm from the spectra in (a); solid red line: least-squares best fit obtained by fitting the data to the Scheme 3.2 equations.....58

Figure 3.5. Spectral components $\Delta\epsilon$, obtained from fitting the Figure 3.4a data with the Scheme 3.2 equations. $\Delta\epsilon_1$ appeared in a step governed by a midpoint potential $\epsilon_1 = 0.174$ V, and $\Delta\epsilon_2$ appeared in a step governed by a midpoint potential $\epsilon_2 = -0.010$ V.....61

Figure 3.6. (a) UV/Vis spectral changes obtained upon exposing a solution initially containing 76 μM of fully oxidized wild type ccNiR, 100 μM 1, 2-naphthoquinone-4-sulfonic acid and 5 mM nitrite to progressively lower potentials.¹ Solid blue lines show the experimentally obtained data, whereas the dashed red lines were calculated from least-squares fitting with a Nernstian 2-electron reduction and one spectral component. The fit yielded a midpoint potential of $\epsilon_m = 0.246$ V. (b) Blue circles: an absorbance difference vs. applied potential slice taken at 424 nm from the spectra of part (a); solid red line: least-squares best fit obtained from global analysis of the data with n fixed at 2 electrons transferred in the Nernstian equation; dotted green line: same as the red line, but with n fixed at 1 electron transferred in the Nernstian equation.....62

Figure 4.1. (a) Blue traces: UV/Vis spectral changes observed after mixing 8 mM Nitrite, 1.2 mM TMPD, and 1.03 μM R103QccNiR in a pH 7 HEPES buffer. Red traces: least-squares best fit with Eq. 4.1. The reaction mixture was monitored at 15s intervals, but for clarity, the selected traces are at 600 s intervals. (b) Blue trace: absorbance vs. time slice taken at the 611 nm maximum of the data set above. Red trace: least-squares best fit with Eq. 4.1.....72

Figure 4.2. Spectral components (a) Λ_0 and (b) Λ_1 generated by fitting the SVD-processed Fig. 4.1 data with Eq. 4.1. The overlaid dashed red traces are the least-squares best fits obtained using known extinction coefficient spectra, as described in the main text.....74

Figure 4.3. Blue circles: dependence of the initial TMPD oxidation rate (V_0 , nM/s) on total R103QccNiR concentration, with $[\text{NO}_2^-]_0$ and $[\text{TMPD}]_0$ held constant at 8 mM and 1.2 mM, respectively. All experiments were performed in 50 mM HEPES buffer (pH 7.0). Red line: least-squares fit of the data; slope = $(7 \pm 2) \times 10^{-3} \text{ s}^{-1}$, intercept = $2 \pm 2 \text{ nMs}^{-1}$ 76

Figure 4.4. Blue circles: dependence of k_{app} ($V_0/[\text{R103QccNiR}]$, s^{-1}) on total TMPD concentration, with $[\text{NO}_2^-]_0$ held constant at 8 mM. All experiments were performed in 50 mM HEPES buffer (pH 7.0). Solid red line: average k_{app} value; dashed lines: standard deviation.....77

Figure 4.5. Blue circles: dependence of k_{app} ($V_0/[\text{R103QccNiR}]$, s^{-1}) on total nitrite concentration, with $[\text{TMPD}]_0$ held constant at 1 mM. All experiments were performed in 50 mM HEPES buffer (pH 7.0). Solid red line: least-squares fit to a rectangular hyperbola in which a K_m value was fixed at an arbitrary value below 100 mM (this was used for illustrative purposes only, as any hyperbolic behavior is completely masked by the data scatter at low nitrite concentrations). The data stayed roughly constant at $0.011 \pm 0.006 \text{ s}^{-1}$ down to about 200 mM $[\text{NO}_2^-]_0$77

Figure 4.6. Blue circles: initial rate of CatNO formation vs R103QccNiR concentration; red squares: initial rate of TMPD_{ox} formation vs R103QccNiR concentration. The blue and red lines are the linear least-squares best fits to each data set. The data sets were collected at pH 7.0, with a nitrite concentration of 2 mM, a TMPD concentration of 1 mM and a catalase concentration 4 μM . Blue line: slope = $(2.54 \pm 0.07) \times 10^{-3} \text{ s}^{-1}$, intercept = $(1.2 \pm 0.4) \times 10^{-10} \text{ M/s}$; red line: $(2.6 \pm 0.1) \times 10^{-3} \text{ s}^{-1}$, intercept = $(9 \pm 7) \times 10^{-11} \text{ M/s}$79

Figure 5.1. (a) Blue traces: UV/Vis spectral changes observed after mixing 1.15 μM R103QccNiR with 4.7 mM nitrite and 1.0 mM pure Ru^{II} , in a pH 7 HEPES buffer. Dashed red traces: least-squares best fit with Eq. 5.1. The reaction mixture was monitored at 15s intervals, but for clarity, the selected traces are at 600 s intervals. (b) Blue trace: absorbance vs. time slice taken at the 409 nm maximum of the data set above. Red trace: least-squares best fit with Eq. 5.1.....89

Figure 5.2. (a) Blue trace: spectral component Λ_0 generated by fitting the SVD-processed Fig. 5.1 data with Eq. 5.1. Red trace: least-squares best fit obtained using known extinction coefficient spectra of R103Q $_{ox}$ and nitrite. (b) Difference spectrum obtained by subtracting the red spectrum in Fig. 5.2a from the blue one.....91

Figure 5.3. Spectral components (a) Λ_1 and (b) Λ_2 that were obtained by fitting the Fig. 5.1a data to Eq. 5.1.....93

Figure 5.4. Dependence on $[\text{Ru}^{II}]$ of the k_{1app} and k_{2app} values obtained from fitting data like those of Fig. 5.1a to Eq. 5.1. In all cases, $[\text{NO}_2^-] = 2 \text{ mM}$ and $[\text{R103QccNiR}] \sim 1.2 \mu\text{M}$94

Figure 5.5. Blue circles: initial rate of CatNO formation vs R103QccNiR concentration; The red line is the linear least-squares best fit to the first four points of the data set (slope = $(7.6 \pm 0.1) \times 10^{-3}$

s^{-1}). The data set was collected at pH 7.0, with a nitrite concentration of 2 mM, a Ru^{II} concentration of 400 μM and a catalase concentration 4 μM94

Figure 5.6. Spectral changes seen at 403 nm (blue trace) and 422 nm green trace upon mixing $\sim 1 \mu M$ R103Q ccNiR, 2 mM nitrite, and 400 μM Ru^{II} . Red traces: least-squares fit of the data to Eq. 5.2.....97

Figure 5.7. Spectral component Λ_3 generated by fitting the SVD-processed stopped-flow data with Eq. 5.2. According to the Eq. 5.2 model, this component represents the spectrum present at $t = 0$97

Figure 5.8. Spectral components (a) Λ_4 and (b) Λ_5 that were obtained by fitting the stopped-flow data to Eq. 5.2. The component Λ_4 grew in with a half-life of about 20 ms, while Λ_5 grew in with a half-life of about 1s.....98

Figure 5.9. (a) Blue traces: UV/Vis spectral changes observed after mixing 1.6 μM R103QccNiR with 2 mM nitrite and a 1:1 mixture of Ru^{II} : Ru^{III} (600 μM total ruthenium) in a pH 7 HEPES buffer. Dashed red traces: least-squares best fit with Eq. 5.3. The reaction mixture was monitored at 15s intervals, but for clarity, the selected traces are at 600 s intervals. (b) Blue trace: absorbance vs. time slice taken at the 409 nm maximum of the data set above. Red trace: least-squares best fit with Eq. 5.3.....101

Figure 5.10. Blue trace: spectral component Λ_6 generated by fitting the SVD-processed Fig. 5.9 data with Eq. 5.3. Dashed red trace: least-squares best fit obtained using known extinction coefficient spectra of R103Q_{ox} and nitrite.....101

Figure 5.11. Spectral component Λ_7 generated by fitting the SVD-processed Fig. 5.9 data with Eq. 5.3. Note the similarity to Λ_2 in Fig. 5.3, the spectrum obtained at infinite time when nitrite-loaded R103Q ccNiR was reduced with pure Ru^{II}101

LIST OF TABLES

Table 2.1. Summary of buffers that were used for column chromatography, dialysis, and storage in R103Q purification storage for R103Q purification.....	30
Table 2.2. Parameters k_{cat2} and K_{m2} (Eq. 2.2) obtained for nitrite reduction by MV_{red} catalyzed by wtccNiR and two variants.....	47
Table 2.3. Parameters k_{cat3} and K_{m3} (Eq. 2.3) obtained for hydroxylamine reduction by MV_{red} catalyzed by wtccNiR and two variants.....	47
Table 3.1. List of mediators used for the spectropotentiometric titrations of R103Qccnir.....	53

LIST OF SCHEMES

Scheme 1.1. Reactions catalyzed by ccNiR under standard assay conditions. The strong reductant methyl viologen.....	9
Scheme 1.2. Enemark-Feltham notation used to represent iron nitrosyl species for which the electron distribution is uncertain.....	15
Scheme 1.3. Some of the catalytic steps proposed for reduction of nitrite to ammonia at the ccNiR active site, based on computational analysis. ¹⁻³ The heme-bound nitrosyl species are represented by their Enemark-Feltham notations (Scheme 1.2). When present in protonated form, the catalytically important conserved active site amino acids are labeled as follows (using <i>S. oneidensis</i> numbering): H _V , Tyr206; H _R , Arg 103; H _H , His257. ⁵ This shorthand is adapted from that used by Bykov and Neese ² , but with some modifications. PCET: <u>P</u> roton <u>C</u> oupled <u>E</u> lectron <u>T</u> ransfer.....	15
Scheme 1.4. Energetics of Fe _{H1} ^{II} (NO ₂ ⁻) disproportionation; DG ⁰ = -23 kJ/mol.....	19
Scheme 2.1. Flow chart that outlines the procedure for calculating the ccNiR extinction coefficient spectrum.....	37
Scheme 3.1. Model used to fit the Fig 3.2 data.....	55
Scheme 3.2. Model used to fit the Fig 3.4 data	59
Scheme 3.3. Possible reduced species that might be generated when the ccNiR active site is exposed to reducing potentials in the presence of nitrite. The evidence presented herein shows that reduction of R103QccNiR generates different species than reduction of wtccNiR. Steps that release free NO are included in the scheme because previous studies in our group showed that wtccNiR catalyzes NO formation under weakly reducing conditions. ¹¹ As will be seen in Chapter 4, R103QccNiR also does this.....	63
Scheme 4.1. <i>N,N,N',N'</i> -tetramethyl- <i>p</i> -phenylenediamine (TMPD) and its 1-electron oxidized radical TMPD _{ox} . The reaction below the structures shows the stoichiometry of nitrite reduction to NO· by TMPD.....	69
Scheme 4.2. Trapping of NO· by catalase. Catalase (Cat) and the nitrosylated product (CatNO) have very different colors.....	78
Scheme 4.3. Minimal scheme that outlines the possible intermediate species that could be generated when the ccNiR active site is exposed to weakly reducing conditions in the presence of nitrite (same as Scheme 3.3)	80
Scheme 5.1. Minimal mechanism proposed to explain the reactivity of nitrite-loaded R103Q ccNiR with Ru ^{II} . Fe _{H1} refers to active site heme 1 and Fe _{H4} to heme 4 (Fig. 1.2b)	103

ACKNOWLEDGMENTS

At first, I would like to acknowledge and express my utmost gratitude to my supervisor Professor A. Andrew Pacheco, for supporting me in my dream and for his supervision to prepare me in my career path. I got the best support and guidance in my research, motivation, comfort during my very difficult time in graduate school. I will never forget the challenging time when his motivation and valuable suggestion and endless support gave me the strength to go further down that road than I ever thought possible. I met a very few persons in my whole lifetime like Professor Pacheco who is not only a caring supervisor but also one of the best human beings. I always pray for him from the core of my heart. I am always very grateful to my supervisor for his active presence in the lab that motivated me to work hard and valuable time he gave us to discuss project, data analysis, professional development and endless mental support that motivated me to focus on my work. As a Graduate student and working mother, when I faced difficulties I got the best advice from him. Thanks to his encouragement and help that shaped me to fit in the graduate school program and for my future career as a scientist.

I would also like to extend my gratitude to Dr. Wilcoxon who actively helped me in EPR analysis and stopped flow experiments. I am also grateful to Dr. Silvaggi for giving ideas about enzyme kinetics and structural biology, Dr. Peng for her valuable suggestions and Dr. Deitz for his valuable suggestions in analytical chemistry and data analysis in my research.

I would like to show my humble thanks to my lab members Steven Reinhardt, Alex Drena, Victoria Mandella, David Kolterman and Brad Dimock for supporting me all the way in the lab. They are really wonderful colleagues, very supportive and welcoming that made my life easier, also thanks to Jonathon Mielke from Dr. Wilcoxon's lab for helping me. I am very lucky to be able

to work alongside such amazing group members. I also want to thank Dr. Ali and Dr. Shahid for their support at the very beginning of my time in Dr. Pacheco's lab.

I would like to show my love and respect to my parents who provided me the best support and unconditional love to fulfil my dream as a scientist. Their prayers and trust helped me to overcome all the barriers in my life and carrier path. I would like to show my love to my husband Dr. Shahnawaz Ali and my ten-year-old son Faieque Nawaz for their unconditional love and support to follow my dreams; without their love, it was been impossible to continue such a stressful journey. Their patience and mental support motivated me to work harder and focus on research.

I acknowledge the support I got from the National Science Foundation (NSF grants MCB-1330809 and MCB-1616824) throughout my research time as a graduate student. Finally, I am always grateful to Almighty Allah who gave me the strength.

Chapter 1

Introduction

1.1. The nitrogen cycle in respiration and environmental processes

Prokaryotic respiratory processes play a critical role in shaping the chemical environment of the biosphere, affecting everything from the levels of greenhouse gases and composition of soils to the speciation of toxic metals such as arsenic and mercury.^{6, 7} The multi-electron redox reactions that drive respiration are catalyzed by highly efficient protein assemblies. This thesis studies cytochrome *c* nitrite reductase (ccNiR) from *Shewanella oneidensis*, one in a class of particularly complex prokaryotic multi-heme respiratory enzymes involved in the nitrogen cycle.

The nitrogen cycle (Fig. 1.1) maintains the environmental nitrogen balance which is very important for living organisms such as plants and animals, as nitrogen is used by all organisms for the biosynthesis of amino acids, nucleosides, and other fundamental compounds.^{8, 9} In addition, some organisms also use nitrogen compounds as substrates for energy transduction, either as electron donors (ammonium) or as electron acceptors (nitrate, nitrite, nitric oxide, nitrous oxide).^{8, 10-13} Nitrogen is the most abundant element in the earth's atmosphere (79%), but it is present there as dinitrogen (N₂) which cannot be absorbed by plants and animals until it is converted to ammonium in the process known as "nitrogen fixation" (yellow arrow, Fig. 1.1). Historically, most nitrogen fixation has been accomplished by certain bacteria and blue-

Animals then ingest these algae and plants, converting them into their own body compounds. The remains of all living things—and their waste products—are ultimately decomposed to ammonium by microorganisms. Under anaerobic conditions, foul-smelling putrefactive intermediates may be temporarily generated, but these are ultimately converted to ammonium.¹⁷

The major reservoirs of inorganic nitrogen are ammonium and nitrate, which are interconverted by plants and bacteria in three processes. Nitrifying bacteria use ammonium as an electron source in aerobic respiration that ultimately results in nitrate formation (black arrows, Fig. 1.1). Most commonly, nitrification involves ammonia oxidizing bacteria that oxidize ammonia to nitrite and distinct nitrite oxidizing bacteria that oxidize nitrite to nitrate. However, very recently, complete ammonia oxidizers that oxidize ammonia all the way to nitrate have also been described.^{18, 19} In contrast to nitrifying bacteria, nitrate- and nitrite-ammonifying bacteria use nitrate and nitrite as electron acceptors in anaerobic respiration, in a process known as “dissimilatory nitrate reduction to ammonium (DNRA, green arrows in Fig. 1.1).¹³ The nitrate and nitrite reduction steps are linked at the cellular level in some organisms, while in other cases the steps are shared between organisms in a community. Finally, plants, fungi and bacteria also convert nitrate and nitrite into ammonium so that it can be assimilated into organic matter (assimilatory ammonification, orange arrows, Fig. 1.1). It should be noted that assimilatory ammonification employs identical chemistry to DNRA, but it is facilitated by evolutionarily unrelated nitrite reductases.¹⁷ Furthermore, the distinction between assimilatory and dissimilatory ammonification is not always clear, and it is likely that bacteria that use nitrite as

an electron acceptor in DNRA also sometimes incorporate the ammonium so formed into organic matter.¹³

In addition to being a source of ammonium, nitrate is also used as an electron acceptor by denitrifying bacteria, which convert it back to dinitrogen, thus completing the cycle (blue arrows, Fig. 1.1). Denitrifying bacteria, are especially active in water-logged anaerobic soils. The action of these bacteria tends to deplete soil nitrates, forming free atmospheric nitrogen. Unlike nitrate reduction to ammonia, which takes place in two steps via nitrite, denitrification takes place in multiple steps that produce nitrite, nitric oxide, and nitrous oxide as discrete byproducts. Heterotrophic microbes that can directly couple reduction of nitrate to nitrite, nitrite to nitric oxide, nitrous oxide, and nitrous oxide to dinitrogen, are known as “classical” or “canonical” denitrifiers. Many organisms, though, carry out only parts of the denitrification process, which can lead to the release of nitrogenous gases such as nitric and nitrous oxides into the environment. This is concerning as nitrous oxide is a potent greenhouse gas and also an ozone depleting one.^{20, 21}

One other process that also empties the reactive nitrogen pool is the process known as “anaerobic ammonium oxidation”, also referred to as “anammox” (gray arrows, Fig. 1.1). In this novel respiratory process, ammonium acts as an electron source and nitrate as an electron acceptor (through a nitric oxide intermediate) to produce hydrazine, which is then oxidized to dinitrogen. Though anammox is a minor process in the nitrogen cycle, it is ecologically beneficial for wastewater treatment as it removes both nitrite and ammonium simultaneously without producing nitrous oxide, and it is being used industrially for sewage treatment.²²⁻²⁵ Anammox is also a major reactive nitrogen removal process in the ocean and in oxygen minimum zones.

This thesis is part of a larger study that aims to understand the reaction mechanism of cytochrome *c* nitrite reductase (ccNiR), which catalyzes the six-electron reduction of nitrite to ammonia as part of the DNRA pathway. The thesis presents an investigation of a *Shewanella oneidensis* ccNiR active-site variant, and draws mechanistic conclusions by comparing the variant's properties with those of the wild type *S. oneidensis* ccNiR and other variants.

1.2. Structural overview of cytochrome *c* nitrite reductase (ccNiR)

Cytochrome *c* nitrite reductase (ccNiR, also called NrfA after the *nrfA* gene that codes for it) is a stable, periplasmic, soluble, multiheme respiratory protein found in a variety of Gram-negative bacteria. The enzyme is a homodimer (Fig. 2.2a), and each protomer has five *c*-type hemes, and a molecular weight that varies from 55 to 70 kDa depending on the bacterial source.²⁶⁻³² Figure 2.2 shows the 1.66 Å structure of the *S. oneidensis* ccNiR homologue (UniprotKB Q8EAC7),³² a variant of which is the main subject of this study. Figure 2.2a shows the homodimer, while Fig. 2.2b shows the arrangement of the five hemes within one of the ccNiR protomers. Four of the hemes (hemes 2–5 in Fig. 2.2b) are low-spin and bis-his ligated, while the active site heme 1 has a high-spin ferric resting state, and, unusually, has a lysine (Lys123 in *S. oneidensis* ccNiR) bound at the proximal site instead of a histidine. The distal site of heme 1 has a loosely bound water that can be displaced by nitrite during catalysis (see below). As with all *c*-type hemes, the ccNiR hemes are covalently bound to the protein

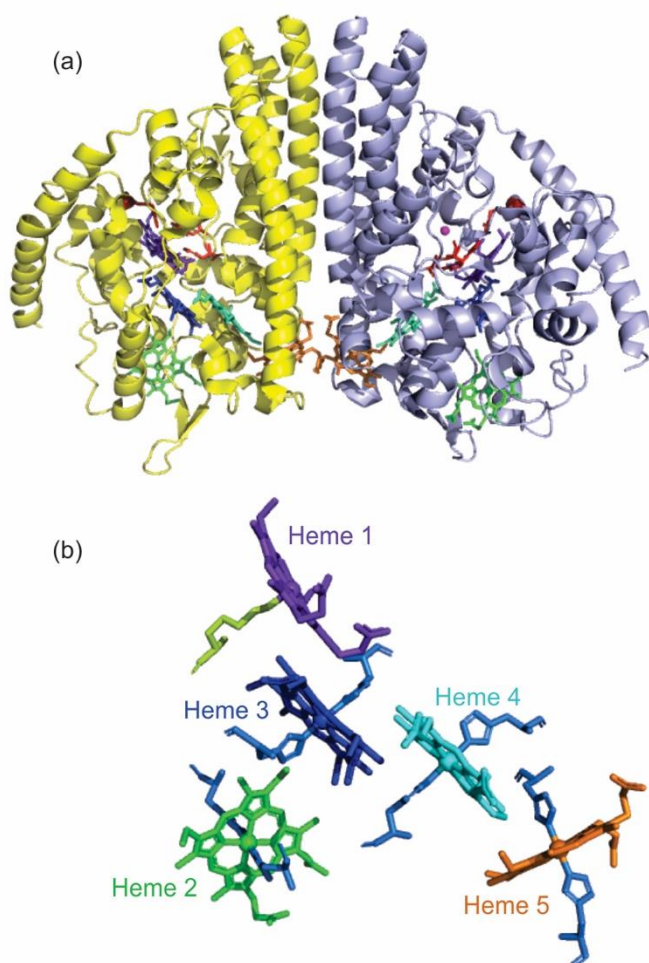


Figure 1.2. (a) Homodimeric structure of *S. oneidensis* ccNiR (UniprotKB Q8EAC7).³² Each protomer contains five heme centers (hemes 1–5). (b) Heme arrangement within one of the ccNiR protomers. Electrons are believed to enter the protein via heme 2 (green). The four bis-His- ligated hemes conduct electrons to the heme 1 active site that has the unusual lysine ligated to it (light green).

backbone through thioether linkages to two cysteines. Hemes 2 – 5 interact with the protein backbone through CXXCH motifs that are characteristic of *c*-hemes;²⁶ however, active site heme 1 interacts via a novel CXXCK sequence, in which K is the lysine axial ligand for the heme.²⁶ The heme arrangement in ccNiR is such that the hemes are closely packed, with iron–iron distances of $<13 \text{ \AA}$, which facilitates rapid inter-heme electron transfer from heme 2, the likely entry point

for electrons, to the heme 1 active site.³⁰ Furthermore, the heme 5 groups from the two protomers are also closely spaced, which may allow inter-protomer electron transfer; thus, electrons entering at heme 2 from one protomer could, in principle, end up at the active site of the other protomer.

All ccNiRs identified to date have three conserved amino acid active site residues that appear to be critical for optimal catalytic activity (Figure 1.3); in *S. oneidensis* ccNiR, these are Arg103, Tyr206, and His257.^{31, 32} In addition, with one exception,³³ a calcium ion (Ca^{2+}) has been found near the active site of all ccNiRs structurally characterized to date, including the *S. oneidensis* enzyme.²⁶⁻³² On the basis of the Ca^{2+} ion's proximity to the active site (~ 11 Å) and other structural clues, it is hypothesized that Ca^{2+} may facilitate proton delivery during catalysis.^{26, 33} The only ccNiR identified to date that does not have a Ca^{2+} ion bound is the homologue from *Geobacter lovleyi*.³³ However, this homologue has a positively charged arginine residue in the spot where Ca^{2+} would usually sit, which appears to perform the same electrostatic function as Ca^{2+} does in other ccNiR homologues.³³

One last feature that is shared by all ccNiR homologues characterized to date is a funnel-like tunnel that leads from the enzyme surface to the active site. This funnel is lined with positively charged amino acid residues and appears to facilitate access to the active site by the negatively charged nitrite substrate.²⁶ The original ccNiR structures also appeared to show a tunnel lined with negatively charged residues leading away from the active site that could be used as an exit path for the ammonium product.²⁶

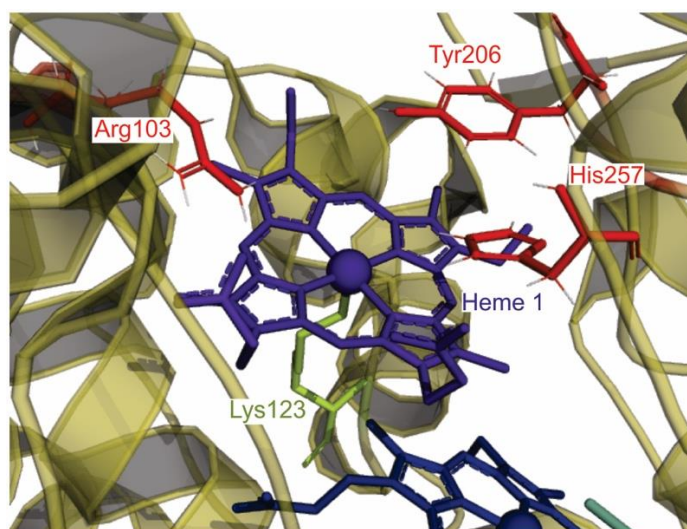


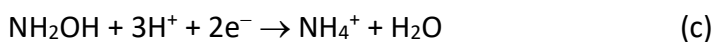
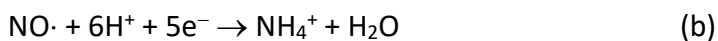
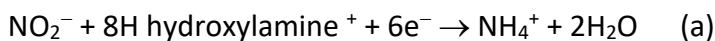
Figure 1.3. *S. oneidensis* ccNiR active site showing heme 1 (blue), the three conserved amino acid residues, Arg103, Tyr206, and His257, that are known to be important for catalytic activity (red sticks), and the unusual proximal axial ligand, Lys123 (green sticks).

1.3. Cytochrome c Nitrite reductase (ccNiR) reaction mechanism

1.3.1. Overview

Scheme 1.1 summarizes the ammonium-generating reactions that are catalyzed by ccNiR *in vitro*.^{26, 28, 29, 34} The obviously physiologically relevant reaction is the 6-electron, 8-proton reduction of nitrite. However, there is substantial evidence that reduction of nitric oxide may also be important to some microorganisms that use the reaction to eliminate this toxic molecule. Nitric oxide can be present as a metabolic byproduct, or in the case of pathogenic bacteria, as a weapon of the host's immune system.³⁵⁻³⁹ In principle, ccNiR could play a role in eliminating hydroxylamine, which is also a toxic byproduct of metabolism. However, as will be shown in

Chapter 2, ccNiR has a very low affinity for hydroxylamine, which makes it unlikely that is a physiological substrate.



Scheme 1.1. Reactions catalyzed by ccNiR under standard assay conditions. The strong reductant methyl viologen monocation radical, MV_{red} , is used as the electron donor.

The standard in vitro assay for ccNiR uses methyl viologen monocation radical (MV_{red} , $E^0 = -0.445\text{ V}$) as the reducing agent for the substrates shown in Scheme 1.1. Ammonium is the only free nitrogenous product in the MV_{red} assay, and no enzyme intermediate has ever been detected with the assay either.^{26, 28, 31, 34, 35} Despite the absence of detectable enzyme intermediates though, the fact that both nitric oxide and hydroxylamine are substrates for ccNiR-catalyzed reduction by MV_{red} suggests that nitrite reduction is likely to proceed via enzyme-bound intermediates that at least formally involve these two species.^{26, 28, 29, 34}.

Several computational studies, together with assessment of the existing ccNiR crystal structures, have provided additional insights regarding the possible ccNiR mechanism, which will be summarized below in Section 1.3.2. Furthermore, work done by the Pacheco group and collaborators during the past eight years has demonstrated that putative catalytic intermediates can be trapped and studied, if ccNiR-catalyzed nitrite reduction proceeds under more weakly reducing conditions than are provided in the MV_{red} assay.^{32, 40-43} The earlier work from our group is summed up in Section 1.3.3. The theoretical and experimental studies reviewed in Sections

1.3.2 and 1.3.3 provided the starting point for the investigations described in this thesis, whose goals are summarized in Section 1.4.

1.3.2. Structural and computational analyses of the ccNiR mechanism

1.3.2.1. Nitrite activation at the ccNiR active site. Resting-state ccNiR has been crystallized with a variety of ligands occupying the active site distal position. For example, the *E. coli* and *S. oneidensis* enzymes have been crystallized with water or hydroxide in the distal position,^{28, 32} while the *W. succinogenes* and *S. deleyianum* structures were obtained with sulfate in this position.²⁶ The *W. succinogenes* structure was also obtained in the presence of the physiological substrate nitrite, and of the putative reaction intermediate, hydroxylamine.³⁴ In a series of computational studies, the Neese group analyzed the ccNiR mechanism, using the experimental structures as benchmarks for calibrating their calculations.^{1-3, 44} These computational studies provided insights that helped guide the work described in this thesis and will now be summarized in detail.

The Neese group first modeled the resting enzyme with water at the distal site. They calculated an iron – oxygen distance of 2.106 Å for water bound to the ferric heme,^{3, 44} which is in good agreement with the experimental structure (2.1 Å).³⁴ The calculations show that water will be weakly bound in both the ferric and ferrous state, with binding energies of –10.8 and –5.6 kcal/mol for the ferrous and ferric complexes, respectively, and that upon reduction, the iron – oxygen bond length should increase from 2.106 Å to 2.134 Å.

The catalytic process starts when the substrate, nitrite, binds to the heme 1 distal site. Nitrite is an ambidentate ligand that can, in principle, bind metals via either a nitrogen (nitro

isomer) or an oxygen (nitrito isomer) donor atom.⁵ Both nitro and nitrito forms are known in heme chemistry. For example, the nitrito isomer was found in horse-heart myoglobin,⁴⁵ and human myoglobin,⁴⁶ in which the proximal site is typically histidine bound. In the case of ccNiR, the 2002 structure of the *W. succinogenes* homologue displayed the nitro isomer.³⁴ The theoretical calculations by Bykov and Neese also predicted that binding via oxygen should be 4 kcal/mol less favorable than binding via nitrogen.⁴⁴ The calculations suggest that the proximal lysine ligand plays a role in stabilizing the nitro form, as do the positively charged amino acid residues that line the active site and interact with the N-bound nitrite's oxygen atoms.^{3, 34, 44} In the *S. oneidensis* homologue the positively charged amino acids that stabilize the nitro form are His257 and Arg103 (Fig. 1.3).^{31, 32}

Density functional (DFT) calculations predict that the Fe-N bond becomes significantly stronger when the nitrite-loaded active site is reduced. This can be attributed to π -backbonding from the more electron-rich ferrous iron into the nitrite π -antibonding orbital.⁵ As a consequence of π -backbonding, the Fe^{II}-N bond length is calculated to be a short 1.877 Å. At the same time, as mentioned earlier, the Fe – O bond distance of active site-bound water lengthens from 2.106 Å to 2.134 Å upon heme reduction, which facilitates replacement of the water by nitrite upon reduction. The driving force for the replacement was calculated to be –39 kcal/mol).³ In addition to shortening the Fe – N bond, π -backbonding also weakens the nitrite N – O bond as it adds electron density to the antibonding orbital. This results in N – O bond elongation, which facilitates the subsequent heterolytic cleavage of one of the N-O bonds.^{3, 34, 44, 47, 48} The active site amino acid residues (R103, Y206, H257 in *S. oneidensis* ccNiR) form an electropositive

environment that fine-tunes the iron-nitrite π -backbond to optimize for subsequent PCET reactions.^{3, 29}

1.3.2.2. The Possible Pathways for the First N–O Bond Cleavage. The theoretical work of the Neese group explored the role of the three conserved active site residues (Arg103, Tyr206, and His257 in *S. oneidensis*) in mediating the first N – O nitrite bond cleavage. At physiological pH, the Arg and Tyr must be protonated since their side chain pK_a values are expected to be around 12.5 and 10.1, respectively, based on the pK_a s of the free amino acids. The pK_a of the His side chain ($pK_a=6.00$ in the free amino acid) is close to the physiological level, which indicates it can be protonated or deprotonated. Bykov and Neese computationally explored two reaction pathways, the first assuming that His was initially protonated, the second that it was deprotonated.^{3, 44}

When His was initially protonated (HisH^+) the theoretical analysis of Bykov and Neese showed that proton transfer from either Arg or HisH^+ gave a stable $\text{Fe}(\text{HONO})$ adduct; however, proton transfer from Arg was highly endergonic ($\Delta G = +17.7$ kcal/mol) while proton transfer from HisH^+ was much more thermodynamically feasible ($\Delta G = +4.9$ kcal/mol). The latter is still endergonic, but this is manageable if the $\text{Fe}(\text{HONO})$ is continually removed by subsequent reactions. The calculations also showed a reasonable activation barrier for proton transfer from HisH^+ to bound nitrite ($\Delta G^\ddagger = +5.5$ kcal/mol).⁴⁴ The crystallographic evidence supports an initial proton transfer from HisH^+ .^{34, 49, 50} According to the crystal structure of nitrite-bound ccNiR, the active site His is very close (2.6 Å) to one of the nitrite oxygen atoms. The active site Arg is close, but not as close, to the second nitrite oxygen (2.8 Å).³⁴ Bykov and Neese calculate an H-bonding distance of 1.56 Å for the nitrite- HisH^+ interaction and 2.67 Å and 2.30 Å for the two Arg

interactions.⁴⁴ Furthermore, an H-bonding interaction is also seen between Arg and O in the hydroxylamine-bound ccNiR crystal structure (3.0 Å), whereas the His – O hydrogen bond is missing in this structure,³⁴ suggesting that the oxygen that interacted with HisH⁺ in the nitrite structure has now been cleaved.

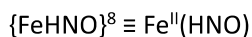
To cleave the first N-O bond completely, two protons need to be transferred to the O leaving group, so Bykov and Neese next computationally explored possible pathways for the second protonation.⁴⁴ The nitrite turnover rate puts an upper limit of about +15.2 kcal/mol on the rate limiting activation barrier,^{51, 52} which limited the possibilities. Bykov and Neese showed that His could be re-protonated if the Fe-bound HONO temporarily rotated towards Tyr at an energy cost of +4.2 kcal/mol. This, together with the +7.9 kcal/mol cost of His reprotonation, provided an activation barrier of +12.1 kcal/mol, in the range of the experimental predictions.^{51, 52} The calculations also showed that subsequent proton transfer from HisH⁺ and hydrolysis of the resulting H₂ONO could proceed with no further activation barrier.

In calculations where the active site His was taken to be deprotonated at the start of the reaction, Bykov and Neese showed that the lowest energy path involved successive protonations of the nitrite oxygen leaving group by the active site Arg, which was reprotonated after each proton transfer step.⁴⁴ In this case, the first activation barrier was 16.7 kcal/mol and the second 17.2 kcal/mol. These activation barriers are higher than those calculated when HisH⁺ is the proton donor, but they are still close to the +15.2 kcal/mol maximum placed on the activation barrier by the experimental turnover rate.^{51, 52} Taken together, the conclusions of Bykov and Neese suggest that while ccNiR may use HisH⁺ as the proton donor at low pH, it should still be

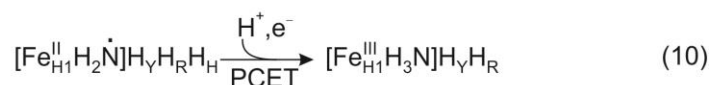
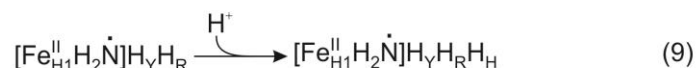
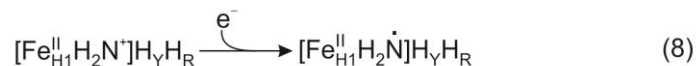
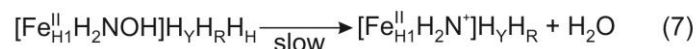
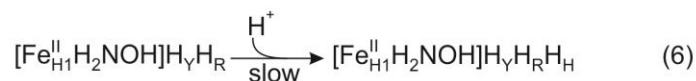
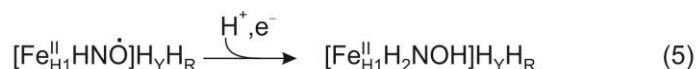
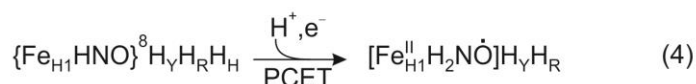
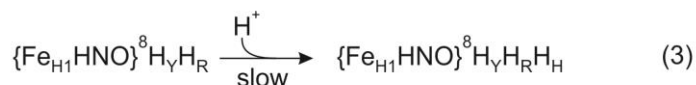
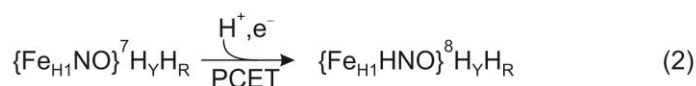
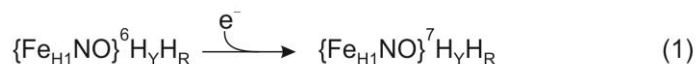
able to catalyze the first N – O nitrite bond cleavage fairly rapidly at high pH by using Arg as an alternate proton source.

1.3.2.3. Heme iron-nitrosyl intermediates and the second N – O bond cleavage. The Neese computational group analyzed the reduction steps that follow cleavage of the first N – O bond in two detailed articles,^{1, 2} and a review.³ The analyses looked at the changes occurring at the heme 1 center, as well as the protonation states of the three conserved active site amino acid residues known to be directly involved in catalysis (see above). This section summarizes the key results of the analyses, using a modified version of the shorthand used by Bykov and Neese in their papers that was developed by Shahid of our laboratory (Scheme 1.3).⁵

Following cleavage of the N – O bond in nitrite bound to ferrous heme, one obtains an iron nitrosyl species referred to as $\{\text{Fe}_{\text{H1}}\text{NO}\}$ ⁶ using the Enemark-Feltham notation (Scheme 1.2).⁴ This species is, in turn, sequentially reduced by two more electrons, to generate iron nitrosyl species referred to as $\{\text{Fe}_{\text{H1}}\text{NO}\}$ ⁷ and $\{\text{Fe}_{\text{H1}}\text{HNO}\}$ ⁸ (Scheme 1.2).⁴ The $\{\text{Fe}_{\text{H1}}\text{NO}\}$ ⁶ reduction to $\{\text{Fe}_{\text{H1}}\text{NO}\}$ ⁷ (Step 1, Scheme 1.3) was predicted to be highly exergonic,¹ a prediction that is consistent with later experimental results in our laboratories (see Section 1.3.3 below). Bykov and Neese analyzed the sequential reductions computationally to assess the roles of the conserved active site amino acids.^{1, 3} In the $\{\text{Fe}_{\text{H1}}\text{NO}\}$ ⁷ state, Arg103 was protonated, but His257 remained unprotonated (steps 1 and 2, Scheme 1.3). The $\{\text{Fe}_{\text{H1}}\text{NO}\}$ ⁷ state was calculated to be a thermodynamic minimum; however, the species could be reduced in a coupled proton electron transfer step to $\{\text{Fe}_{\text{H1}}\text{HNO}\}$ ⁸, in a nearly thermoneutral process with a 6.5 kcal/mol activation barrier (Step 2, Scheme 1.3).¹



Scheme 1.2. Enemark-Feltham notation used to represent iron nitrosyl species for which the electron distribution is uncertain.⁴



Scheme 1.3. Some of the catalytic steps proposed for reduction of nitrite to ammonia at the ccNiR active site, based on computational analysis.¹⁻³ The heme-bound nitrosyl species are represented by their Enemark-Feltham notations (Scheme 1.2). When present in protonated form, the catalytically important conserved active site amino acids are labeled as follows (using *S. oneidensis* numbering): H_Y, Tyr206; H_R, Arg 103; H_H, His257.⁵ This shorthand is adapted from that used by Bykov and Neese,² but with some modifications. PCET: Proton Coupled Electron Transfer.

Reduction of $\{\text{Fe}_{\text{H1}}\text{HNO}\}^8$ is prohibitively endergonic unless it is coupled to proton transfer, and Bykov and Neese's calculations suggest that this first requires a rate limiting protonation of His 257 (+12.9 kcal/mol, Step 3, Scheme 1.3).² There are two energetically plausible products of $\{\text{Fe}_{\text{H1}}\text{HNO}\}^8$ reduction, and Step 4 of Scheme 1.3 shows the one that is most consistent with our experimental results, the ferrous $[\text{Fe}_{\text{H1}}\text{H}_2\text{NO}\cdot]$ (see Section 1.3.3 below). Sequential protonation and reduction of the active site moiety next generates the ferrous hydroxylamine-bound intermediate, $[\text{Fe}_{\text{H1}}\text{H}_2\text{NOH}]$ (Step 5, Scheme 1.3).

The final stage in the catalytic cycle is the reduction of bound hydroxylamine to ammonia, and both the computational studies,² and experimental results from our laboratories (Section 1.3.3 below), suggest that this is an energetically expensive process. The computational studies unambiguously show that the rate limiting step is hydroxylamine dehydration, which requires a prior protonation. The lowest energy pathway requires an initial protonation of His 257 at a cost of 5 kcal/mol (Step 6, Scheme 1.3), followed by proton transfer to the hydroxylamine oxygen and subsequent dehydration (Step 7, Scheme 1.3). This step is highly endergonic (9.0 kcal/mol) and has an activation barrier of 12.2 kcal/mol². Experimental results (Section 1.3.3 below) suggest that this may be the overall rate limiting step in nitrite reduction to ammonia; however, the activation energy is still within the range of the +15.2 kcal/mol barrier predicted from experimental results.^{51, 52,53}

Once hydroxylamine has been dehydrated, the subsequent reactions are all highly exergonic, with steps 8-10 of Scheme 1.3 showing one plausible sequence to heme-bound ammonia. The most important conclusion to come from the computational analysis of the final steps was that the product had ammonia bound to ferric heme. In that case, the rate of

dissociation of the bound ammonia is governed by a switch from a low-spin to high-spin ferric state as the Fe – N bond lengthens; the low spin state energy increases as the bond lengthens, whereas the high-spin state energy decreases. The activation barrier for the dissociation is the point at which the low-spin and high-spin potential energy surfaces cross.²

1.3.3. Detection of catalytic intermediates under weakly reducing conditions

As mentioned earlier, work done by the Pacheco group and collaborators during the past eight years has demonstrated that putative catalytic intermediates can be trapped and studied, if ccNiR-catalyzed nitrite reduction proceeds under more weakly reducing conditions than are provided in the MV_{red} assay.^{32, 40-43} This approach is proving valuable for testing the theoretical predictions made by Bykov and Neese that were summarized in Section 1.3.2.^{1-3, 44} This section will recap the studies that had been published prior to the work described in this thesis, which are summarized schematically in Fig. 1.4.

The first step in nitrite reduction to ammonia is the binding of nitrite to the active site. In Fig. 1.4 this is the step going from Fe_{H1}^{III} to Fe_{H1}^{III}(NO₂⁻). The nitrite binding constant was determined to be $(5.0 \pm 0.1) \times 10^3 \text{ M}^{-1}$ in a titration of the fully oxidized enzyme by nitrite that was monitored by EPR.³² From this, the standard free energy of nitrite binding to the fully oxidized active site was estimated to be about -20 kJ/mol. A UV/Vis spectropotentiometric titration showed that Fe_{H1}^{III}(NO₂⁻) reduced to {Fe_{H1}NO}⁷ in a concerted 2-electron step that has a midpoint potential of 0.246 V vs SHE at pH 7, which corresponds to a standard free energy difference of about -50 kJ/mol vs SHE for reduction of nitrite-loaded heme 1. Though no species are detected between Fe_{H1}^{III}(NO₂⁻) and {Fe_{H1}NO}⁷ under equilibrium conditions, a 1-

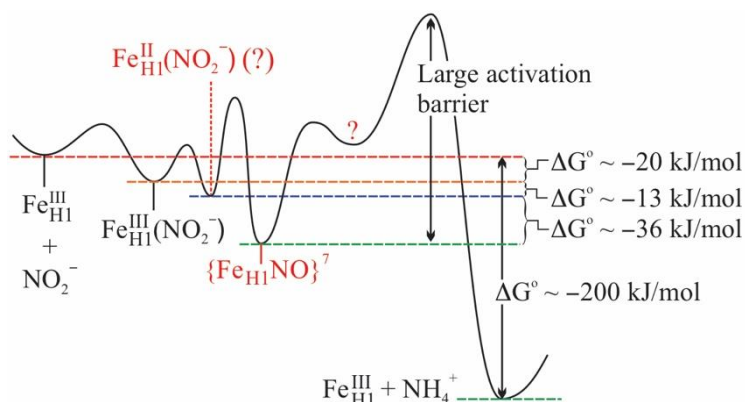
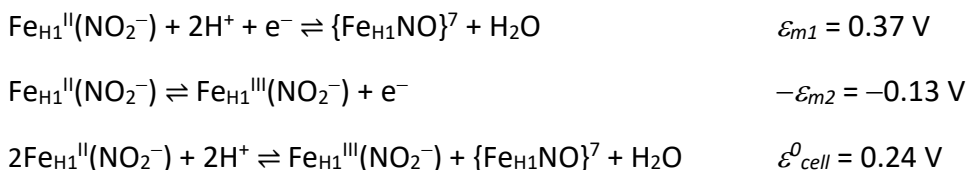


Figure 1.4. Working hypothesis, in schematic form, of the pathway by which nitrite reduction to ammonia is catalyzed by ccNiR (adapted from Ref. 43). The overall rate limiting step in the process is shown to be the final 2-electron reduction, based on the studies of Bykov and Neese,² and on the fact that ammonia is not produced at applied potentials above $\sim -0.1\text{V}$, even when its formation should be thermodynamically favored.⁴³

electron reduced species was transiently observed in UV/Vis stopped-flow studies when wtccNiR was reduced by the weak reductant *N,N,N',N'*-tetramethyl-*p*-phenylenediamine (TMPD).⁴³ The 1-electron reduced species accumulated rapidly (on the ms timescale) in a pseudo-first-order process, and was then further reduced to the $\{\text{Fe}_{\text{H1}}\text{NO}\}^7$ moiety by TMPD in a second pseudo-first-order process. Shahid et al. proposed that the 1-electron reduced intermediate is $\text{Fe}_{\text{H1}}^{\text{II}}(\text{NO}_2^-)$ because the theoretical studies of Bykov and Neese identify the rate limiting step in reduction of $\text{Fe}_{\text{H1}}^{\text{III}}(\text{NO}_2^-)$ to $\{\text{Fe}_{\text{H1}}\text{NO}\}^7$ to be the dehydration of heme-bound nitrite that generates $\{\text{Fe}_{\text{H1}}\text{NO}\}^6$.^{1, 44} By analyzing the dependence of the first reduction's reaction rate on TMPD concentration, Shahid et al. estimated the midpoint potential for $\text{Fe}_{\text{H1}}^{\text{III}}(\text{NO}_2^-)$ reduction to $\text{Fe}_{\text{H1}}^{\text{II}}(\text{NO}_2^-)$ to be 0.13V vs SHE, and that for reduction of $\text{Fe}_{\text{H1}}^{\text{II}}(\text{NO}_2^-)$ to $\{\text{Fe}_{\text{H1}}\text{NO}\}^7$ to be 0.37V vs SHE.⁴³ The fact that the second midpoint potential is so much higher than the first explains why $\text{Fe}_{\text{H1}}^{\text{II}}(\text{NO}_2^-)$ doesn't accumulate under equilibrium conditions, as this species is unstable with respect to disproportionation to $\text{Fe}_{\text{H1}}^{\text{III}}(\text{NO}_2^-)$ and $\{\text{Fe}_{\text{H1}}\text{NO}\}^7$ (Scheme 1.4); in other words, as

$\text{Fe}_{\text{H1}}^{\text{II}}(\text{NO}_2^-)$ accumulates, it reacts with itself to form $\text{Fe}_{\text{H1}}^{\text{III}}(\text{NO}_2^-)$ and $\{\text{Fe}_{\text{H1}}\text{NO}\}^7$, in a process that has a favorable driving force of -23 kJ/mol . (Scheme 1.4).



Scheme 1.4. Energetics of $\text{Fe}_{\text{H1}}^{\text{II}}(\text{NO}_2^-)$ disproportionation; $\Delta G^0 = -23 \text{ kJ/mol}$.

As discussed more fully in refs. 5, 32, 43, $\text{Fe}_{\text{H1}}^{\text{II}}(\text{NO}_2^-)$ and $\{\text{Fe}_{\text{H1}}\text{NO}\}^7$ may not be the only catalytic intermediates that can be trapped by tuning the potential applied to nitrite-loaded ccNiR. Preliminary UV/Vis spectropotentiometric studies⁵⁴ showed that a second intermediate might accumulate at applied potentials between -80 mV vs SHE and the -120 mV vs SHE required for detectable catalytic turnover; this hypothesis is also supported by the results of rapid-mixing experiments with ccNiR and hydroxylamine.⁴⁰ UV/Vis stopped-flow experiments showed that when ccNiR was mixed with large excesses of hydroxylamine ($10 \text{ mM} - 300 \text{ mM}$) the ccNiR was reduced in a triphasic exponential process. A follow-up using the rapid freeze-quench technique showed that a radical species built up within 100 ms of mixing, and then decayed, but not to zero concentration. EPR analysis⁴⁰ suggested that this transient intermediate was most likely the ferrous $[\text{Fe}_{\text{H1}}\text{H}_2\text{NO}\cdot]$ moiety that theoretical studies have proposed as an intermediate in ccNiR-catalyzed nitrite reduction (Step 4 of Scheme 1.3).² Together, the stopped-flow and rapid freeze-quench EPR studies suggested that, within 10 s of mixing ccNiR with hydroxylamine, electrons were transferred from the hydroxylamine to the ccNiR heme pool, generating an equilibrium mixture of partly reduced nitrosylated ccNiR moieties.⁴⁰ These probably include $\{\text{Fe}_{\text{H1}}\text{NO}\}^7$,

together with as-yet uncharacterized species that are collectively depicted by a question mark in Figure 1.4.

1.4. Specific objectives of this thesis

The theoretical and experimental studies on ccNiR that have been completed so far provide an excellent mechanistic scaffold for understanding the ccNiR reaction mechanism (Scheme 1.3 and Fig. 1.4). However, many questions remain regarding important details of the mechanism. This thesis describes a study of the ccNiR variant R103Q. Arg 103 (Fig. 1.3) is one of three strictly conserved active site amino acids, and the goal of the study was to shed light on the catalytic function of this amino acid. Chapter 2 describes the purification and preliminary characterization of R103QccNiR, including its nitrite and hydroxylamine reductase activities in comparison to those of wtccNiR and the H257Q ccNiR variant. Chapter 3 presents a UV/Vis spectropotentiometric titration of R103QccNiR in the presence of nitrite, comparing the variant's electrochemical behavior to that of the wild type enzyme. Chapter 4 explores the reactivity of R103Q ccNiR with the weak reductant *N,N,N',N'*-tetramethyl-*p*-phenylenediamine (TMPD) in the presence of nitrite, with particular attention to R103Q ccNiR's ability to catalyze reduction of nitrite to nitric oxide by TMPD. Chapter 5 similarly explores the reactivity of R103Q ccNiR with hexaammineruthenium(II) in the presence of nitrite. Hexaammineruthenium(II) is a significantly stronger reducing agent than TMPD, but is still weak compared to the methyl viologen monocation radical, MV_{red}. Finally, Chapter 6 summarizes and ties together the results of Chapters 2-5, and then makes suggestions for further study.

1.5. References

1. Bykov, D.; Neese, F., Reductive activation of the heme iron-nitrosyl intermediate in the reaction mechanism of cytochrome c nitrite reductase: a theoretical study. *J. Biol. Inorg. Chem.* **2012**, *17* (5), 741-760.
2. Bykov, D.; Plog, M.; Neese, F., Heme-bound nitroxyl, hydroxylamine, and ammonia ligands as intermediates in the reaction cycle of cytochrome c nitrite reductase: a theoretical study. *J. Biol. Inorg. Chem.* **2014**, *19*, 97-112.
3. Bykov, D.; Neese, F., Six-electron reduction of nitrite to ammonia by cytochrome c nitrite reductase: insights from density functional theory studies. *Inorg. Chem.* **2015**, *54*, 9303-9316.
4. Enemark, J. H.; Feltham, R. D., Principles of Structure, Bonding and Reactivity for Metal Nitrosyl Complexes. *Coord. Chem. Rev.* **1974**, *13*, 339-406.
5. Shahid, S. A mechanistic investigation of cytochrome c nitrite reductase catalyzed reduction of nitrite to ammonia: the search for catalytic intermediates. University of Wisconsin-Milwaukee, Milwaukee, WI, 2020.
6. Ehrlich, H. L., *Geomicrobiology*. 4th ed.; Marcel Dekker, Inc: New York, NY, 2002.
7. Fenchel, T.; King, G. M.; Blackburn, T. H., *Bacterial Biogeochemistry*. 2nd ed.; Academic Press: London, 1998.
8. Canfield, D. E.; Glazer, A. N.; Falkowski, P. G., The Evolution and Future of Earth's Nitrogen Cycle. *Science* **2010**, *330*, 192-196.
9. Bernhard, A. E., The nitrogen cycle: processes, players, and the human impact. *Nat. Educ. Knowl.* **2010**, *2*, 12.
10. Raymond, J.; Siefert, J. L.; Staples, C. R.; Blankenship, R. E., The natural history of nitrogen fixation. *Mol. Biol. Evol.* **2004**, *21*, 541-554.
11. Da Silva, J. F.; Williams, R. J. P., *The biological chemistry of the elements: the inorganic chemistry of life*. Oxford University Press: 2001.
12. Bothe, H.; Ferguson, S. J.; Newton, W. E., *Biology of the nitrogen cycle*. Elsevier: Amsterdam, 2007.
13. Moreno-Vivian, C.; Ferguson, S. J., Definition and distinction between assimilatory, dissimilatory, and respiratory pathways *Mol. Microbiol.* **1998**, *29*, 661-669.
14. Fritz, G.; Einsle, O.; Rudolf, M.; Schiffer, A.; Kroneck, P. M. H., Key bacterial multi-centered metal enzymes involved in nitrate and sulfate respiration. *J. Mol. Microbiol. Biotechnol.* **2005**, *10*, 223-233.
15. Galloway, J. N.; Leach, A. M.; Bleeker, A.; Erismann, J. W., A chronology of human understanding of the nitrogen cycle. *Phil. Trans. R. Soc. B.* **2013**, *368*, 20130120.
16. Lehnert, N.; Coruzzi, G.; Hegg, E.; Seefeldt, L.; Stein, L. Feeding the world in the 21st century: grand challenges in the nitrogen cycle.
17. Maia, L. B.; Moura, J. G., How biology handles nitrite. *Chem. Rev.* **2014**, *114*, 5273-5357.
18. Daims, H.; Lebedeva, E. V.; Pjevac, P.; Herbold, C.; Albertsen, M.; Jehmlich, N.; Palatinszky, M.; Vierheilig, J.; Kirkegaard, R. H.; von Bergen, M.; Rattei, T.; Bendinger, B.; Nielsen, P. H.; Wagner, M., Complete nitrification by *Nitrospira* bacteria. *Nature* **2015**, *528*, 504-509.

19. van Kessel, M. A. H. J.; Speth, D. R.; Albertsen, M.; Nielsen, P. H.; Op den Camp, H. J. M.; Kartal, B.; Jetten, M. S. M.; Lucker, S., Complete nitrification by a single microorganism. *Nature* **2015**, *528*, 555-559.
20. Ravishankara, A. R.; Daniel, J. S.; Portmann, R. W., Nitrous oxide (N₂O): the dominant ozone-depleting substance emitted in the 21st century. *Science* **2009**, *326*, 123-125.
21. Wuebbles, D. J., Nitrous oxide: no laughing matter. *Science* **2009**, *326*, 56-57.
22. Kartal, B.; Maalcke, W. J.; de Almeida, N. M.; Cirpus, I.; Gloerich, J.; Geerts, W.; Op den Camp, H. J. M.; Harangi, H. R.; Janssen-Megens, E. M.; Francoijs, K.-J.; Stunnenberg, H. G.; Keltjens, J. T.; Jetten, M. S. M.; Strous, M., Molecular mechanisms of anaerobic ammonium oxidation. *Nature* **2011**, *479*, 127-130.
23. Kartal, B.; de Almeida, N. M.; Maalcke, W. J.; Op den Camp, H. J. M.; Jetten, M. S. M.; Keltjens, J. T., How to make a living from anaerobic ammonium oxidation. *FEMS Microbiol. Rev.* **2013**, *37*, 428-461.
24. Maalcke, W. J.; Dietle, A.; Marritt, S. J.; Butt, J. N.; Jetten, M. S. M.; Keltjens, J. T.; Barends, T. R. M.; Kartal, B., Structural basis of biological NO generation by octaheme oxidoreductases. *J. Biol. Chem.* **2014**, *289*, 1228-1242.
25. Dietle, A.; Ferousi, C.; Maalcke, W. J.; Menzel, A.; de Vries, S.; Keltjens, J. T.; Jetten, M. S. M.; Kartal, B.; Barends, T. R. M., The inner workings of the hydrazine synthase multiprotein complex. *Nature* **2015**, *527*, 394-397.
26. Einsle, O.; Messerschmidt, A.; Stach, P.; Bourenkov, G. P.; Bartunik, H. D.; Huber, R.; Kroneck, P. M. H., Structure of cytochrome c nitrite reductase. *Nature* **1999**, *400* (6743), 476-480.
27. Einsle, O.; Stach, P.; Messerschmidt, A.; Simon, J.; Kroger, A.; Huber, R.; Kroneck, P. M. H., Cytochrome c nitrite reductase from *Wolinella succinogenes* - Structure at 1.6 angstrom resolution, inhibitor binding, and heme-packing motifs. *J. Biol. Chem.* **2000**, *275* (50), 39608-39616.
28. Bamford, V. A.; Angove, H. C.; Seward, H. E.; Thomson, A. J.; Cole, J. A.; Butt, J. N.; Hemmings, A. M.; Richardson, D. J., Structure and spectroscopy of the periplasmic cytochrome c nitrite reductase from *Escherichia coli*. *Biochemistry* **2002**, *41* (9), 2921-2931.
29. Cunha, C. A.; Macieira, S.; Dias, J. M.; Almeida, G.; Goncalves, L. L.; Costa, C.; Lampreia, J.; Huber, R.; Moura, J. J. G.; Moura, I.; Romao, M. J., Cytochrome c nitrite reductase from *Desulfovibrio desulfuricans* ATCC 27774 - The relevance of the two calcium sites in the structure of the catalytic subunit (NrfA). *J. Biol. Chem.* **2003**, *278* (19), 17455-17465.
30. Rodrigues, M.; Oliveira, T.; Pereira, I.; Archer, M., X-ray structure of the membrane-bound cytochrome c quinol dehydrogenase NrfH reveals novel haem coordination. *EMBO Journal* **2006**, *25*, 5951-5960.
31. Youngblut, M.; Judd, E. T.; Srajer, V.; Sayyed, B.; Goelzer, T.; Elliott, S. J.; Schmidt, M.; Pacheco, A. A., Laue crystal structure of *Shewanella oneidensis* cytochrome c nitrite reductase from a high-yield expression system. *J. Biol. Inorg. Chem.* **2012**, *17*, 647-662.
32. Ali, M.; Stein, N.; Mao, Y.; Shahid, S.; Schmidt, M.; Bennett, B.; Pacheco, A. A., Trapping of a putative intermediate in the cytochrome c nitrite reductase (ccNiR)-catalyzed reduction of nitrite: implications for the ccNiR reaction mechanism. *J. Am. Chem. Soc.* **2019**, *141*, 13358-13371.
33. Campecino, J.; Lagishetty, S.; Wawrzak, Z.; Alfaro, V. S.; Lehnert, N.; Reguera, G.; Hu, J.; Hegg, E., Cytochrome c nitrite reductase from the bacterium *Geobacter lovleyi* represents a new NrfA subclass. *J. Biol. Chem.* **2020**, *295*, 11455-11465.

34. Einsle, O.; Messerschmidt, A.; Huber, R.; Kroneck, P. M. H.; Neese, F., Mechanism of the six-electron reduction of nitrite to ammonia by cytochrome c nitrite reductase. *J. Am. Chem. Soc.* **2002**, *124* (39), 11737-11745.
35. Poock, S.; Leach, E.; Moir, J.; Cole, J.; Richardson, D., Respiratory Detoxification of Nitric Oxide by the Cytochrome c Nitrite Reductase of *Escherichia coli*. *J. Biol. Chem.* **2002**, *277* (26), 23664-23669.
36. Pittman, M. S.; Elvers, K. T.; Lee, L.; Jones, M. A.; Poole, R. K.; Park, S. F.; Kelly, D. J., Growth of *Campylobacter jejuni* on nitrate and nitrite: electron transport to NapA and NrfA via NrfH and distinct roles for NrfA and the globin Cgb in protection against nitrosative stress. *Mol. Microbiol.* **2007**, *63*, 575-590.
37. Macuch, P. J.; Tanner, A. C., *Campylobacter* species in health, gingivitis, and periodontitis. *J. Dent. Res.* **2000**, *79*, 785-792.
38. Klotz, M. G.; Schmid, M. C.; Strous, M.; op den Camp, H. J. M.; Jetten, M. S. M.; Hooper, A. B., Evolution of an octahaem cytochrome c protein family that is key to aerobic and anaerobic ammonia oxidation by bacteria. *Environ. Microbiol.* **2008**, *10*, 3150-3163.
39. Tikhonova, T.; Tikhonov, A.; Trofimov, A.; Polyakov, K.; Boyko, K.; Cherkashin, E.; Rakitina, T.; Sorokin, D.; Popov, V., Comparative structural and functional analysis of two octaheme nitrite reductases from closely related *Thioalkalovibrio* species. *FEBS J.* **2012**, *279*, 4052-4061.
40. Youngblut, M.; Pauly, D. J.; Stein, N.; Walters, D.; Conrad, J. A.; Moran, G. R.; Bennett, B.; Pacheco, A. A., *Shewanella oneidensis* cytochrome c nitrite reductase (ccNiR) does not disproportionate hydroxylamine to ammonia and nitrite, despite a strongly favorable driving force. *Biochemistry* **2014**, *53*, 2136-2144.
41. Judd, E. T.; Youngblut, M.; Pacheco, A. A.; Elliott, S. J., Direct Electrochemistry of *Shewanella oneidensis* Cytochrome c Nitrite Reductase: Evidence of Interactions across the Dimeric Interface. *Biochemistry* **2012**, *51* (51), 10175-10185.
42. Judd, E. T.; Stein, N.; Pacheco, A. A.; Elliott, S. J., Hydrogen bonding networks tune proton-coupled redox steps during the enzymatic six-electron conversion of nitrite to ammonia. *Biochemistry* **2014**, *53*, 5638-5646.
43. Shahid, S.; Ali, M.; Legaspi-Humiston, D.; Wilcoxon, J.; Pacheco, A. A., A kinetic investigation of the early steps in cytochrome c nitrite reductase (ccNiR)-catalyzed reduction of nitrite. *Biochemistry* **2021**, *60*, 2098-2115.
44. Bykov, D.; Neese, F., Substrate binding and activation in the active site of cytochrome c nitrite reductase: a density functional study. *J. Biol. Inorg. Chem* **2011**, *16*, 417-430.
45. Copeland, D. M.; Soares, A. S.; West, A. H.; Richter-Addo, G. B., Crystal structures of the nitrite and nitric oxide complexes of horse heart myoglobin. *J. Inorg. Biochem.* **2006**, *100*, 1413-1425.
46. Yi, J.; Safo, M. K.; Richter-Addo, G. B., The nitrite anion binds to human hemoglobin via the uncommon O-nitrito mode. *Biochemistry* **2008**, *47* (32), 8247-8249.
47. Nasri, H.; Ellison, M. K.; Shang, M.; Schultz, C. E.; Scheidt, W. R., Variable π -bonding in iron(II) porphyrinates with nitrite, CO, and tert-butyl isocyanide: characterization of [Fe(TpivPP)(NO₂)(CO)]. *Inorg. Chem.* **2004**, *43*, 2932-2942.

48. Nasri, H.; Ellison, M. K.; Krebs, C.; Huynh, B. H.; Scheidt, W. R., Highly variable pi-bonding in the interaction of iron(II) porphyrinates with nitrite. *J. Am. Chem. Soc.* **2000**, *122* (44), 10795-10804.
49. Hartshorne, S.; Richardson, D. J.; Simon, J., Multiple haem lyase genes indicate substrate specificity in cytochrome *c* biogenesis. *Biochem. Soc. Trans.* **2006**, *34* (Pt 1), 146-149.
50. Almeida, M. G.; Silveira, C. M.; Guigliarelli, B.; Bertrand, P.; Moura, J. G.; Moura, I.; Leger, C., A needle in a haystack: the active site of the membrane-bound complex cytochrome *c* nitrite reductase. *FEBS Lett.* **2007**, *581*, 284-288.
51. Clarke, T. A.; Hemmings, A. M.; Burlat, B.; Butt, J. N.; Cole, J. A.; Richardson, D. J., Comparison of the structural and kinetic properties of the cytochrome *c* nitrite reductases from *Escherichia coli*, *Wollinella succinogenes*, *Sulfurospirillum deleyianum*, and *Desulfovibrio desulfuricans*. *Biochem. Soc. Trans.* **2006**, *34*, 143-145.
52. Rahaman, M.; Ali, M. S.; Jahan, K.; Hinz, D.; Belayet, J. B.; Majinski, R.; Hossain, M. M., Synthetic Scope of Brønsted Acid-Catalyzed Reactions of Carbonyl Compounds and Ethyl Diazoacetate., *J. Org. Chem.* 2021, *86*, 6138–6147.
53. Stach, P.; Einsle, O.; Schumacher, W.; Kurun, E.; Kroneck, P. M. H., Bacterial cytochrome *c* nitrite reductase: new structural and functional aspects. *J. Inorg. Biochem.* **2000**, *79*, 381-385.
54. Stein, N. Spectroscopic and electrochemical studies of *Shewanella oneidensis* cytochrome *c* nitrite reductase, and improving *c*-heme expression systems. Ph.D., University of Wisconsin-Milwaukee, Dept. of Chemistry and Biochemistry, Milwaukee, WI, 2014.

Chapter 2

Purification and Preliminary Characterization of the ccNiR R103Q Variant

2.1. Overview

As was shown in Fig. 1.3, bacterial ccNiRs contain three strictly conserved active site amino acids, R103, Y206, and H257.² The theoretical studies of Bykov and Neese,³⁻⁶ together with earlier studies on ccNiR variants,⁷⁻⁹ support the presumption that these residues are essential in providing a finely tuned acidic environment for binding, orienting and reducing the negatively charged nitrite substrate. However, experimental studies done to date have invariably used strongly reducing conditions to study the variants' nitrite reductase activity, and under such conditions, catalytic intermediates don't accumulate. This chapter presents the purification and preliminary characterization of the R103QccNiR variant, which in Chapters 3-5 is studied chemically and electrochemically under mildly reducing conditions.

2.2. Materials and Methods

2.2.1. General materials

Hydroxylamine hydrochloride, sodium nitrite, Tris-HCl (99% extra pure), and Bis-Tris (ultra-pure) were purchased from Acros Organics, Ammonium sulfate (AS), EDTA and HEPES free acid and sodium salt were obtained from Fisher scientific, and Argon (high purity grade) from Airgas. All reagents used in this chapter's experiments were of high bio-grade purity and purchased from Thermo-Fisher, Dot Scientific, Millipore sigma or MP Biomedical unless mentioned specifically.

2.2.2. General instrumentation

UV/vis spectral data were collected by using Cary 50 (Varian) spectrophotometers. Two of these spectrophotometers are housed in gloveboxes. Two gloveboxes (MBraun and Innovative Technology) were used to maintain anaerobic conditions while recording UV/vis spectra or doing controlled potential electrolysis. High purity nitrogen (Airgas, 99.99 % pure), which is continually circulated through an oxygen scrubber, was used to maintain an oxygen level of less than 2 ppm in the glove box. The glovebox scrubbers were regenerated with 5% or 7% Hydrogen (Airgas) at least once a month, or whenever the oxygen level rose above 2 ppm. BASi Epsilon EC potentiostats were used to reduce required reagents at the appropriate potentials. An Ag/AgCl electrode (BASi model RE-5B) was used as the reference and was routinely calibrated against the methyl viologen midpoint potential.

2.2.3. Overview of Transformation of the R103Q mutant plasmid into *S. oneidensis* TSP-C cells

The expression system for the R103Q variant was designed by fellow graduate student Steven Reinhardt. The plasmid containing the R103Q ccNiR gene and a kanamycin resistance gene was transferred to the TSP-C strain of *S. oneidensis* by electroporation. The TSP-C strain has a rifampicin resistance gene. TSP-C cells were grown overnight (~16 hours) at 30 °C with 30 µg/mL rifampicin. Approximately 2 mL of overnight culture were spun at 4300 × g to obtain a cell pellet, washed with 500 µL 1 M sorbitol, decanted, and then resuspended in 80 µL 1M sorbitol. A 20 µL aliquot of mutant ccNiR plasmid was added to the resuspended cells, which were then electroporated at 1500 V, mixed with 800 µL of SOC growth medium, and incubated at 30 °C for 1-2 hours at 200 rpm in an incubator shaker. The newly transformed cells were incubated

overnight at 30 °C on a plate containing LB, kanamycin (50 µg/mL), and rifampicin (30 µg/mL). Only positively transformed bacteria grew on this plate, and they appeared as pink colonies. To doubly confirm the result, colony PCR was also performed, and the PCR products were loaded onto an EtBr-containing agarose gel. The presence of a new 1.5 kb band on the gel confirmed the presence of the bacterial plasmid that contained the variant. After this confirmation, the bacterial colony from the petri dish was further cultured and then stored at -80 °C in 10% glycerol for future experiments.¹

2.2.4. Large scale *S. oneidensis* harvesting and purification of the ccNiR active site variant R103Q from TSP-C cells

2.2.4.1. Bulk culture preparation and harvesting. TSP-C cells containing the R103QccNiR gene were cultured and harvested using a protocol first reported by Shahid.¹ In the first step, TSP-C cells were scraped from still-frozen stock, prepared as described in Section 2.2.3, and plated onto an LB agarose plate containing the antibiotics kanamycin (Kan 50µg/mL) and rifampicin (Rif, 30 µg/mL). The petri dish was incubated overnight at 30°C, at which point many small colonies were visible (the colonies become larger and visibly pinkish within 48 h). An isolated colony from the plate was used to inoculate 5 mL sterile LB broth containing 50 µg/mL kanamycin and 30 µg/mL rifampicin, after which the solution was incubated for 10-11 hours in an incubator shaker at 200 rpm and 30 °C. The 5mL bacterial culture was used to inoculate 1L of sterile LB broth that contained the kanamycin & rifampicin antibiotics, which in turn was incubated for 16 hours under the same conditions as used in the first step. Finally, the 1 L bacterial culture was transferred to a 50L carboy filled with 40 L water, 4 L autoclaved LB broth, kanamycin (50 µg/mL), and rifampicin (30 µg/mL), that sat in a 30 °C constant-temperature water

bath. This culture was incubated for 16 – 18 (not more than 22) hours at 30 °C, while being continually sparged with compressed air. The air served to agitate the culture suspension and to keep it aerated until late in the growth process when high bacterial density consumed oxygen faster than it could be replenished. The appropriate harvest time was usually determined by qualitative inspection (one looks for the suspension to be opaque and orange-pink, and to smell of dimethylsulfide, due to reduction of DMSO as the bacteria switch to anaerobic respiration).

The cells were harvested from the 45 L cell culture by centrifuging aliquots in 1 L bottles for 15 minutes at $5,800 \times g$. After discarding the supernatant, the cell pellets were gently scraped off the bottles with a spatula, transferred to a single large stainless-steel beaker, and resuspended using 20 mM tris buffer, pH = 8.1 (final volume ~550 mL), to which was immediately added either PMSF (0.1 - 1 mM) or AEBSF (0.1 - 1.0 mM) as a protease inhibitor. The resuspended cell pellet was frozen and stored in a -80 °C freezer until needed.

2.2.4.2. Purification of wild type and R103Q ccNiR from *S. Oneidensis* TSP-C cells.

S. oneidensis wild type ccNiR was purified from a high yield expression system using a protocol described previously.^{1, 2} R103QccNiR is tagged with a deca-His tail at the carboxy terminal.¹ Cell pellets of R103QccNiR (~300ml) from the -80°C freezer were thawed with room temperature water. An aliquot of thawed concentrated cell suspension was lysed by sonication in an ice-cooled stainless-steel beaker, using cycles of 30 s ultrasonic bursts at 70% amplitude followed by 45 s pauses, repeated for 10 minutes. The cell suspension was then centrifuged at

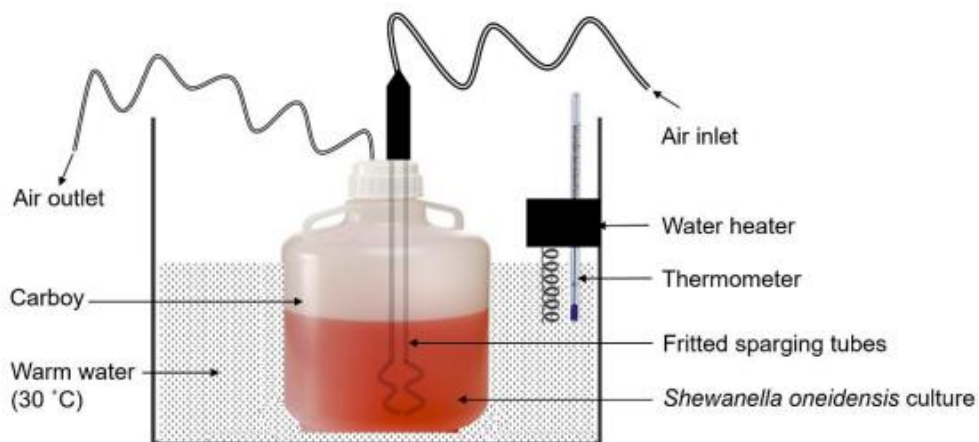


Figure 2.1. Large scale (45 L) *S. oneidensis* culture for large scale purification of R103Q ccNiR. A carboy used for this culture was immersed in a water bath. A thermostat maintained the constant optimum temperature (30 °C). To keep the culture aerated and to avoid cell settling, two fritted sparging tubes inside of the carboy provided compressed air circulation that continuously agitated the culture (Figure reproduced from ref. 1 with permission).

41,500 × g for 60 minutes to remove cell debris, after which 40 mM imidazole was added to the clarified supernatant. Next, the supernatant was loaded onto an affinity column (GE Healthcare His Trap FF, 20 mL) that had been pre-equilibrated with a buffer that contained 40 mM Imidazole,¹ 20 mM tris base, and 500 mM NaCl, adjusted to pH = 8.1 (Buffer A from Table 2.1). After the clarified cell extract had been loaded, the column was washed with 5-10 column volumes of Buffer A (Table 2.1) until the UV reading at 280 nm of the column flow-through dropped to a constant background level. The his-tagged R103QccNiR variant was eluted by mixing Buffer A with 80% of a pH 7.0 buffer containing 500 mM Imidazole, 20 mM HEPES, and 500 mM NaCl (Buffer B). All fractions for which the UV reading at 280 nm deviated significantly from the baseline were pooled and immediately transferred to Snake-Skin dialysis tubes (9 mL /1 cm, ThermoFisher) for roughly 4-5 hours of dialysis at 4 °C in an imidazole-free buffer reservoir (20 mM HEPES, 500 mM NaCl, pH = 7.0; Buffer C). The His-tag was removed by

Table 2.1. Summary of buffers that were used for column chromatography, dialysis, and storage in R103Q purification.

Purification step	Buffers used (buffer name & concentration)
1. GE Healthcare HisTrap FF chromatography column (20 mL)	Loading buffer: 40 mM Imidazole, 20 mM tris base, and 500 mM NaCl, pH=8.1 (buffer A) Elution buffer: 500 mM Imidazole, 20 mM HEPES, and 500 mM NaCl pH=7 (buffer B)
2. GE Healthcare HisTrap FF chromatography column (5 mL)	25 mM tris, 300 mM NaCl, pH = 8.0 (buffer E)
3. Sephacryl-S200, GE Healthcare, Size Exclusion Chromatography (320 mL)	50 mM HEPES, 150 mM NaCl, pH = 7.0 (buffer F)
4. Dialysis buffer 1	20 mM HEPES, 500 mM NaCl, pH = 7.0 (buffer C)
5. Dialysis buffer 2	50 mM Tris, 100 mM NaCl, 1 mM DTT, 250 μ M EDTA, pH 8.0 (buffer D)
5. Storage buffer	50 mM HEPES at pH = 7.0 (buffer G)

incubating the protein with Tobacco etch virus (TEV) protease. TEV protease was added to the dialysis tube containing the R103Q variant according to the rule of thumb protocol of adding 1.0 O.D. TEV protease to 10 O.D. mutant ccNiR.¹ The dialysis tube was then transferred into another buffer reservoir (50 mM Tris, 100 mM NaCl, 1 mM DTT, 250 μ M EDTA, pH = 8.0; Buffer D) which was an optimum buffer for TEV protease activity. The digestion of His-tag by TEV protease was continued overnight at 4 °C. The digested protein solution was centrifuged at 41,500 \times g for 10

min and the supernatant was collected. A small HisTrap FF column (5 mL, GE Healthcare) was equilibrated with a buffer containing 25 mM tris, 300 mM NaCl, pH = 8.0 (Buffer E), after which the clarified protein solution was loaded onto it. This column captured undigested R103Q ccNiR and the TEV protease, which is also His-tagged, but allowed the R103Q ccNiR from which the His-tag had been successfully cleaved to pass through. The buffer from the flow-through was exchanged for a buffer containing 50 mM HEPES, 150 mM NaCl, pH = 7.0 (Buffer F), and then concentrated using centrifugal concentrators (Amicon) spun at 4,000 g for 10 min intervals. Size exclusion chromatography (SEC, Sephacryl-S200, GE Healthcare) was used as the final step of purification. The SEC column (320 mL) was equilibrated with Buffer F and then loaded with a concentrated R103QccNiR sample (not more than 2.5 mL). Two distinct UV280 peaks were observed in the chromatograph. The second of these displayed a UV/Vis ratio $A_{409}/A_{280} > 3.8$ and was confirmed to be the pure R103Q ccNiR by SDS-PAGE. The pure protein's buffer was exchanged for 50 mM HEPES at pH = 7.0, after which the solution was concentrated using centrifugal concentrators and stored at -80°C .¹

2.2.5. Pyridine hemochrome assay

Heme concentrations in ccNiR solutions were determined using a variation of the pyridine hemochrome assay methodology described by Berry and Trumpower,¹⁰ and Barr and Guo.¹¹ Briefly, 10 μL of a 0.1 M potassium ferricyanide solution was mixed with 800 μL of 0.5 M NaOH, 800 μL of pyridine (Anhydrous, 99.8% pure, Sigma-Aldrich) and 390 μL nano-pure water to make 2 mL of Solution I. The final concentrations in Solution I were 500 μM $\text{Fe}(\text{CN})_6^{3-}$, 0.2 M NaOH and 40% v/v pyridine. A solution containing equal volumes of Solution I and 50 mM HEPES buffer, pH

7, was used to set the baseline for the UV/Vis spectrophotometer. CcNiR samples were dissolved in a 50 mM HEPES buffer, pH = 7.0, to make Solution II. Equal volumes of Solution I and Solution II were mixed in a cuvette, and the UV/Vis spectrum was recorded in the range 450 nm – 800 nm. This was the oxidized pyridine hemochrome sample and was labeled as Dataset-1. A few grains of solid sodium dithionite (sodium hydrosulfite) were added into the cuvette, the solution was carefully mixed, and then several UV/Vis spectra were recorded at 30 s intervals until the spectra remained unchanged. The final spectrum was the reduced pyridine hemochrome sample and was labeled as Dataset-2; the reduced solution is distinctly pink, compared to the orange oxidized pyridine hemochrome. The difference spectrum (Dataset-2) – (Dataset-1) was fit in the range from 525 nm – 620 nm using the known extinction coefficient difference spectrum¹⁰ to determine the concentration of pyridine hemochrome in solution.

2.2.6. Methyl viologen assays of ccNiR nitrite reduction activity

R103Q ccNiR's ability to catalyze nitrite reduction was compared to that of wild type ccNiR and other variants using what is effectively the standard assay for ccNiR, in which methyl viologen monocation radical, MV_{red} , $\epsilon_m^\circ = -0.449$ V vs SHE,¹² serves as the electron donor. The blue MV_{red} was prepared by applying a potential of -0.800 V vs SHE to a solution of methyl viologen (1,1'-dimethyl-4,4'-bipyridinium dication, MV_{ox}) in a bulk electrolysis cell; an Ag/AgCl electrode was used as a reference electrode. CcNiR-catalyzed reduction of nitrite by MV_{red} was carried out under anaerobic conditions in a glove box. Experiments were carried out in 50 mM HEPES, pH 7.0; nitrite, MV_{red} , and ccNiR concentrations were systematically varied from one experiment to the next in order to probe the reaction rate's dependence on these concentrations. Nitrite concentrations were varied from 0 – 4 mM, MV_{red} concentrations from 0 – 100 μ M, and ccNiR

concentrations from 70-100 pM (wtccNiR) or from 0.4 – 1.2 nM (R103QccNiR). Experiments with a given set of nitrite and MV_{red} concentrations were performed in the presence and absence of enzyme (blank reaction). MV_{red} reacts with nitrite even in the absence of ccNiR, so the uncatalyzed contribution was measured in the blank experiments and subtracted. MV_{red} oxidation was monitored by UV/Vis spectroscopy in the range from 400 nm to 800 nm; spectra were collected at 15 s intervals for 3 – 5 minutes. MV_{red} exists as a mixture of monomer and dimer (MV_{red})₂ in proportions that vary with total MV_{red} concentration and monitoring the 400 nm-800 nm visible range allowed the contributions from each species to be distinguished. In all experiments involving MV_{red} oxidation, the rate of change in total MV_{red} is reported, where (MV_{red})_{tot} = MV_{red} + 2(MV_{red})₂. The monomer and dimer concentrations were deconvoluted using a program written in the commercially available software package Mathcad 15 (PTC). Replots of initial MV_{red} oxidation rate vs nitrite, MV_{red}, or ccNiR concentrations were graphed and analyzed in Microcal Origin (Version 9.1).

2.2.7. Methyl viologen assays of ccNiR hydroxylamine reduction activity

As mentioned earlier, ccNiR catalyzes the 6-electron reduction of nitrite to ammonium and 2-electron reduction of hydroxylamine to ammonium. R103Q ccNiR's ability to catalyze hydroxylamine reduction was compared to that of wild type ccNiR and other variants using the MV_{red} assay described above, but with one modification. As will be seen, the K_m value for hydroxylamine is high, which necessitated the use of up to 200 mM hydroxylamine to determine hydroxylamine's effect on catalysis rates. As hydroxylamine is a weak base, it becomes part of the buffer at concentrations higher than a few millimolar, which complicates pH regulation. To address this problem, hydroxylamine solutions were prepared by a method first described by

Youngblut et al.¹³ Aliquots of hydroxylamine hydrochloride (pK_a 6.03) and NaHEPES (sodium 2-[4-(2-hydroxyethyl) piperazin-1-yl] ethane-1-sulfonate; HEPES pK_a 7.4) stock solutions were mixed in 1:1.2 mole ratios to give final solutions containing the desired hydroxylamine concentration. Varying amounts of sodium chloride were also added to the solutions to maintain the ionic strength constant at 0.3 M. The pHs of solutions prepared in this way were close to 7.0 for a wide range of hydroxylamine concentrations. The data were analyzed using the same procedures described for the nitrite reduction assays in Section 2.2.6.

2.3. Results

2.3.1. Pyridine Hemochrome assay determination of the R103QccNiR extinction coefficient

Figure 2.2 outlines how the pyridine hemochrome assay is used to quantify the amount of heme present in a solution of heme-containing protein.^{10, 11} The heme protein is denatured by adding an alkaline pyridine solution. For *a* and *b* hemes, the heme is completely extruded from the denatured protein, and the amino acid axial ligands from the protein are replaced by pyridines. For *c*-heme proteins such as ccNiR, the hemes retain the thioether linkages with the denatured protein, but the native axial ligands are still replaced by pyridines. The bis-pyridine ligated heme obtained in the alkaline pyridine solution is called the “pyridine hemochrome”; *a*, *b*, and *c* pyridine hemochromes each have distinctive UV/Vis spectra whose extinction coefficients are known,¹⁰ so once the spectrum of a pyridine hemochrome solution has been obtained, the heme concentration in it can be ascertained. Figure 2.3 shows the visible extinction coefficient spectra of oxidized and reduced *c*-type pyridine hemochrome, along with the reduced – oxidized difference spectrum;¹⁰ the difference spectrum was used to obtain the concentration

of pyridine hemochrome solutions because it is less prone to errors from baseline drift than either the oxidized or reduced spectrum alone. Figure 2.4 shows an example of a reduced – oxidized difference spectrum of pyridine hemochrome derived from ccNiR, fit with the known – extinction coefficient difference spectrum of *c*-heme pyridine hemochrome.¹⁰ A matrix form of Beer’s law was used to obtain the pyridine hemochrome concentration from the fit.

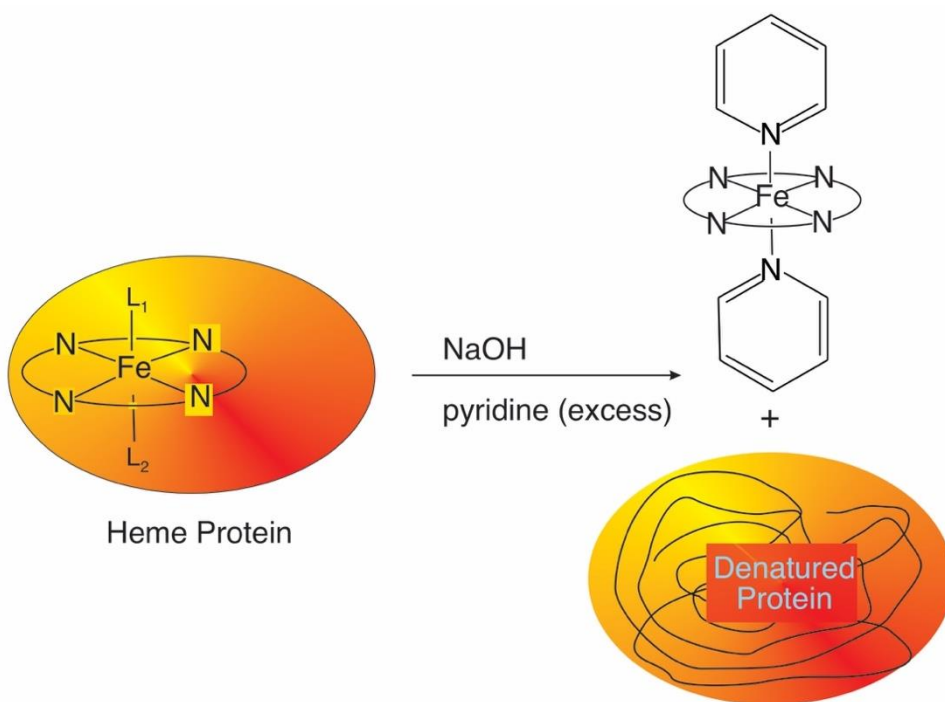


Figure 2.2. Outline of the pyridine hemochrome assay procedure. The bis-pyridine ligated heme obtained in the alkaline pyridine solution is called the “pyridine hemochrome”.¹⁰

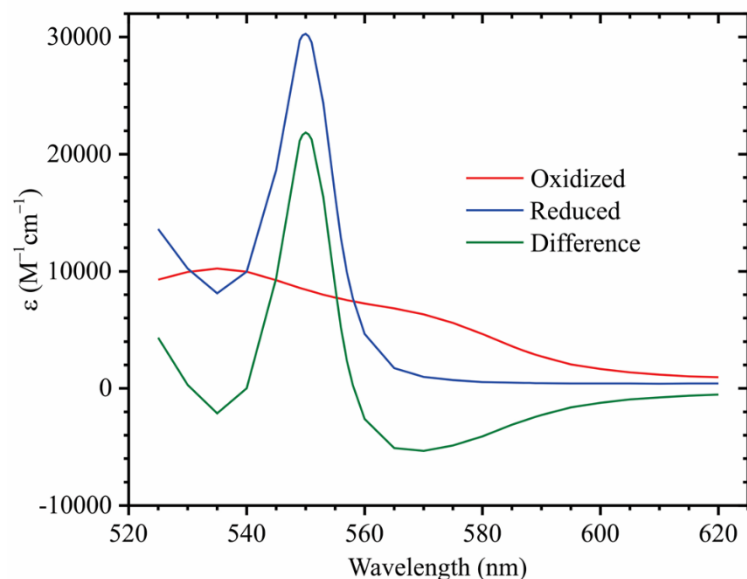


Figure 2.3. Extinction coefficient spectra of oxidized and reduced *c*-heme pyridine hemochrome, along with the reduced – oxidized extinction coefficient difference spectrum. Generated from the data tables provided in ref. ¹⁰.

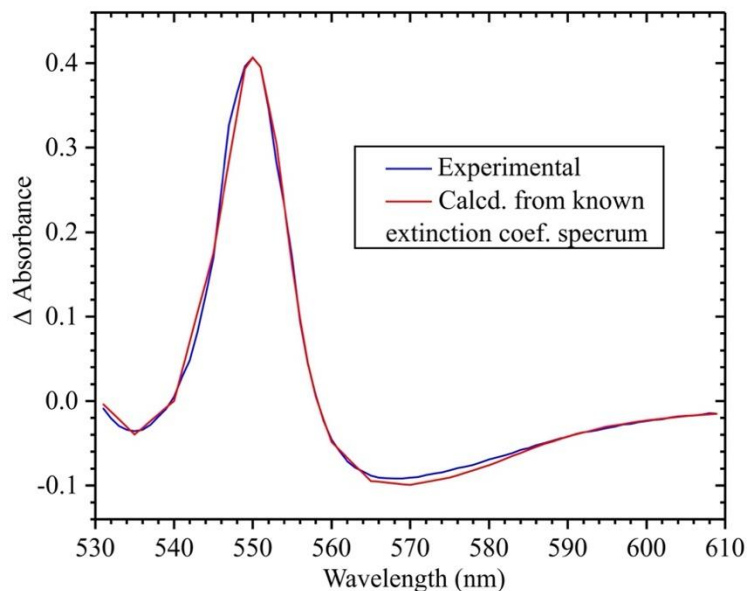
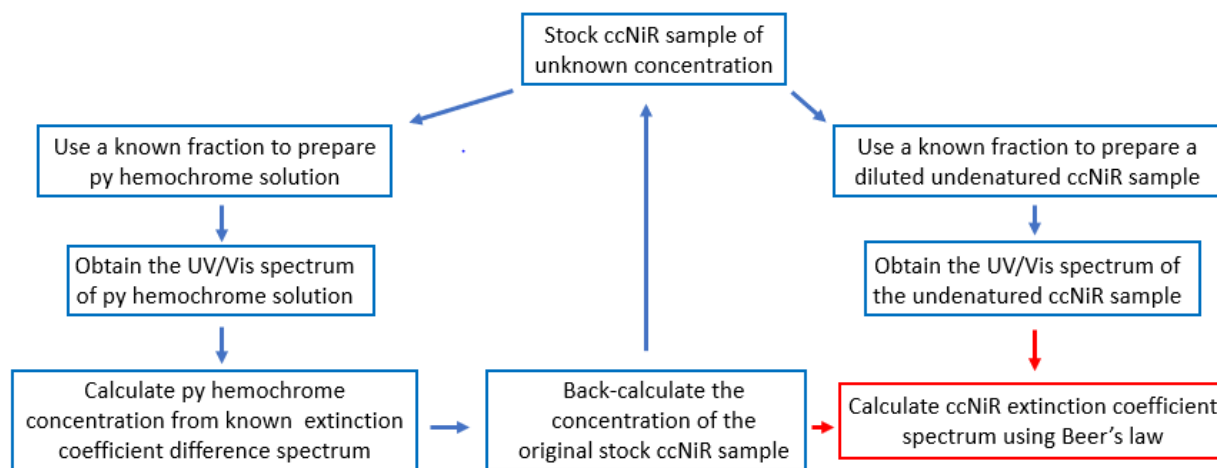


Figure 2.4. Reduced – oxidized difference spectrum of pyridine hemochrome derived from ccNiR, fit with the known extinction coefficient difference spectrum of *c*-heme pyridine hemochrome.¹⁰ The pyridine hemochrome concentration was obtained from the fit.

The traditional pyridine hemochrome assay uses only the difference between reduced and oxidized absorbance at the 550 nm reduced absorbance maximum. However, fitting the entire difference spectrum has the enormous advantage of revealing baseline shifts, or the presence of absorbing species other than pyridine hemochrome, which single-point measurements don't detect. For our ccNiR experiments, the spectral fits were uniformly excellent, as seen in Fig. 2.4, confirming that the pyridine hemochrome was the only absorbing species in solution.

Scheme 2.1 outlines how the pyridine hemochrome assay was used to obtain the extinction coefficient spectra of undenatured ccNiR and its variants. The scheme has two branches. Along the left-hand branch, an aliquot from a stock ccNiR solution was diluted and then denatured as described in Fig. 2.2, after which the spectra of the oxidized and reduced



Scheme 2.1. Flow chart that outlines the procedure for calculating the ccNiR extinction coefficient spectrum.

pyridine hemochrome were obtained as described in Section 2.2.5 and used to generate the reduced – oxidized difference spectrum. This was fit with the known reduced – oxidized extinction coefficient difference spectrum of *c*-heme pyridine hemochrome, to obtain the pyridine hemochrome concentration, as described above. Once the pyridine hemochrome concentration was known, it was used to back-calculate the heme concentration of the original ccNiR stock solution. At this point, one must remember that ccNiR contains five hemes per protomer, therefore, the calculated heme concentration was divided by 5 to obtain the ccNiR protomer concentration in solution. Furthermore, as ccNiR is a dimer, the protomer concentration must be divided by two if one chooses to report the ccNiR dimer concentration.

To obtain the extinction coefficient spectrum of undenatured ccNiR (right branch, Scheme 2.1), an aliquot of the stock solution, now of known concentration, was diluted in HEPES buffer pH 7 such that the Soret band absorbance (409 nm) was ≤ 1.0 , after which the UV/Vis spectrum was recorded from 250 nm – 800 nm. As the ccNiR concentration was known from the pyridine hemochrome assay, the extinction coefficient spectrum was readily obtained by dividing the absorbance obtained between 250 nm and 800 nm by the concentration and path length (Beer's law). Figure 2.5a compares the R103QccNiR extinction coefficient spectrum with that of the wild type, while Fig. 2.5b plots the difference between the two spectra. As can be seen, the spectra are broadly comparable, though the R103QccNiR Soret band has slightly lower maximum intensity than the wild type ($\lambda_{\text{max}}(409\text{nm}) = 5.4 \times 10^5 \text{ M}^{-1}\text{cm}^{-1}$ for R103QccNiR, compared to $5.6 \times 10^5 \text{ M}^{-1}\text{cm}^{-1}$ for wild type). Notably, very little difference is detectable above

600 nm, where high-spin and low-spin hemes typically show distinct charge transfer bands.⁹ This suggests that the R103QccNiR and wild type ccNiR active sites have the same spin states.

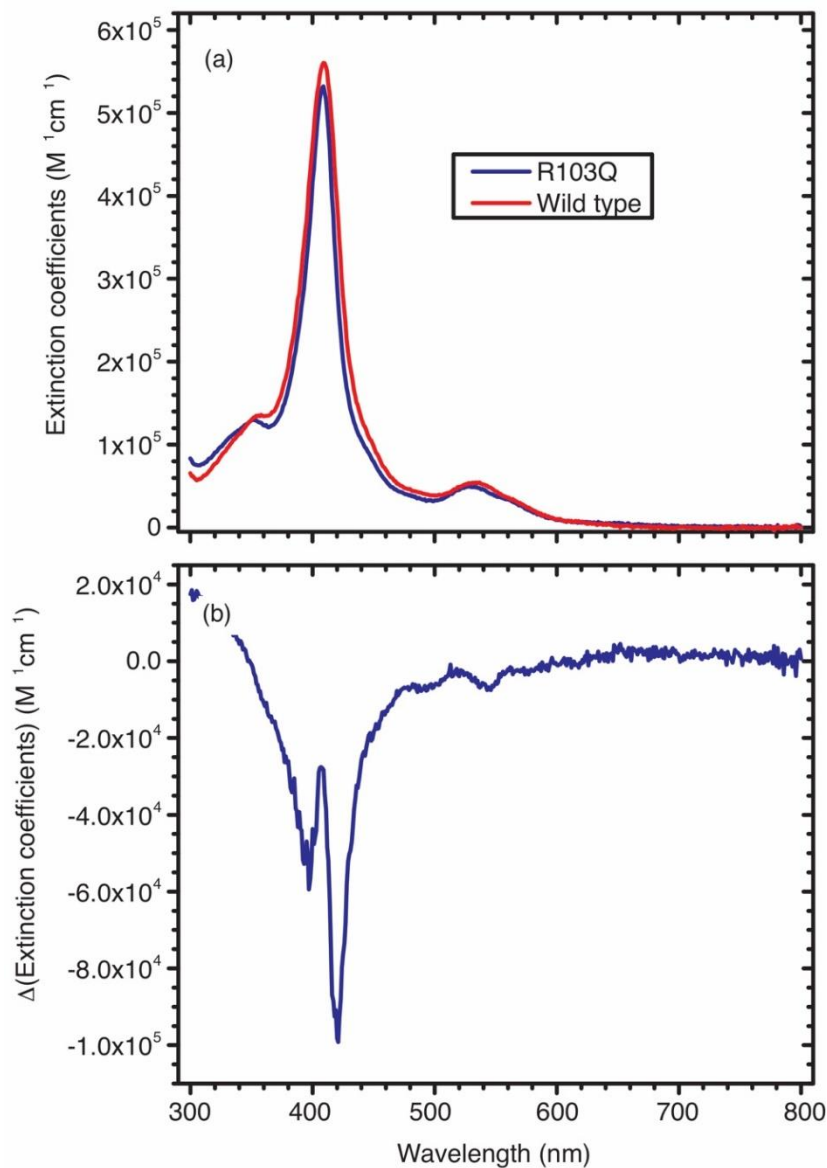


Figure 2.5. (a) Comparison between the R103QccNiR extinction coefficient spectrum (blue line) and that of wtccNiR (red line). (b) $\epsilon(R103QccNiR) - \epsilon(wtccNiR)$ difference spectrum.

2.3.2. Dependence on MV_{red} concentration of ccNiR-catalyzed reduction of nitrite by MV_{red}

The initial rate of ccNiR-catalyzed reduction of nitrite by MV_{red} at fixed nitrite and MV_{red} concentrations depends linearly on wtccNiR concentration,¹⁴ and the same is true for the R103QccNiR-catalyzed process. For convenience, we define a parameter $k_{app} \equiv V_0/[ccNiR]$, where V_0 is the initial rate of MV_{red} oxidation and [ccNiR] is the concentration of either wtccNiR or R103QccNiR, depending on the system under study. Figures 2.6 and 2.7 then show the dependence of k_{app} on [MV_{red}] for wtccNiR and R103QccNiR, respectively. As can be seen from the figures, the value of k_{app} is independent of [MV_{red}] within the studied range. Presumably, at sufficiently low MV_{red} concentrations, k_{app} would show hyperbolic dependence on [MV_{red}] (Michaelis-Menten-type behavior, Eq. 2.1). However, one can estimate that any K_{m1} value

$$k_{app} = \frac{k_{cat1}[MV_{red}]}{K_{m1} + [MV_{red}]} \quad \text{Eq. 2.1}$$

associated with dependence on [MV_{red}] must be less than 1-5 μM by reasoning that, if K_{m1} were higher, a drop in k_{app} would be detectable at 20 μM [MV_{red}]. For example, if K_{m1} were 10 μM , k_{app} at 20 μM [MV_{red}] should be only 66% of its maximum value (Eq. 2.1), a drop in k_{app} that should be readily detectable.

The average value of k_{app} for R103QccNiR-catalyzed reduction in the 20 – 100 μM [MV_{red}] range was $480 \pm 30 \text{ s}^{-1}$ (Fig. 2.7), which is about 15% of the wild type k_{app} in the same concentration range ($3600 \pm 850 \text{ s}^{-1}$, Fig. 2.6). This is a significant loss of activity, demonstrating the importance of Arg103 to ccNiR's catalytic function.

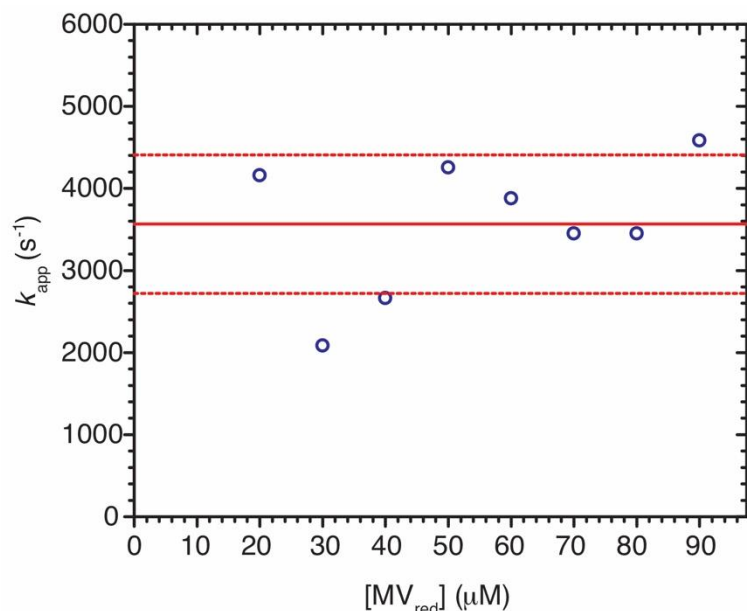


Figure: 2.6. WtccNiR-catalyzed reduction of nitrite by MV_{red} at varying MV_{red} concentrations ($k_{app} \equiv V_0/[ccNiR]$). Blue circles are the experimentally obtained values at each MV_{red} concentration. This set of experiments was performed at pH 7.0 in the presence of 70 pM - 100 pM wtccNiR and 0-100 μM MV_{red}. The solid red line was obtained by averaging the k_{app} values, while the dashed lines represent the standard deviation from the average ($k_{app} = 3600 \pm 850 \text{ s}^{-1}$).

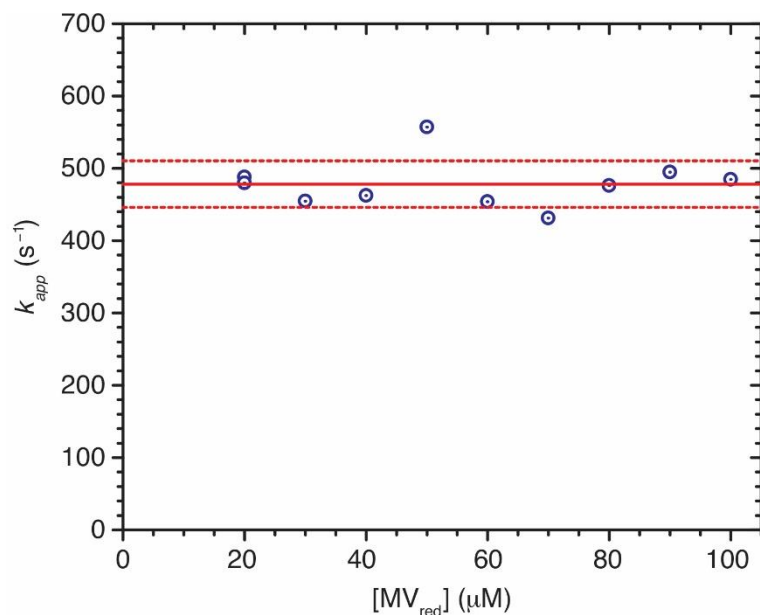


Figure: 2.7. R103QccNiR-catalyzed reduction of nitrite by MV_{red} at varying MV_{red} concentrations. Red circles are the experimentally obtained values at each MV_{red} concentration. This set of experiments was performed at pH 7.0 in the presence of 0.4-1.1 nM R103QccNiR, 0-100 μM MV_{red}, and 1mM nitrite. The solid red line was obtained by averaging the k_{app} values, while the dashed lines represent the standard deviation from the average ($k_{app} = 480 \pm 30 \text{ s}^{-1}$).

2.3.3. Dependence on nitrite concentration of ccNiR-catalyzed reduction of nitrite by MV_{red}

Figures 2.8 and 2.9 show the dependence on [NO₂⁻] of wtccNiR- and R103QccNiR-catalyzed reduction of nitrite by MV_{red}, respectively. As with Figs. 2.6 and 2.7, the graphs plot k_{app} as the ordinate (section 2.3.2), this time with [NO₂⁻] as the abscissa. In both cases, k_{app} shows hyperbolic dependence on [NO₂⁻], and the data were fit with Eq. 2.2 (red trace, Figs. 2.8,

$$k_{app} = \frac{k_{cat2}[\text{NO}_2^-]}{K_{m2} + [\text{NO}_2^-]} \quad \text{Eq. 2.2}$$

2.9). Figure 2.9 shows that both k_{cat2} and K_{m2} for R103QccNiR are significantly different from the wild type values. The R103QccNiR k_{cat1} value is about 20% that of the wild type ($780 \pm 50 \text{ s}^{-1}$ compared to $4510 \pm 90 \text{ s}^{-1}$), while that of the K_{m1} value is about 20 times higher ($(4.7 \pm 0.9) \times 10^{-4} \text{ M}$ compared to $(2.4 \pm 0.6) \times 10^{-5} \text{ M}$). This shows that Arg103 is important both for accelerating the reduction of bound nitrite and for stabilizing the interaction between nitrite and ccNiR.

2.3.4. Dependence on hydroxylamine concentration of ccNiR-catalyzed reduction of hydroxylamine by MV_{red}

In addition to catalyzing the 6-electron reduction of nitrite to ammonia by MV_{red}, wtccNiR also catalyzes the 2-electron reduction of hydroxylamine to ammonia.¹⁴ Figures 2.10 and 2.11 show how the dependence on [NH₂OH] of R103QccNiR-catalyzed reduction of hydroxylamine by MV_{red} compares to that of wtccNiR. As with Figs. 2.6 - 2.9, the graphs plot k_{app} as the ordinate (section 2.3.2), this time with [NH₂OH] as the abscissa. In both cases, k_{app} shows hyperbolic dependence on [NH₂OH], and the data are fit with Eq. 2.3. Figure

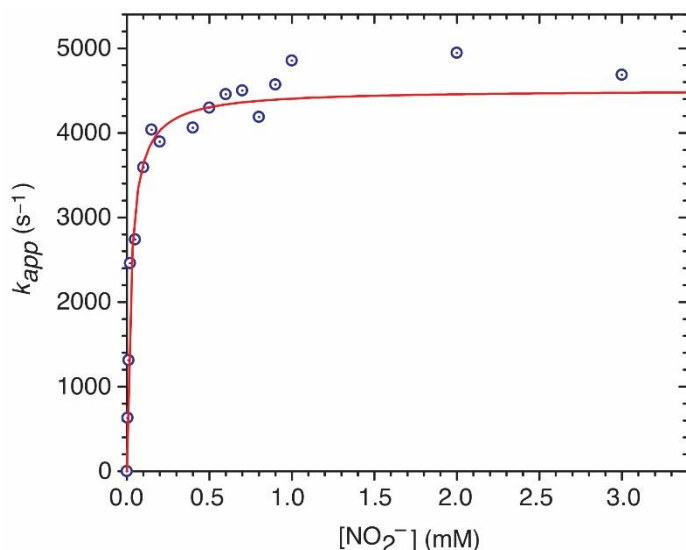


Figure 2.8. WtccNiR-catalyzed reduction of nitrite by MV_{red} at varying nitrite concentrations. Blue circles are the experimentally obtained values at each nitrite concentration, while the red curve is the least-squares fit of the data to the rectangular hyperbola Eq 2.2. This set of experiments was performed at pH 7.0 in the presence of 54 pM wtccNiR and 100 μ M MV_{red}. The least-squares fit yielded the parameter values $K_{m2} = (2.4 \pm 0.6) \times 10^{-5}$ M, $k_{cat2} = 4510 \pm 90$ s⁻¹ ($k_{app} \equiv V_0/[ccNiR]$; Section 2.3.2).

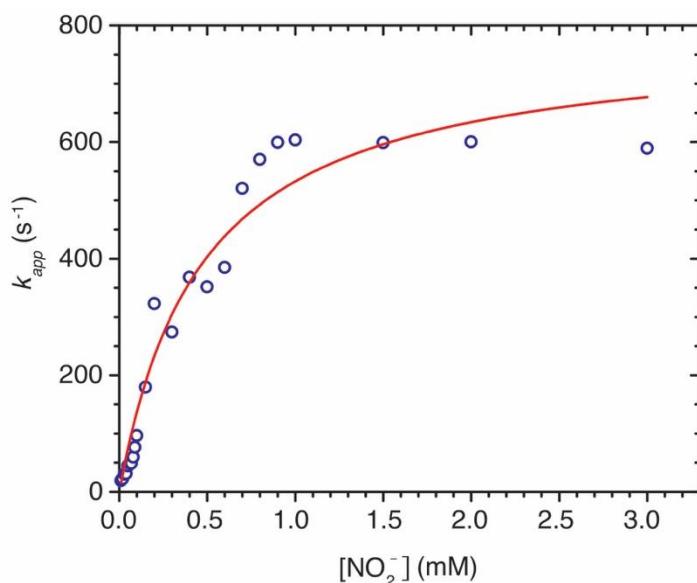


Figure 2.9. R103QccNiR-catalyzed reduction of nitrite by MV_{red} at varying nitrite concentrations. Blue circles are the experimentally obtained values at each nitrite concentration, while the red curve is the least-squares fit of the data to the rectangular hyperbola Eq 2.2. This set of experiments was performed at pH 7.0 in the presence of 10-110 nM R103QccNiR and 100 μ M MV_{red}. The least-squares fit yielded the parameter values $K_{m2} = (4.7 \pm 0.9) \times 10^{-4}$ M and $k_{cat2} = 780 \pm 50$ s⁻¹ ($k_{app} \equiv V_0/[ccNiR]$; Section 2.3.2).

$$k_{app} = \frac{k_{cat3}[\text{NH}_2\text{OH}]}{K_{m3} + [\text{NH}_2\text{OH}]} \quad \text{Eq. 2.3}$$

2.11 shows that the R103QccNiR k_{cat3} for hydroxylamine reduction is about 20% of the wild type value ($600 \pm 30 \text{ s}^{-1}$ compared to $3100 \pm 300 \text{ s}^{-1}$), a decrease similar to that seen for nitrite reduction. On the other hand, the K_{m3} value for hydroxylamine reduction is essentially identical for R103QccNiR and wtccNiR ($(2.7 \pm 0.5) \times 10^{-2} \text{ M}$ vs. $(2.1 \pm 0.7) \times 10^{-2} \text{ M}$). Both values are very high though, suggesting that the ccNiR active site is not optimized for hydroxylamine binding, even in the wild type.

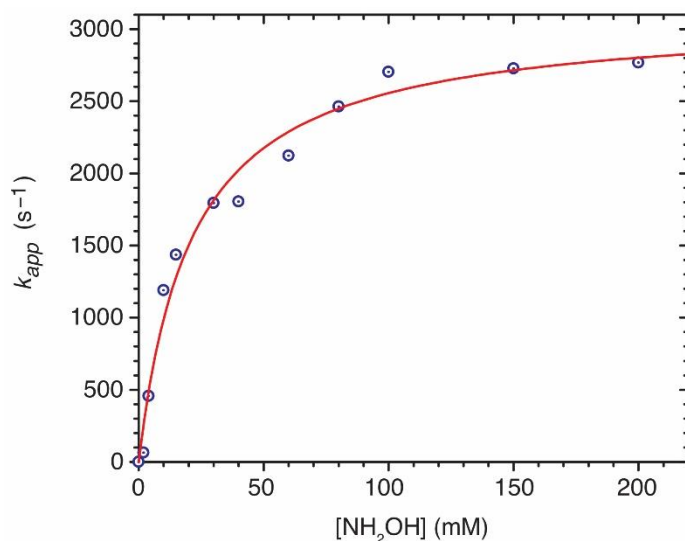


Figure 2.10. WtccNiR-catalyzed reduction of hydroxylamine by MV_{red} at varying hydroxylamine concentrations. Blue circles are the experimentally obtained values at each hydroxylamine concentration, while the red curve is the least-squares fit of the data to the rectangular hyperbola Eq 2.3. This set of experiments was performed at pH 7.0 in the presence of 22 pM wtccNiR and 100 μM MV_{red}. The least-squares fit yielded the parameter values $K_{m3} = (2.1 \pm 0.7) \times 10^{-2} \text{ M}$ and $k_{cat3} = 3100 \pm 300 \text{ s}^{-1}$; ($k_{app} \equiv V_0/[\text{ccNiR}]$; Section 2.3.2).

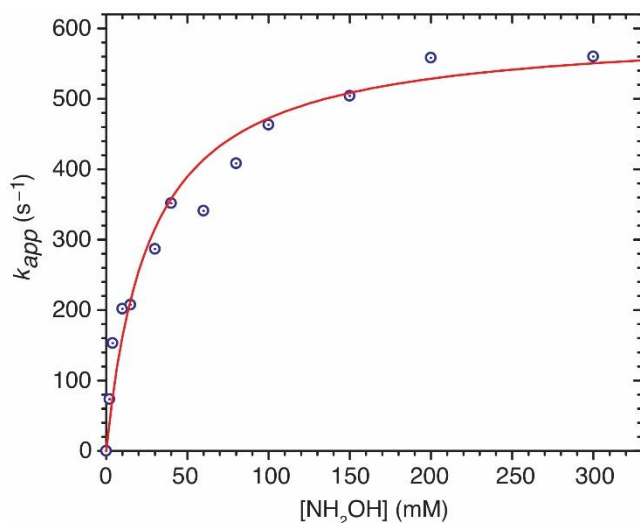


Figure 2.11. R103QccNiR-catalyzed reduction of hydroxylamine by MV_{red} at varying hydroxylamine concentrations. Blue circles are the experimentally obtained values at each hydroxylamine concentration, while the red curve is the least-squares fit of the data to the rectangular hyperbola Eq 2.3. This set of experiments was performed at pH 7.0 in the presence of 120 pM R103QccNiR and 100 μ M MV_{red}. The least-squares fit yielded the parameter values $K_{m3} = (2.7 \pm 0.5) \times 10^{-2}$ M and $k_{cat3} = 600 \pm 30$ s⁻¹; ($k_{app} \equiv V_0/[ccNiR]$; Section 2.3.2).

2.4. Discussion

The schematic reaction pathway shown in Fig. 1.4 suggests that the rate limiting step for nitrite reduction to ammonium is the final 2-electron reduction of what is formally a hydroxylamine bound at the heme 1 active site. In Fig. 1.4, this is represented by the large activation barrier after an as-yet unspecified 4-electron reduced intermediate (question mark in Fig. 1.4). An important piece of evidence for the proposed rate limiting step is that, for wtccNiR, k_{cat} for nitrite and hydroxylamine reduction are comparable, suggesting a shared choke point. In this work, k_{cat3} for hydroxylamine reduction was measured at about 70% that of k_{cat2} nitrite reduction (Figs. 2.8 and 2.10); however, these parameters for the *S. oneidensis* enzyme have been

independently measured multiple times in our laboratory over the years,¹⁴ and the cumulative results suggest that k_{cat2} and k_{cat3} have identical values (roughly $4000 \pm 1000 \text{ s}^{-1}$). Moreover, the k_{cat2} and k_{cat3} values for the *S. oneidensis* enzyme are also comparable to those obtained for the *E. coli* homologue.¹⁵

Tables 2.2 and 2.3 summarize the Michaelis-Menten parameters obtained for nitrite and hydroxylamine reduction by MV_{red} , catalyzed by R103QccNiR, as well as by wtccNiR and the variant H257QccNiR; the parameters for the H257Q variant were obtained by former Pacheco graduate student Shahid Shahid.¹ Note that k_{cat2} and k_{cat3} for R103QccNiR have comparable values ($690 \pm 90 \text{ s}^{-1}$), and that both have been reduced to $\sim 20\%$ of the wild type values ($3800 \pm 700 \text{ s}^{-1}$). Based on the Fig. 1.4 mechanism, this suggests that mutation of Arg103 disrupts the rate limiting final 2-electron reduction step. By contrast, mutation of His257 almost completely shuts down reduction of nitrite (k_{cat2} for H257Q is $\sim 0.25\%$ of the wild type value), but has a minor effect on reduction of hydroxylamine (k_{cat3} for H257Q is $\sim 66\%$ of the wild type value). This suggests that His257 is essential for catalyzing the initial steps of nitrite reduction but is less important than Arg103 for facilitating the final 2-electron reduction. Work by Shahid,¹ together with computational studies by Bykov and Neese,³ suggested that H257's key role is to protonate one of the nitrite oxygens so that it can be removed as water in the first 2-electron reduction of bound nitrite (Section 1.3.2).

Table 2.2. Parameters k_{cat2} and K_{m2} (Eq. 2.2) obtained for nitrite reduction by MV_{red} catalyzed by wtccNiR and two variants.

	k_{cat2} (s ⁻¹)	K_{m2} (M)
wtccNiR	4510 ± 90	(2.4 ± 0.6)×10 ⁻⁵
R103QccNiR	780 ± 50	(4.7 ± 0.9)×10 ⁻⁴
H257QccNiR ^a	11.3±0.6	(1.5 ± 0.3)×10 ⁻⁴

^a. Data from ref. 1

Table 2.3. Parameters k_{cat3} and K_{m3} (Eq. 2.3) obtained for hydroxylamine reduction by MV_{red} catalyzed by wtccNiR and two variants.

	k_{cat3} (s ⁻¹)	K_{m3} (M)
wtccNiR	3110 ± 300	(2.1 ± 0.7)×10 ⁻²
R103QccNiR	600 ± 30	(2.7 ± 0.6)×10 ⁻²
H257QccNiR ^a	2050±140	(2.1 ± 0.5)×10 ⁻²

^a. Data from ref. 1

Table 2.2 shows that K_{m2} is significantly higher for both R103Q and H257Q than it is for wtccNiR, demonstrating that both amino acid residues play important roles in stabilizing nitrite in the active site, though R103QccNiR is more profoundly affected ($K_{m2} \sim 20\times$ higher than for wtccNiR, compared to $\sim 6\times$ higher for H257Q). Table 2.3 shows that K_{m3} is comparable for wtccNiR and the two variants. In all cases though, K_{m3} is very high (~ 0.02 M), suggesting that ccNiR is not optimized for tight binding of hydroxylamine.

2.5. References

1. Shahid, S. A mechanistic investigation of cytochrome c nitrite reductase catalyzed reduction of nitrite to ammonia: the search for catalytic intermediates. University of Wisconsin-Milwaukee, Milwaukee, WI, 2020.
2. Ali, M.; Stein, N.; Mao, Y.; Shahid, S.; Schmidt, M.; Bennett, B.; Pacheco, A. A., Trapping of a putative intermediate in the cytochrome c nitrite reductase (ccNiR)-catalyzed reduction of nitrite: implications for the ccNiR reaction mechanism *J. Am. Chem. Soc.* **2019**, *141*, 13358-13371.
3. Bykov, D.; Neese, F., Substrate binding and activation in the active site of cytochrome c nitrite reductase: a density functional study. *J. Biol. Inorg. Chem* **2011**, *16*, 417-430.
4. Bykov, D.; Neese, F., Reductive activation of the heme iron-nitrosyl intermediate in the reaction mechanism of cytochrome c nitrite reductase: a theoretical study. *J. Biol. Inorg. Chem.* **2012**, *17* (5), 741-760.
5. Bykov, D.; Plog, M.; Neese, F., Heme-bound nitroxyl, hydroxylamine, and ammonia ligands as intermediates in the reaction cycle of cytochrome c nitrite reductase: a theoretical study. *J. Biol. Inorg. Chem.* **2014**, *19*, 97-112.
6. Bykov, D.; Neese, F., Six-electron reduction of nitrite to ammonia by cytochrome c nitrite reductase: insights from density functional theory studies. *Inorg. Chem.* **2015**, *54*, 9303-9316.
7. Lukat, P.; Rudolf, M.; Stach, P.; Messerschmidt, A.; Kroneck, P.; Simon, J.; Einsle, O., Binding and Reduction of Sulfite by Cytochrome c Nitrite Reductase. *Biochemistry* **2008**, *47*, 2080-2086.
8. Judd, E. T.; Stein, N.; Pacheco, A. A.; Elliott, S. J., Hydrogen bonding networks tune proton-coupled redox steps during the enzymatic six-electron conversion of nitrite to ammonia. *Biochemistry* **2014**, *53*, 5638-5646.
9. Lockwood, C. W. J.; Burlat, B.; Cheesman, M. R.; Kern, M.; Simon, J.; Clarke, T.; Richardson, D. J.; Butt, J. N., Resolution of key roles for the distal pocket histidine in cytochrome c nitrite reductases. *J. Am. Chem. Soc.* **2015**, *137*, 3059-3068.
10. Berry, E. A.; Trumpower, B. L., Simultaneous determination of hemes a, b, and c from pyridine hemochrome spectra. *Anal. Biochem.* **1987**, *161*, 1-15.
11. Barr, I.; Guo, F., Pyridine hemochromagen assay for determining the concentration of heme in purified protein solutions. *Bio. Protoc.* **2015**, *5*, (18).
12. Watanabe, T.; Honda, K., Measurement of the extinction coefficient of the methyl viologen cation radical and the efficiency of its formation by semiconductor photocatalysis. *J. Phys. Chem.* **1982**, *86*, 2617-2619.
13. Youngblut, M.; Pauly, D. J.; Stein, N.; Walters, D.; Conrad, J. A.; Moran, G. R.; Bennett, B.; Pacheco, A. A., *Shewanella oneidensis* cytochrome c nitrite reductase (ccNiR) does not disproportionate hydroxylamine to ammonia and nitrite, despite a strongly favorable driving force. *Biochemistry* **2014**, *53*, 2136-2144.
14. Youngblut, M.; Judd, E. T.; Srajer, V.; Sayyed, B.; Goelzer, T.; Elliott, S. J.; Schmidt, M.; Pacheco, A. A., Laue crystal structure of *Shewanella oneidensis* cytochrome c nitrite reductase from a high-yield expression system. *J. Biol. Inorg. Chem.* **2012**, *17*, 647-662.

15. Bamford, V. A.; Angove, H. C.; Seward, H. E.; Thomson, A. J.; Cole, J. A.; Butt, J. N.; Hemmings, A. M.; Richardson, D. J., Structure and spectroscopy of the periplasmic cytochrome c nitrite reductase from *Escherichia coli*. *Biochemistry* **2002**, *41* (9), 2921-2931.

Chapter 3

Electrochemical characterization of the R103Qccnir Variant and a comparative study with wild type ccNiR

3.1. Overview

This chapter presents a UV/Vis spectropotentiometric study of the R103Qccnir variant in the presence of the physiological substrate, nitrite. It is not usually possible to do spectropotentiometry on an enzyme in the presence of the enzyme's substrate because, at some point, the enzyme will turn the substrate over so that equilibrium at a fixed potential can't be established. However, Ali et al found that it is possible to monitor initial reduction of the wtccNiR heme 1 active site in the presence of nitrite because the nitrite-loaded heme center reduces at a potential that is almost 300 mV above the potential at which significant turnover of nitrite to ammonium can take place.¹ We hoped to employ the same strategy with R103QccNiR, thus obtaining heme 1's first midpoint potential under conditions as close to physiologically relevant as possible.

3.2 Materials and methods

3.2.1. General Materials

All reagents were high bio-grade purity and used without further purification. Sodium nitrite, anthroquinone-2-sulfonic acid sodium salt monohydrate, methyl viologen hydrate, and safranin O were purchased from Acros Organics. Anthroquinone-1, 5-disulfonic acid disodium salt hydrate, hexaammineruthenium(III) chloride, potassium indigo trisulfonate, potassium indigo tetra sulfonate, and indigo carmine were purchased from Sigma-Aldrich. Sodium chloride

and 2-[4-(2-hydroxyethyl) piperazin-1-yl] ethane sulfonic acid (HEPES) sodium salt were from Fisher Scientific. The mediator Diquat [6, 7-dihydrodipyrido [1, 2-*a*: 2', 1'-*c*] pyrazinediium dibromide (Table 3.1)] was synthesized using the method described previously by Homer and Tomlinson.² Other reagents were obtained from Thermo-Fisher, Acros Organics or Millipore Sigma, Dot scientific or MP Bio medicals, unless specified otherwise.

3.2.2. General instrumentation

All routine UV/vis spectra were obtained using one of three Cary 50 (Varian) spectrophotometers. Two of these spectrophotometers are housed in nitrogen-filled anaerobic gloveboxes for obtaining spectra of air-sensitive samples. Electrochemistry experiments were carried out in the gloveboxes using BASi Epsilon EC potentiostats.

3.2.3. UV/Visible spectropotentiometric titrations of R103Q ccNiR in the presence of the strong field ligand nitrite

UV/Vis spectropotentiometric experiments were performed using an optically transparent thin-layer electrode (OTTLE) cell of design previously used in our laboratory (Fig. 3.1),³ a BASi Epsilon EC potentiostat to set the potential, and a CARY Bio 50 UV/Vis spectrophotometer to record the spectrum at each applied potential. The apparatus was housed in an anaerobic glove box. An Ag/AgCl electrode (BASi, model RE-5B) was used as a reference. The electrode was checked prior to collection of the spectropotentiometric data sets by using it to obtain cyclic voltammograms of methyl viologen, whose midpoint potential is known to be – 0.449 V vs SHE.⁴ For the experiment, a solution containing R103Q ccNiR (70-90 μ M protomer), the redox mediators listed in Table 3.1, 300 mM NaCl, and 5 mM nitrite,

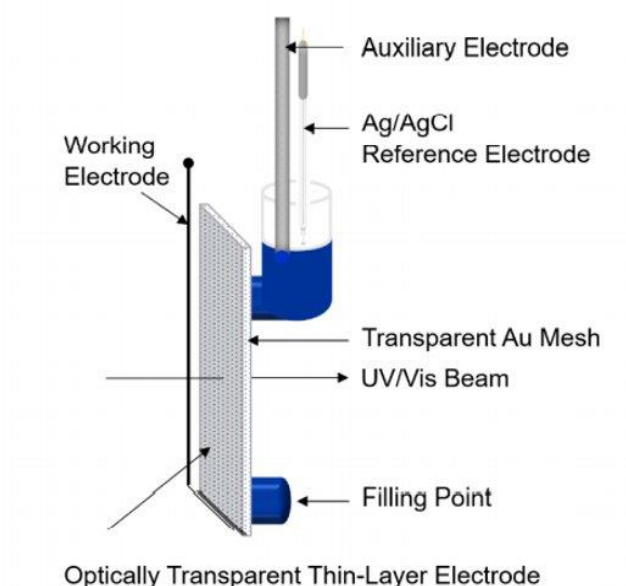


Figure 3.1. The Apparatus used for the Spectro-potentiometric titrations of wild type and R103QccNiR experiments (reproduced with permission from ref. 5). The ash-colored bar is the auxiliary electrode, the white one is the Ag/AgCl reference electrode, and the black bar is the working electrode. The cuvette was filled from the bottom using a syringe, until the upper reservoir contained enough solution for the electrodes to sit in. The transparent gold mesh is sandwiched between the two plates of the demountable cuvette.

in a 50 mM HEPES buffer, pH 7.0, was loaded into the OTTLE cell. UV/visible spectra were collected in the range 300 nm – 800 nm at 10 mV intervals between –100 mV and +200 mV vs SHE. A blank data set was also collected using a solution that contained all the same reagents except for the R103Q ccNiR. The contribution of the mediators and nitrite was then subtracted from each of the spectra obtained in the presence of enzyme. The data sets were analyzed using programs written within the commercially available software package Mathcad 15 (PTC Software). Data were fit with matrix forms of the Nernst equation and Beer's law broadly following methodology used previously by this group,⁴ and described in more detail below. The

R103QccNiR extinction coefficient spectrum obtained with the pyridine hemochrome assay (Chapter 2) was used to obtain the R103Q ccNiR concentrations.

Table 3.1. List of mediators used for the spectropotentiometric titrations of R103Qccnir.

Mediator	ϵ_m (V vs SHE)	Concentration (μM)
<i>N, N,N'N'</i> -tetramethyl- <i>p</i> -phenylenediamine (TMPD)	0.260	25
1,2-naphthoquinone-4-sulfonic acid	0.168	100
Phenazine methosulfate	0.080	25
Hexaammineruthenium (III) chloride	0.050	100
Indigo tetra sulfonate	-0.046	25
Indigo trisulfonate	-0.081	25

3.3. Results

3.3.1. UV/Vis spectropotentiometric experiment with nitrite and mediators only

Several of the mediators in Table 3.1 have appreciable UV/Vis absorbance which can complicate the analysis of the UV/Vis spectral changes associated with ccNiR reduction. For this reason, a spectropotentiometric titration was performed on a solution that contained all the mediators, in addition to nitrite, but no enzyme. This data set was later used to subtract the mediator spectra from those of the enzyme (see below). Figure 3.2a shows the difference spectra obtained by subtracting the spectrum of the fully oxidized mediators from each

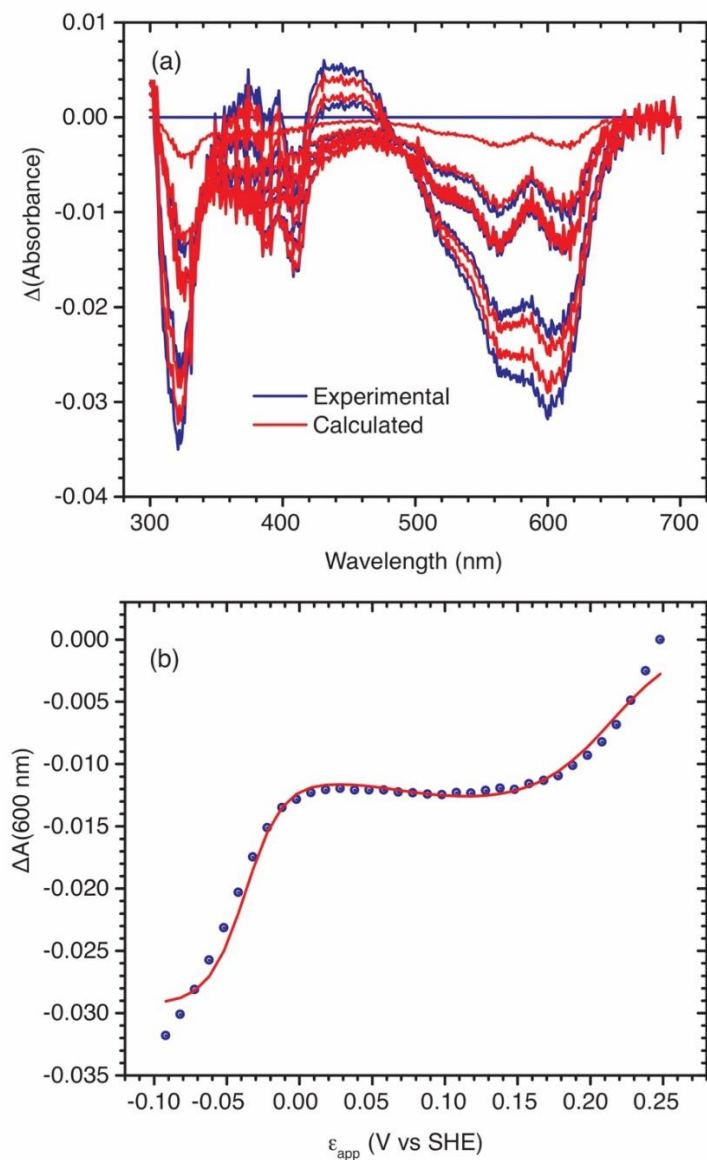
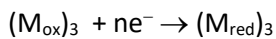
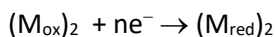
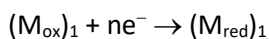


Figure 3.2. (a) UV/Vis spectral changes observed upon exposing a solution containing nitrite and the mediators from Table 3.1, but no enzyme, to progressively lower applied potentials. The blue lines are the experimentally obtained spectra, the red ones were calculated using the equations of Scheme 3.1. For clarity, only select spectra are shown. (b) Blue circles: an absorbance difference vs. applied potential slice taken at 600 nm from the spectra in (a); solid red line: least-squares best fit obtained by fitting the data to the Scheme 3.1 equations.

subsequent spectrum. The Fig. 3.2 data set was analyzed by singular value decomposition (SVD)^{6, 7} and found to be composed of three spectral components, so it was fit with the 3-component model shown in Scheme 3.1, using a fitting routine similar to those previously described by our group.^{4, 8} The model proposes three colored mediators and then defines the fraction of each mediator that is reduced at a given potential as M_i . The values of $M_1 - M_3$, are modeled with



$$M_i \equiv \frac{(M_{red})_i}{(M_{tot})_i} = \frac{\exp\left\{\frac{n_i F}{RT}[(\varepsilon_m)_i - \varepsilon_{app}]\right\}}{1 + \exp\left\{\frac{n_i F}{RT}[(\varepsilon_m)_i - \varepsilon_{app}]\right\}} \quad \text{Eq. 3.1}$$

$$\mathbf{S} = \Delta\mathbf{A} \cdot \left[\mathbf{M}(\mathbf{M}^T \cdot \mathbf{M})^{-1} \right] \quad \text{Eq. 3.2}$$

Scheme 3.1. Model used to fit the Fig. 3.2 data. The model is empirical and only approximates the experimental data (see main text for details).

three Nernstians in exponential form (Eq. 3.1).^{4, 8} In Eq. 3.1, n_i are the number of electrons transferred when reducing M_i , $(\varepsilon_m)_i$ is the midpoint potential of the i^{th} mediator, and ε_{app} is the applied potential. One trial round of data fitting proceeded as follows. A trial set of midpoint potentials $(\varepsilon_m)_1 - (\varepsilon_m)_3$ was manually entered into the fitting program, which then used Eq. 3.1 to generate $M_1 - M_3$ values at each applied potential (the independent variable). The resulting matrix \mathbf{M} was used to generate a right pseudoinverse,⁶ which in Eq. 3.2 then multiplied the matrix of experimental absorbance differences ($\Delta\mathbf{A}$) from the right to generate a matrix of spectral components, \mathbf{S} . Finally, the product of \mathbf{M} and \mathbf{S} was used to generate a theoretical absorbance difference matrix $\Delta\mathbf{A}_{calc}$, which was compared in a least-squares sense with $\Delta\mathbf{A}$. The process was

repeated with varying sets of trial midpoint potentials until the sum of squares obtained from $\Delta A - \Delta A_{\text{calc}}$ was minimized. The red traces in Fig. 3.2a are the spectra calculated using the Scheme 3.1 equations; Figure 3.2b shows an absorbance difference vs applied potential slice taken from the Fig. 3.2a spectra at 600 nm.

Figure 3.3 shows the three spectral components **S** (Eq. 3.2) obtained from the least-squares fit of the Fig. 3.2 data. The first component (blue trace) is associated with a midpoint potential $\varepsilon_{m1} = 0.215\text{V}$ vs SHE and can be assigned to reduction of the TMPD cation radical because of its distinctive maxima at 560 nm and 611 nm. The second component (green trace) with $\varepsilon_{m2} = 0.071\text{V}$ vs SHE is most likely due to reduction of phenazine methosulfate, whereas the third component (red trace) with $\varepsilon_{m3} = -0.037\text{ V}$ vs SHE is due primarily to indigo tetra

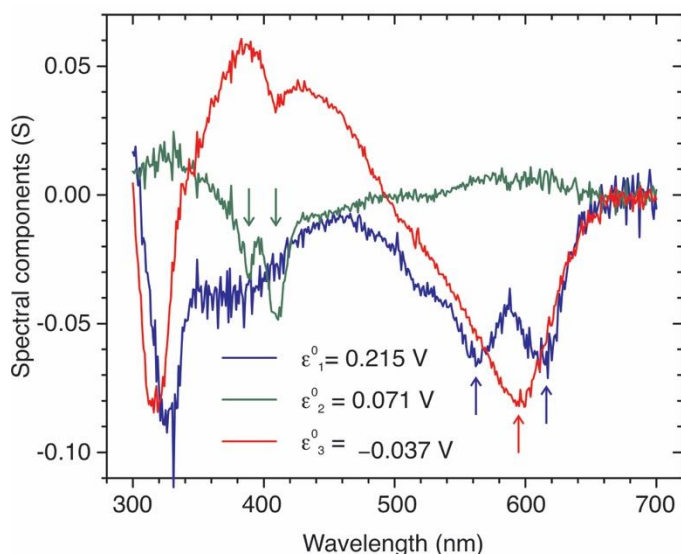


Figure 3.3. Spectral components **S** obtained from fitting the Figure 3.2a data with the Scheme 3.1 equations, along with the midpoint potentials at which each component appeared. The arrows point to distinctive difference maxima that, together with the associated midpoint potentials, could be used to assign each spectral component to a specific mediator or set of mediators (see main text for details).

sulfonate reduction, though the lower potential trisulfonate also contributes to this component. The singular value decomposition analysis showed that the spectra of the two indigos were not resolved into separate components, undoubtedly because the spectropotentiometric titration did not go to low enough potentials to cover the full range within which indigo trisulfonate reduces. As a result of this, the ϵ_{m3} component is an admixture of the indigo tetra- and trisulfonates, and the fit with Eqs. 3.2 and 3.3 is not perfect in the low potential range. However, the Scheme 3.1 fitting routine produced spectral components that were more than adequate for subtracting the small mediator contributions seen in the spectropotentiometric titration of R103QccNiR.

Analysis of an R103QccNiR spectropotentiometric titration is described in the next section. Prior to analyzing the data, a Mathcad program was used to manually subtract fractional multiples of the Fig. 3.3 spectral components from each individual spectrum obtained in the R103QccNiR spectropotentiometric titration. For the most part, this proved straightforward because the ϵ_{m1} and ϵ_{m3} components have distinctive maxima at or above 600 nm, where the ccNiR spectra are comparatively featureless. Furthermore, the applied potential provided guidance as to which component should be subtracted for a given spectrum. Subtraction of the ϵ_{m2} component was more problematic because the absorbance maxima at around 400 nm overlap the heme Soret region. However, the sharp feature at 395 nm provided some guidance as it coincided with a near-isosbestic point for the heme spectra (next section).

3.3.2. UV/Vis spectropotentiometric experiments with *S. oneidensis* R103QccNiR

The blue traces in Fig. 3.4a show the UV/Vis spectral changes, with the mediator contributions subtracted, that were observed after exposing a solution initially containing 79 μM R103QccNiR, 5 mM nitrite, and the mediators listed in Table 3.1, to progressively lower

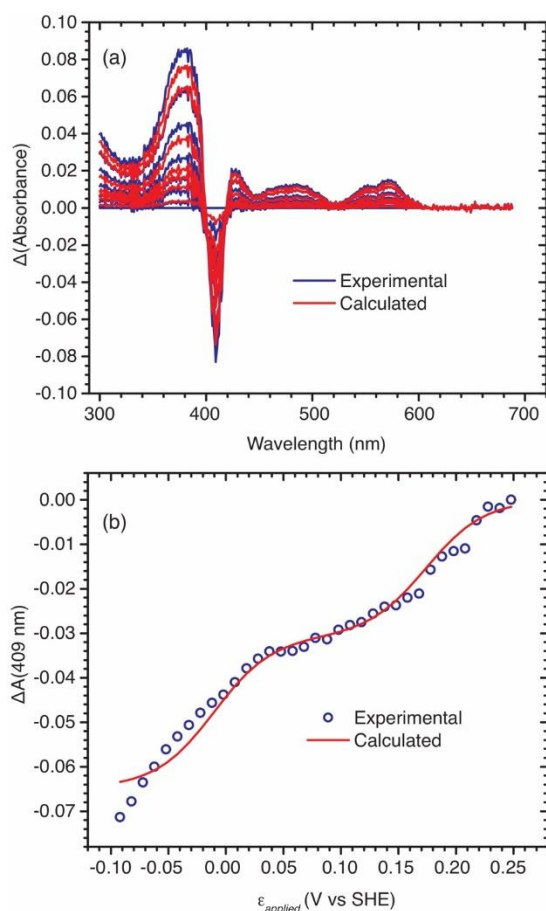
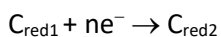
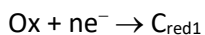


Figure 3.4. (a) UV/Vis spectral changes (with mediator contributions subtracted) observed upon exposing a solution initially containing 79 μM R103QccNiR, 5 mM nitrite, and the mediators listed in Table 3.1, to progressively lower applied potentials. The blue lines are the experimentally obtained spectra, the red ones were calculated using the equations of Scheme 3.2. For clarity, only select spectra are shown. (b) Blue circles: an absorbance difference vs. applied potential slice taken at 409 nm from the spectra in (a); solid red line: least-squares best fit obtained by fitting the data to the Scheme 3.2 equations.

applied potentials. The difference spectra show maximal absorbance increases at 375 nm and decreases at 409 nm. The Fig. 3.4 data set was analyzed by SVD^{6, 7} and found to be composed of two spectral components, so it was fit with the 2-component model shown in Scheme 3.2.^{4, 8} The model proposes a two-step reduction of R103QccNiR, which is simulated with two Nernstian



$$C_{\text{red}(i)} = \frac{C_T \prod_{i=1}^2 E_i}{\text{denom}} \quad \text{Eq. 3.3}$$

$$\text{denom} = 1 + E_1(1 + E_2) \quad \text{Eq. 3.4}$$

$$E_i = \exp \frac{nF}{RT} [\varepsilon_i - \varepsilon_{\text{app}}] \quad \text{Eq. 3.5}$$

$$\Delta \varepsilon = \Delta \mathbf{A} \cdot \left[\mathbf{C}_{\text{red}} \left(\mathbf{C}_{\text{red}}^T \cdot \mathbf{C}_{\text{red}} \right)^{-1} \right] \frac{1}{l} \quad \text{Eq. 3.6}$$

Scheme 3.2. Model used to fit the Fig. 3.4 data (see main text for details).

equations as shown in Eqs. 3.3 – 3.5 of Scheme 3.2. In Eqs. 3.3 – 3.5, n is the number of electrons transferred in each ccNiR reduction step (here assumed to be the same in both steps), ε_i is the midpoint potential of the i^{th} reduction step, C_T is the total concentration of R103QccNiR, and ε_{app} is the applied potential (the independent variable). One trial round of data fitting proceeded as follows. A trial set of midpoint potentials $\varepsilon_1, \varepsilon_2$, was manually entered into the fitting program, which then used Eqs. 3.3 – 3.5 to generate $C_{\text{red}1}$ and $C_{\text{red}2}$ values at each applied potential. The resulting matrix \mathbf{C}_{red} was used in Eq. 3.6 to generate a right pseudoinverse,⁶ which then multiplied

the matrix of experimental absorbance differences ($\Delta\mathbf{A}$) from the right to generate a matrix of extinction coefficient difference spectra $\Delta\epsilon$. Finally, the product of \mathbf{C}_{red} and $\Delta\epsilon$ was used to generate a theoretical absorbance difference matrix $\Delta\mathbf{A}_{\text{calc}}$, which was compared in a least-squares sense with $\Delta\mathbf{A}$. The process was repeated with varying sets of trial midpoint potentials until the sum of squares obtained from $\Delta\mathbf{A} - \Delta\mathbf{A}_{\text{calc}}$ was minimized. The red traces in Fig. 3.4a are the spectra calculated using the Scheme 3.2 equations; Figure 3.4b shows an absorbance difference vs applied potential slice taken from the Fig. 3.4a spectra at 409 nm. The best fits were obtained with n , the number of electrons transferred in each step, set to 1, and the midpoint potentials for the two reduction steps set at $\epsilon_1 = 0.174$ V and $\epsilon_2 = -0.010$ V vs. SHE. Figure 3.5 shows the spectral components (extinction coefficient difference spectra), $\Delta\epsilon_1$ and $\Delta\epsilon_2$, obtained with the fit.

3.4. Discussion

The R103QccNiR variant behaved very differently from the wtccNiR when electrochemically reduced in the presence of nitrite. For comparison, Figure 3.6 shows the results of a wtccNiR spectropotentiometric titration obtained earlier by M. Ali from our research group.¹ For the wild type, heme reduction in the presence of excess nitrite proceeded in a single concerted 2-electron step with a midpoint potential of 0.250 V vs SHE (Fig. 3.6), and the difference spectra showed maximal absorbance increases at 424 nm and decreases at 402 nm. Such changes are fairly typical of low-spin *c*-heme reduction,^{9, 10} though the Fig. 3.6a spectra lack the bands normally seen at 525 nm and 550 nm when low-spin *c*-hemes reduce.

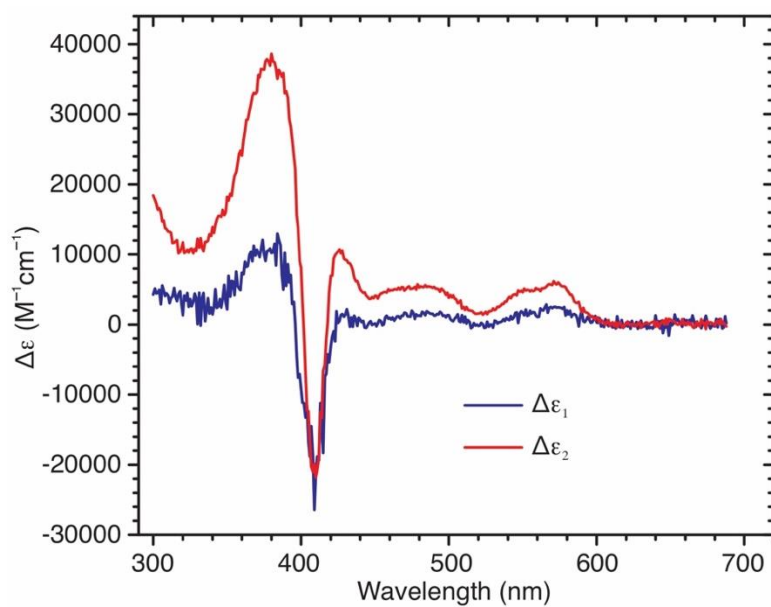


Figure 3.5. Spectral components $\Delta\epsilon$, obtained from fitting the Figure 3.4a data with the Scheme 3.2 equations. $\Delta\epsilon_1$ appeared in a step governed by a midpoint potential $\epsilon_1 = 0.174$ V, and $\Delta\epsilon_2$ appeared in a step governed by a midpoint potential $\epsilon_2 = -0.010$ V.

By contrast, the difference spectra obtained upon spectropotentiometric titration of R103QccNiR (Fig. 2.4a) show maximal absorbance increases at 375 nm and decreases at 409 nm, which are not at all typical of *c*-heme reduction. Furthermore, heme reduction for R103QccNiR was modeled with two 1-electron reduction steps instead of one 2-electron step (Fig. 3.4, Scheme 3.2), and the highest midpoint potential ($\epsilon_1 = 0.174$ V) was observed 0.072 V below the midpoint potential of the wild type heme reduction event. The major reduction event, the one associated with the larger spectral change (Fig. 3.5), had a midpoint potential of $\epsilon_2 = -0.010$ V, 0.256 V below the wild type midpoint potential. Scheme 3.3 outlines all the possible intermediates that might be expected when the ccNiR active site is exposed to reducing potentials in the presence of nitrite. The nitrite-loaded active site, $\text{Fe}_{\text{H1}}^{\text{III}}(\text{NO}_2^-)$,

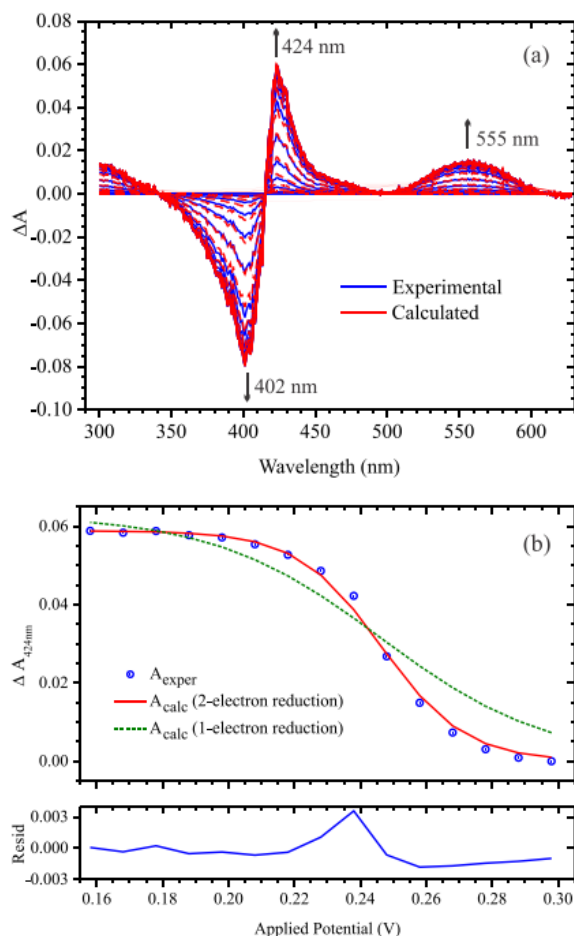
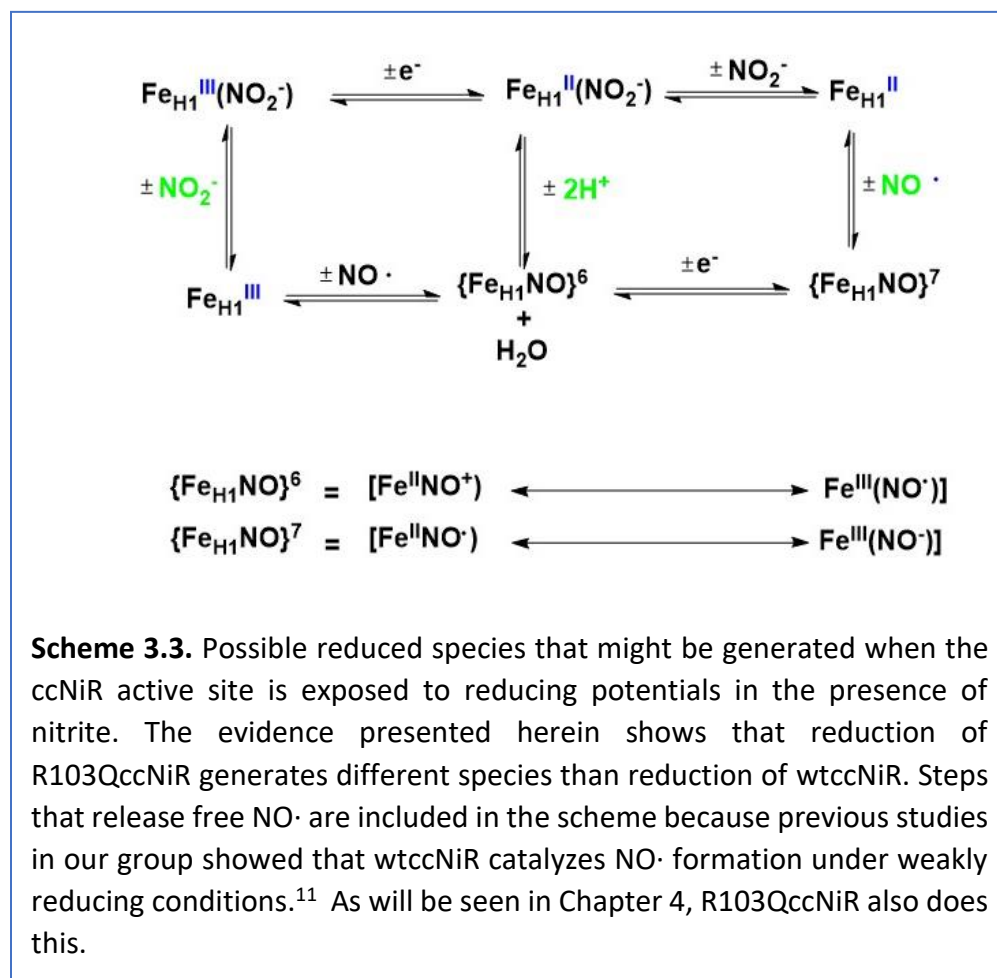


Figure 3.6. (a) UV/Vis spectral changes obtained upon exposing a solution initially containing 76 μM of fully oxidized wild type ccNiR, 100 μM 1, 2-naphthoquinone-4-sulfonic acid and 5 mM nitrite to progressively lower potentials.¹ Solid blue lines show the experimentally obtained data, whereas the dashed red lines were calculated from least-squares fitting with a Nernstian 2-electron reduction and one spectral component. The fit yielded a midpoint potential of $\varepsilon_m = 0.246$ V. (b) Blue circles: an absorbance difference vs. applied potential slice taken at 424 nm from the spectra of part (a); solid red line: least-squares best fit obtained from global analysis of the data with n fixed at 2 electrons transferred in the Nernstian equation; dotted green line: same as the red line, but with n fixed at 1 electron transferred in the Nernstian equation.¹



could first be reduced by one electron to $\text{Fe}_{\text{H1}}^{\text{II}}(\text{NO}_2^-)$, at which point one of the nitrite oxygen's could be protonated and leave as water to give the species referred to as $\{\text{Fe}_{\text{H1}}\text{NO}\}^6$ in the "Enemark-Feltham" notation (Scheme 3.3).¹² A second 1-electron reduction would then give the 2-electron reduced species referred to as $\{\text{Fe}_{\text{H1}}\text{NO}\}^7$ in the Enemark-Feltham notation (Scheme 3.3).¹²

The spectropotentiometric results shown in Fig. 3.6 for wtccNiR show no sign of 1-electron reduced heme 1 species,¹ which suggests that the midpoint potential for the second 1-electron reduced step is much higher than that of the first, so that once the first electron is added,

the second immediately follows and no 1-electron reduced species accumulates.¹ More recently, a transient 1-electron reduced species was detected by stopped-flow UV/Vis spectroscopy when nitrite-loaded wtccNiR was reduced by TMPD (Section 1.3.3).¹¹ The 1-electron reduced intermediate appears to be $\text{Fe}_{\text{H1}}^{\text{II}}(\text{NO}_2^-)$, and there is no evidence that the anhydrous 1-electron reduced species, $\{\text{Fe}_{\text{H1}}\text{NO}\}$,⁶ ever accumulates (Section 1.3.3).¹¹ In the stopped-flow experiments, the 1-electron reduced species builds up over about 1s and is then converted to 2-electron reduced $\{\text{Fe}_{\text{H1}}\text{NO}\}$ ⁷ moiety in a little less than a minute.

In contrast to what is seen with wtccNiR, the Fig. 3.4 data for R103QccNiR appear to suggest that the variant reduces by successive 1-electron steps. However, there are some difficulties with this interpretation. First, the two spectral components for the putative successive 1-electron transfers are nothing like those observed by stopped flow and attributed to $\text{Fe}_{\text{H1}}^{\text{II}}(\text{NO}_2^-)$ and $\{\text{Fe}_{\text{H1}}\text{NO}\}$ ⁷ moieties for the wtccNiR,¹¹ which begs the question of why 1- and 2-electron reduced R103QccNiR moieties should look so different. Second, the two spectral components in Fig. 3.5 have very similar shapes, yet the second component has substantially higher amplitude than the first. It is difficult to rationalize why addition of a second electron to the active site would result such a higher amplitude change. Finally, it is clear from even cursory inspection of Fig. 3.4b that the Scheme 3.2 model fits the data poorly at lower potentials. Indeed, the absorbance at 409 nm clearly continues to decrease below $\mathcal{E}_{\text{app}} = -0.08$ V (the lowest potential used in the experiment), whereas the model predicts that the absorbance should be levelling off at that point. Unfortunately, this last observation calls into question the legitimacy of using UV/Vis spectropotentiometry to study reduction of R103QccNiR in the presence of nitrite. The use of UV/Vis spectropotentiometry depends on being able to collect each individual

spectrum while the redox-active species are at equilibrium, which shouldn't be possible in an enzyme that catalyzes reduction of nitrite to ammonia. It is possible to do UV/Vis spectropotentiometry with nitrite-loaded wtccNiR because the heme 1 midpoint potential of 0.24 V vs SHE is almost 0.3 V above the potential at which significant nitrite turnover can take place,^{1, 13, 15} and also at about 0.3 V above the point at which other ccNiR hemes reduce.⁸ However, the low potentials being probed in the R103QccNiR experiments begin to stray into the range where nitrite turnover becomes important, meaning that equilibrium may no longer be attainable.^{1, 14, 15} Furthermore, at potentials of -0.08 V vs SHE, ccNiR hemes other than the heme 1 active site should start to reduce,⁸ meaning that it is not valid to fit the data with a model that considers only the active site heme.

Interestingly, UV/Vis spectropotentiometric titrations of the nitrite-loaded variants H257QccNiR,⁵ and Y206FccNiR (Steven Reinhardt, personal communication), generated spectral changes very similar to those seen with nitrite-loaded R103QccNiR. Though on the one hand these results call into question the validity of using UV/Vis spectropotentiometry for quantitative investigation of any of the three variants, the results show qualitatively that the three variants generate one or more common intermediates upon reduction that are distinct from the 2-electron reduced intermediate seen in the wild type. Furthermore, the results show that, in the presence of nitrite, some spectral changes occur upon applying potentials as high as 0.170 V vs SHE (Figs. 3.4, 3.5). While this potential may not be as high as the heme 1 midpoint potential of nitrite-loaded wtccNiR (0.24 V vs SHE), it is substantially higher than the potential at which the *S. oneidensis* wtccNiR active site reduces in the absence of nitrite, even when the strong-field ligand cyanide is supplied (0.02 V vs SHE).⁸ The steady-state and stopped-flow kinetics experiments to

be presented in Chapter 5 will shed further light on the nature of the species generated upon reduction of nitrite-loaded R103QccniR. However, definitive characterization of the reduced species will require EPR, and perhaps Mossbauer or vibrational spectroscopic studies; some of these are planned for the near future.

3.5. References

1. Ali, M.; Stein, N.; Mao, Y.; Shahid, S.; Schmidt, M.; Bennett, B.; Pacheco, A. A., Trapping of a putative intermediate in the cytochrome *c* nitrite reductase (ccNiR)-catalyzed reduction of nitrite: implications for the ccNiR reaction mechanism *J. Am. Chem. Soc.* **2019**, *141*, 13358-13371.
2. Homer, R. F.; Tomlinson, T. E., The stereochemistry of the bridged quaternary salts of 2,2'-bipyridyl. *J. Chem. Soc.* **1960**, 2498-2503.
3. Heineman, W. R.; Norris, B. J.; Goelz, J. F., Measurement of enzyme E^0 values by optically transparent thin layer electrochemical cells. *Anal. Chem.* **1975**, *47*, 79-84.
4. Youngblut, M.; Judd, E. T.; Srajer, V.; Sayyed, B.; Goelzer, T.; Elliott, S. J.; Schmidt, M.; Pacheco, A. A., Laue crystal structure of *Shewanella oneidensis* cytochrome *c* nitrite reductase from a high-yield expression system. *J. Biol. Inorg. Chem.* **2012**, *17*, 647-662.
5. Shahid, S. A mechanistic investigation of cytochrome *c* nitrite reductase catalyzed reduction of nitrite to ammonia: the search for catalytic intermediates. University of Wisconsin-Milwaukee, Milwaukee, WI, 2020.
6. Press, W. H.; Teukolsky, S. A.; Vetterling, W. T.; Flannery, B. P., Numerical Recipes the art of scientific computing. 3rd ed.; Cambridge University Press: New York, NY, 2007; pp 773-839.
7. Henry, E. R.; Hofrichter, J., Singular Value Decomposition: Application to Analysis of Experimental Data. In *Meth. Enzymol.*, Brand, L.; Johnson, M. L., Eds. Academic Press: San Diego, 1992; Vol. 210, pp 129-192.
8. Stein, N.; Love, D.; Judd, E. T.; Elliott, S. J.; Bennett, B.; Pacheco, A. A., Correlations between the electronic properties of *Shewanella oneidensis* cytochrome *c* nitrite reductase (ccNiR) and its structure: effects of heme oxidation state and active site ligation. *Biochemistry* **2015**, *54*, 3749-3758.
9. Arciero, D. M.; Balny, C.; Hooper, A. B., Spectroscopic and Rapid Kinetic-Studies of Reduction of Cytochrome-C554 by Hydroxylamine Oxidoreductase from *Nitrosomonas-Europaea*. *Biochemistry* **1991**, *30* (48), 11466-11472.
10. Marritt, S. J.; Kemp, G. L.; Xiaoe, L.; Durrant, J. R.; Cheesman, M. R.; Butt, J. N., Spectroelectrochemical characterization of a pentaheme cytochrome in solution and as electrocatalytically active films on nanocrystalline metal-oxide electrodes. *J. Am. Chem. Soc.* **2008**, *130*, 8588-8589.
11. Shahid, S.; Ali, M.; Legaspi-Humiston, D.; Wilcoxon, J.; Pacheco, A. A., A kinetic investigation of the early steps in cytochrome *c* nitrite reductase (ccNiR)-catalyzed reduction of nitrite. *Biochemistry* **2021**, *60*, 2098-2115.

12. Enemark, J. H.; Feltham, R. D., Principles of Structure, Bonding and Reactivity for Metal Nitrosyl Complexes. *Coord. Chem. Rev.* **1974**, *13*, 339-406.
13. Judd, E. T.; Youngblut, M.; Pacheco, A. A.; Elliott, S. J., Direct Electrochemistry of *Shewanella oneidensis* Cytochrome c Nitrite Reductase: Evidence of Interactions across the Dimeric Interface. *Biochemistry* **2012**, *51* (51), 10175-10185.
14. Rahaman, M.; Ali, M. S.; Jahan, K.; Hinz, D.; Belayet, Rahman, A. F. M. T.; Hossain, M. M., Chemistry of 3-hydroxy-2-aryl acrylate: syntheses, mechanisms, and applications. *Org. Chem. Front.*, **2021**, *8*, 169-191.
15. Judd, E. T.; Stein, N.; Pacheco, A. A.; Elliott, S. J., Hydrogen bonding networks tune proton-coupled redox steps during the enzymatic six-electron conversion of nitrite to ammonia. *Biochemistry* **2014**, *53*, 5638-5646.

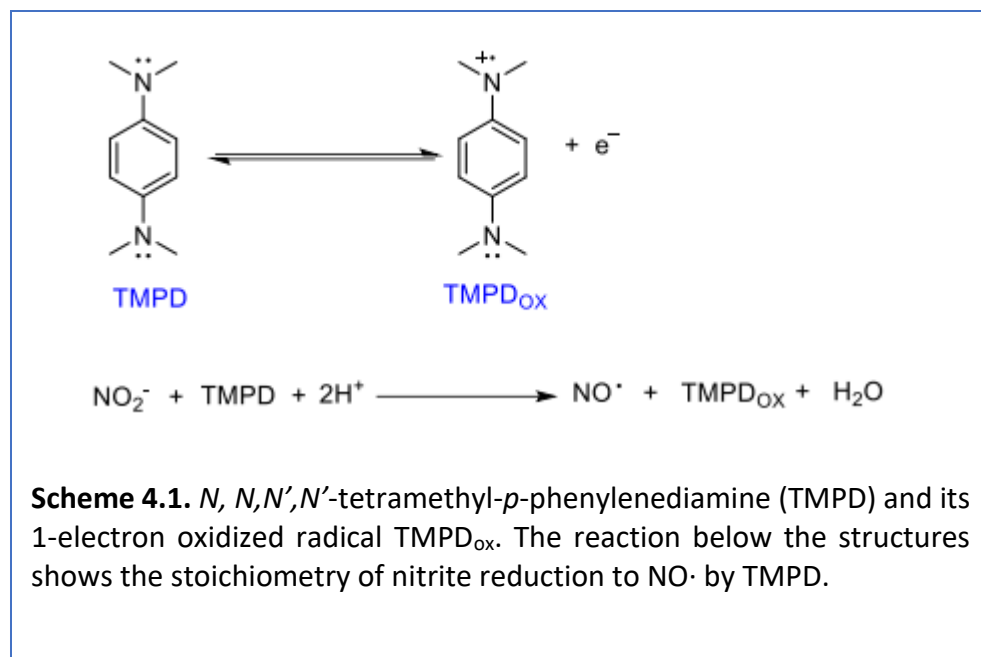
Chapter 4

Reactivity of Nitrite-Loaded R103QccNiR with *N,N,N',N'*-tetramethyl-*p*-phenylenediamine (TMPD)

4.1. Overview

In the standard ccNiR assay, with the strong reductant MV_{red} as the electron source (Chapter 2), ammonium (NH₄⁺) is the sole product of nitrite reduction. However, intermediates accumulate when weaker reductants are employed, facilitating study of the ccNiR mechanism.¹

² This chapter presents a kinetic study in which the weak reductant *N,N,N',N'*-tetramethyl-*p*-phenylenediamine (TMPD, $\varepsilon_m = +0.260$ V vs SHE) was used to reduce mixtures of nitrite and *S. oneidensis* R103QccNiR under various conditions. An advantage of using TMPD as reductant is that the product of TMPD 1-electron oxidation, (TMPD_{ox}, Scheme 4.1) has an intense blue color that is readily detectable by UV/Vis spectroscopy. When TMPD is used to reduce nitrite in the presence of wtccNiR, nitric oxide is catalytically produced, albeit at a very slow rate.⁴ To test for NO· generation when TMPD and nitrite were mixed with R103QccNiR, catalase (Cat) was added to the reaction mixture in some of the experiments. Catalase binds NO· strongly, producing a distinctive color change that can be used to quantify the amount of NO· generated.^{4, 5}



4.2. Materials and methods

4.2.1. General Materials

The reagent TMPD was from Fisher Scientific, nitrite was from ACROS Organics, HEPES free acid from Millipore Sigma. All were used without additional purification.

4.2.2. General instrumentation

Time-resolved UV/Vis spectroscopy experiments were performed using a CARY Bio 50 UV/Vis spectrophotometer housed inside a nitrogen-filled glovebox (Innovative Technologies) to provide an anaerobic environment. The oxygen level was strictly monitored and maintained at less than 2 ppm; the glovebox catalysts were regenerated with 7% Hydrogen (Airgas) once a month or whenever the oxygen level rose above 2 ppm.

4.2.3. Reduction of nitrite-loaded *S. oneidensis* R103QccNiR by TMPD

TMPD and nitrite stock solutions were prepared in 50 mM HEPES pH = 7.0 buffer; TMPD stock solutions are stable for at least one week, and nitrite stock solutions are stable indefinitely, in the glovebox. Reduced TMPD is colorless but 1- electron oxidized TMPD has an intense blue color that is readily detectable by UV-Vis spectroscopy, or even by visual inspection. Steady-state experiments were performed to assess the kinetic dependence of the ccNiR-catalyzed reduction of nitrite by TMPD on TMPD, nitrite and *S. Oneidensis* R103Q ccNiR concentrations. In a typical steady-state experiment, 0-4 mM TMPD, 0-10mM NO_2^- , and 0-2 μM R103Q ccNiR, were mixed in a 1-mL semimicro cuvette (Starna), with 50 mM HEPES, pH = 7 buffering the solution. All the reagents were very quickly mixed using a cuvette mixer (Fireflysci P68 mixer for semi-micro cuvettes), and data collection was immediately initiated. Spectra were collected every 15 s for 1 h in the range 300 nm - 800 nm (240 scans total). Data were analyzed by using programs written for Mathcad 15.0 (PTC Software) and Origin 9.0 (Microcal Software).^{6, 7}

4.2.4. Catalase purification and handling

Catalase from bovine liver was purified by using a previously described method,⁵ and then concentrated to 74 μM before degassing. As catalase denatures upon freezing, it could not be transferred frozen through the glovebox antechamber, which is the method typically used to transfer ccNiR and other proteins through the evacuated antechamber. Instead, an aliquot of 1.5ml purified and concentrated catalase was put in an open glass vial, which in turn was placed in a wide mouth glass test tube. This test tube was sealed with a rubber septum that was additionally wrapped with thermal tape. Two needles were inserted through the rubber septum;

one needle was connected to an argon line that supplied water-saturated argon, and the second to a water bubbler that opened to the atmosphere. To completely deoxygenate the catalase, wet argon was run very gently over the solution for 2h. Finally, the degassed catalase was brought into the glovebox and kept in a 4 °C fridge until needed for the experiment (Caution: the septum on the test tube must be firmly secured so that it does not pop out when placed in the glovebox antechamber).⁸

4.3. Results

4.3.1. Steady-state analysis of R103Q ccNiR-catalyzed reduction of nitrite by TMPD

Figure 4.1a shows the UV/Vis spectral changes observed after mixing 1.03 μM R103QccNiR with 8mM nitrite and 1.2mM TMPD, in a pH 7 HEPES buffer. SVD analysis showed that only two spectral components were needed to faithfully reconstruct a noise-reduced absorbance matrix. The SVD-treated data were then fit to Eq 4.1 using a global fitting

$$f_1(t) = \text{frac} \times [1 - \exp(-k_1 t)] + (1 - \text{frac}) \times [1 - \exp(-k_2 t)] \quad \text{Eq. 4.1a}$$

$$A_{\lambda,t} = L_{0(\lambda)} + L_{1(\lambda)} \times f_1(t) \quad \text{Eq. 4.1b}$$

routine (red traces, Fig. 4.1a).^{6, 7} In Eq 4.1, $A_{\lambda,t}$ is the absorbance obtained at wavelength λ and time t , and the spectral component L_0 is present immediately after adding nitrite (taken as $t = 0$). The second component in Eq. 4.1, L_1 , grows in as a function of two exponentials with time (Eq. 4.1b). The parameter *frac* in Eq. 4.1 determines the relative amplitudes of the first and second exponential components, while k_1 and k_2 are the rate constants. Figure 4.1b shows an

absorbance vs. time slice from the Fig. 4.1a data set, obtained at the 611 nm local maximum. The blue trace is experimentally obtained, the red one is the least-squares best fit to Eq. 4.1.

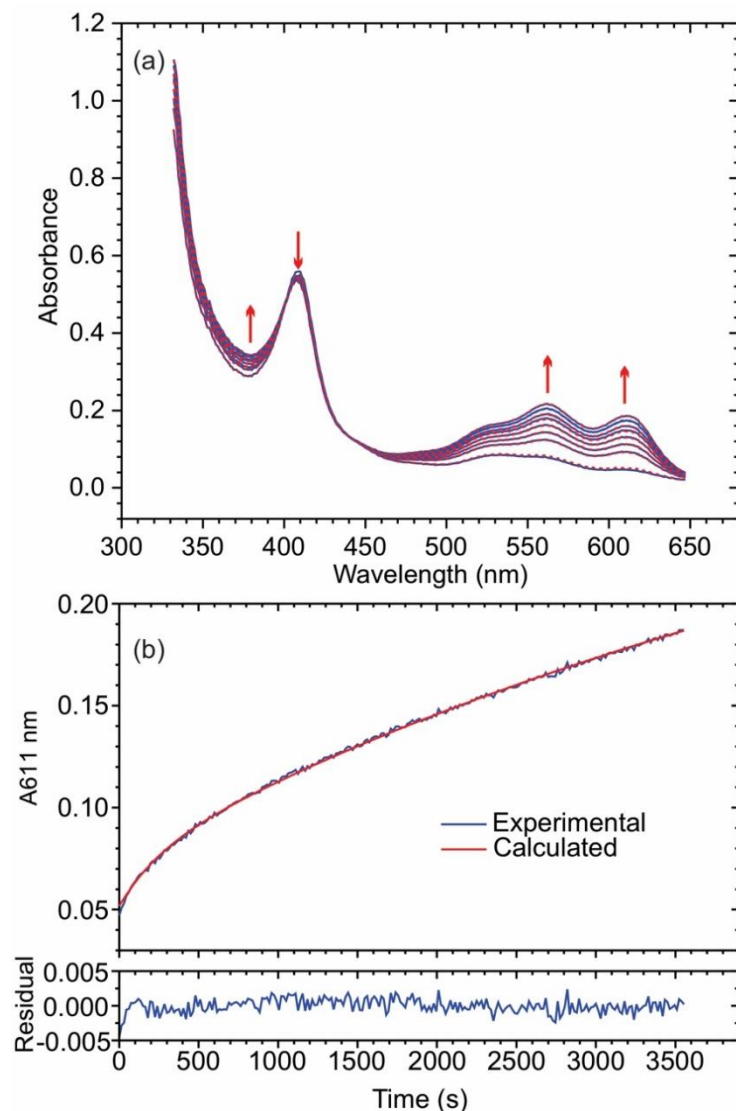


Figure 4.1. (a) Blue traces: UV/Vis spectral changes observed after mixing 8 mM Nitrite, 1.2 mM TMPD, and 1.03 μ M R103QccNiR in a pH 7 HEPES buffer. Red traces: least-squares best fit with Eq. 4.1. The reaction mixture was monitored at 15s intervals, but for clarity, the selected traces are at 600 s intervals. (b) Blue trace: absorbance vs. time slice taken at the 611 nm maximum of the data set above. Red trace: least-squares best fit with Eq. 4.1.

Figure 4.2 shows the spectral components obtained from the fitting process. The component Λ_0 (blue trace, Fig. 4.2a) was in turn fit with the independently obtained extinction coefficient spectra of fully oxidized R103QccNiR (R103Q_{ox}), nitrite, TMPD, and TMPD_{ox} (red dashed trace, Fig. 4.2a). The fit shows that, at time zero, the R103QccNiR was fully oxidized. By contrast, when wtccNiR is exposed to comparable conditions, the nitrite-loaded heme 1 active is reduced within the mixing time, so the Λ_0 spectrum obtained by an analogous fitting routine shows the reduced heme.⁴ The Fig. 4.2a fit allowed the total R103QccNiR concentration to be accurately determined for every experiment. It also allowed the initial concentration of TMPD_{ox} to be determined. Ideally, no TMPD_{ox} was expected at time zero, and in most experiments using fresh TMPD, its concentration was less than 0.5 μ M. Initial TMPD_{ox} concentrations greater than ~ 2 μ M were seen when the oxygen level in the glovebox crept up above 2 ppm, and these were taken as a signal to regenerate the glovebox.

The blue trace in Fig. 4.2b shows the Λ_1 spectral component obtained by fitting the Fig. 4.1a data with Eq. 4.1. The arrows seen in the range from 350 nm – 430 nm are reminiscent of the changes observed during spectropotentiometric reduction of nitrite-loaded R103QccNiR (Chapter 3) and are thus attributed to heme reduction. As the extinction coefficient difference spectrum associated with reduction of nitrite loaded R103QccNiR is unavailable at present, this part of the spectrum could not yet be quantitatively analyzed. However, the part of the spectral component between 500 nm and 650 nm was well fit using only the independently known extinction coefficient spectrum of TMPD_{ox}, (dotted red trace, Fig. 4.2b) showing that TMPD was being oxidized during the hour that the reaction was monitored. No effort was made to interpret the empirical 2-exponential dependence of Λ_1 growth with time (Eq. 4.1b).

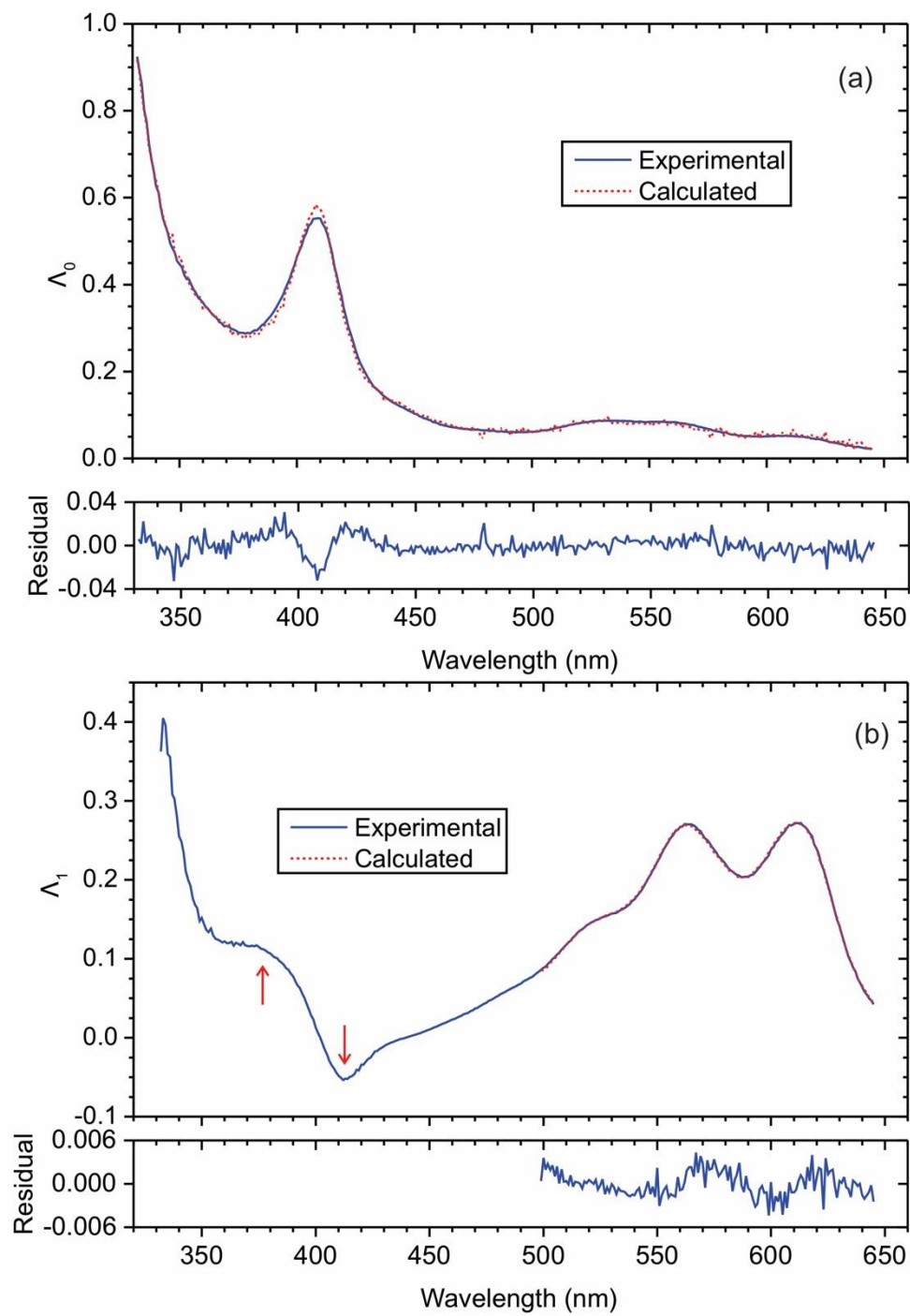


Figure 4.2. Spectral components (a) Λ_0 and (b) Λ_1 generated by fitting the SVD-processed Fig. 4.1 data with Eq. 4.1. The overlaid dashed red traces are the least-squares best fits obtained using known extinction coefficient spectra, as described in the main text.

Instead, the derivative of Eq. 4.1b was used to accurately obtain the initial rate (V_0) of TMPD oxidation (Eq. 4.2). In Eq. 4.2, $[TMPD_f]$ is the limiting concentration of $TMPD_{ox}$ calculated from the Λ_1 fit.

$$V_0 = [TMPD_f] \times [k_1 \times frac + k_2 \times (1 - frac)] \quad \text{Eq. 4.2}$$

To test the dependence of V_0 on the initial R103QccNiR concentration, a series of experiments analogous to the one shown in Fig. 4.1 was carried out with the initial nitrite and TMPD concentrations fixed at 8 mM and 1.2 mM, respectively, but with varying initial R103QccNiR concentration. Figure 4.3 shows that V_0 varies linearly with $[R103QccNiR]_0$, with a slope of $(7 \pm 2) \times 10^{-3} \text{ s}^{-1}$ and an intercept of $2 \pm 2 \text{ nMs}^{-1}$. This proves that R103QccNiR is catalyzing the oxidation of TMPD to $TMPD_{ox}$. The scatter in this set of experiments was rather high because the experiments were carried out during an extended time in which, for never completely understood reasons, the oxygen levels in the glovebox were consistently higher than usual. The scatter makes it difficult to tell if there is any background TMPD oxidation taking place in the absence of enzyme, other than that attributable to background oxygen. Fortunately, experiments described in the next section provided a more precise measurement of the V_0 dependence on $[R103QccNiR]$ (see Section 4.3.2).

Given the linear dependence of V_0 on $[R103QccNiR]_0$, for convenience, we now define an apparent first-order rate constant as $k_{app} \equiv V_0/[R103QccNiR]_0$. Figures 4.4 and 4.5 then show the dependence of k_{app} on $[TMPD]_0$ and $[NO_2^-]_0$, respectively. Figure 4.4 shows that k_{app} is independent of TMPD concentration in the range from 100 μM – 4 mM, which puts an upper

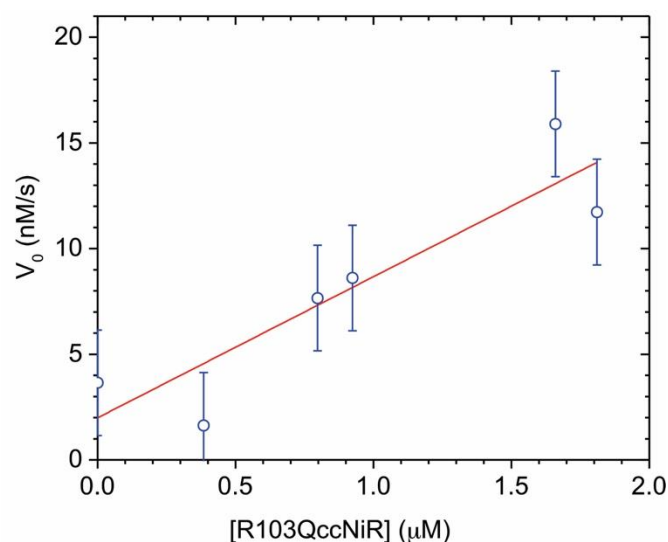


Figure 4.3. Blue circles: dependence of the initial TMPD oxidation rate (V_0 , nM/s) on total R103QccNiR concentration, with $[\text{NO}_2^-]_0$ and $[\text{TMPD}]_0$ held constant at 8 mM and 1.2 mM, respectively. All experiments were performed in 50 mM HEPES buffer (pH 7.0). Red line: least-squares fit of the data; slope = $(7 \pm 2) \times 10^{-3} \text{ s}^{-1}$, intercept = $2 \pm 2 \text{ nMs}^{-1}$.

limit on the K_m value for any putative hyperbolic $[\text{TMPD}]$ dependence at less than 50 μM . The average k_{app} value obtained by averaging the data over the whole $[\text{TMPD}]_0$ range was $0.011 \pm 0.003 \text{ s}^{-1}$. This value agrees with that obtained in the $[\text{R103QccNiR}]_0$ – dependence study shown in Fig. 4.3, though the scatter in these experiments was once again rather high. The k_{app} vs $[\text{NO}_2^-]_0$ plot (Fig. 4.5) likewise showed very little dependence of k_{app} on $[\text{NO}_2^-]_0$, staying roughly constant at $0.011 \pm 0.006 \text{ s}^{-1}$ down to about 200 μM $[\text{NO}_2^-]_0$. Below 200 μM $[\text{NO}_2^-]_0$, V_0 may be starting to decrease, but the scatter at low $[\text{NO}_2^-]_0$ makes it impossible to characterize such a decrease quantitatively. The conclusion that is drawn from the k_{app} vs $[\text{TMPD}]_0$, and k_{app} vs $[\text{NO}_2^-]_0$ experiments is that k_{app} is insensitive to changes in concentrations of these species, at least above 200 μM . This in turn suggests that k_{app} is k_{cat} , the turnover rate for R103Q-catalyzed oxidation of TMPD in the presence of nitrite.

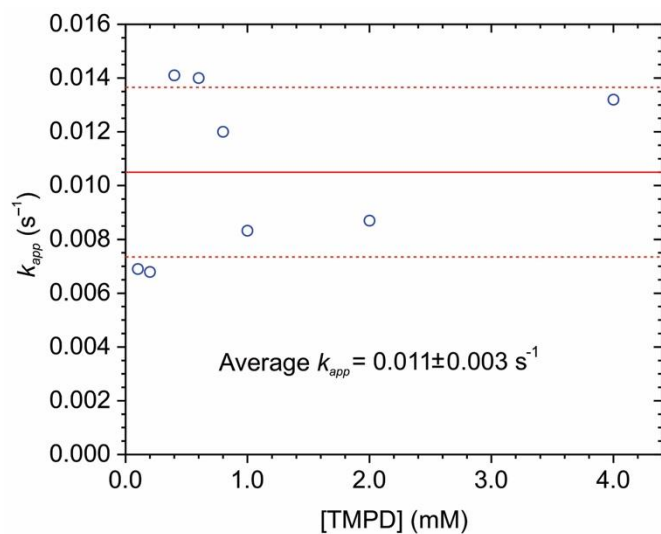


Figure 4.4. Blue circles: dependence of k_{app} ($V_0/[R103QccNiR]$, s^{-1}) on total TMPD concentration, with $[NO_2^-]_0$ held constant at 8 mM. All experiments were performed in 50 mM HEPES buffer (pH 7.0). Solid red line: average k_{app} value; dashed lines: standard deviation.

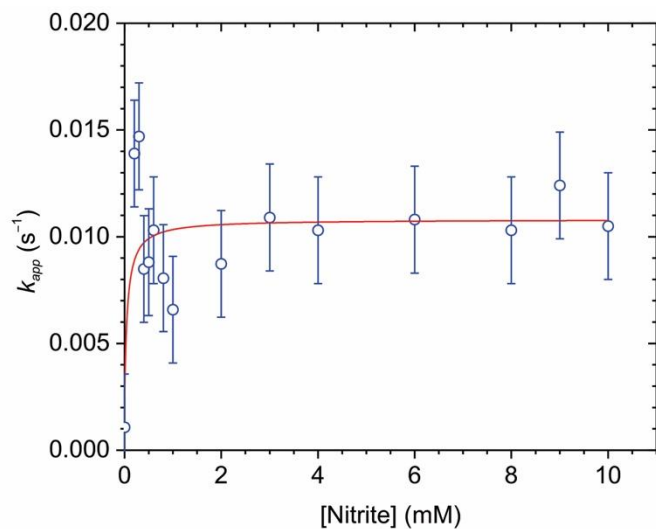
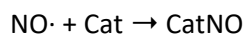
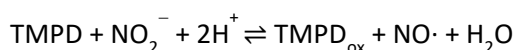


Figure 4.5. Blue circles: dependence of k_{app} ($V_0/[R103QccNiR]$, s^{-1}) on total nitrite concentration, with $[TMPD]_0$ held constant at 1 mM. All experiments were performed in 50 mM HEPES buffer (pH 7.0). Solid red line: least-squares fit to a rectangular hyperbola in which a K_m value was fixed at an arbitrary value below 100 mM (this was used for illustrative purposes only, as any hyperbolic behavior is completely masked by the data scatter at low nitrite concentrations). The data stayed roughly constant at $0.011 \pm 0.006 s^{-1}$ down to about 200 mM $[NO_2^-]_0$.

4.3.2. NO· trapping experiments

The amount of TMPD oxidized in the experiments described in the previous section was higher than that needed to reduce R103QccNiR, which suggested that the variant was catalyzing reduction nitrite to nitric oxide by TMPD (step 1, Scheme 4.1), as had been previously observed for wtccNiR.⁴ To test for this possibility, the experiment of Fig. 4.3 was repeated in the presence of catalase, which rapidly and strongly binds NO· in a process accompanied by a distinct color change (step 2, Scheme 4.2).⁵ Thus, the experiments with catalase allowed production of the colored TMPD_{ox} and CatNO to be simultaneously quantified.



Scheme 4.2. Trapping of NO· by catalase. Catalase (Cat) and the nitrosylated product (CatNO) have very different colors.

Figure 4.6 summarizes the results of a series of experiments in which solutions initially containing 2 mM nitrite, 1mM TMPD, 4 μM catalase, and varying concentrations of R103QccNiR, in 50 mM HEPES pH 7 buffer, were allowed to react for 1h as in the Fig. 4.1 experiment. The blue circles and red squares in Fig. 4.6 show how the initial rates of CatNO and TMPD_{ox} formation, respectively, vary with R103QccNiR concentrations. Both the $V_0(\text{CatNO})$ and $V_0(\text{TMPD}_{\text{ox}})$ vs [R103QccNiR] data sets were well fit with nearly overlapping straight lines, which is consistent with the conjecture that virtually all TMPD oxidation was associated with reduction of nitrite to NO·, as shown in step 1 of Scheme 4.2. The slope of the $V_0(\text{CatNO})$ vs [R103QccNiR] line (blue) is

$(2.54 \pm 0.07) \times 10^{-3} \text{ s}^{-1}$, while that of the $V_0(\text{TMPD}_{\text{ox}})$ vs $[\text{R103QccNiR}]$ line (red) is $(2.6 \pm 0.1) \times 10^{-3} \text{ s}^{-1}$, identical within experimental error. These slopes have lower

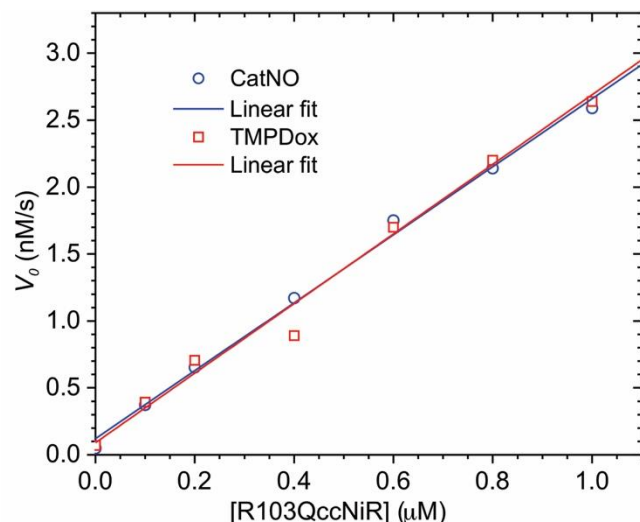


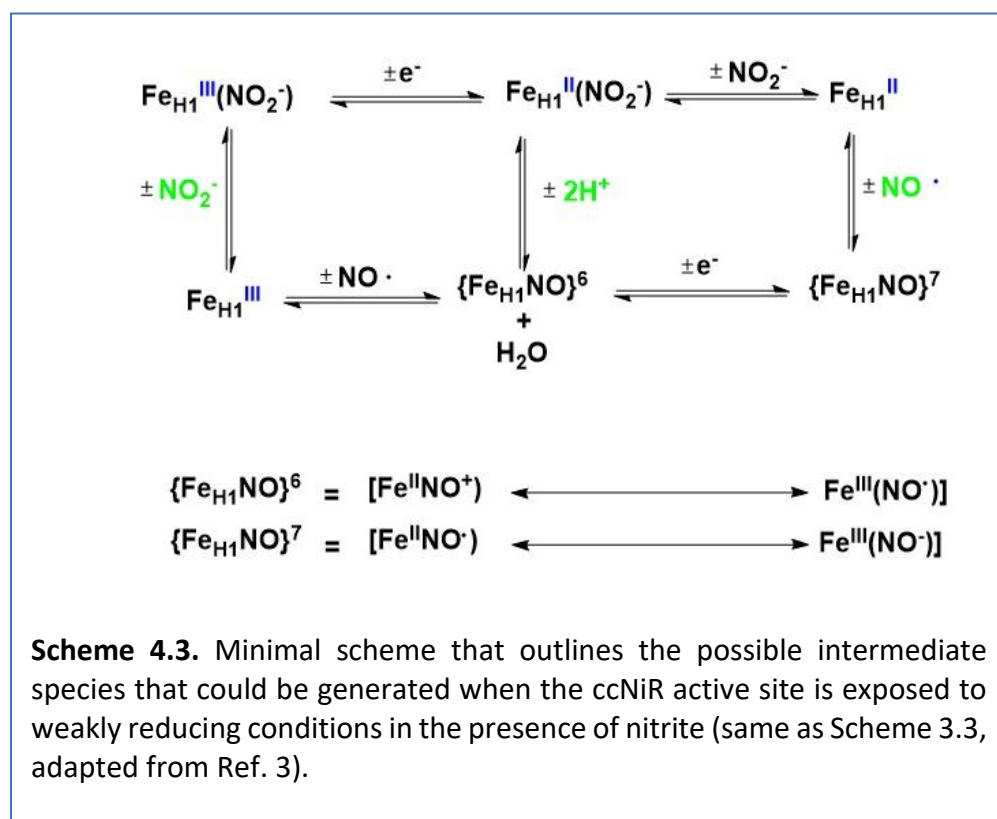
Figure 4.6. Blue circles: initial rate of CatNO formation vs R103QccNiR concentration; red squares: initial rate of TMPD_{ox} formation vs R103QccNiR concentration. The blue and red lines are the linear least-squares best fits to each data set. The data sets were collected at pH 7.0, with a nitrite concentration of 2 mM, a TMPD concentration of 1mM and a catalase concentration 4 μM . Blue line: slope = $(2.54 \pm 0.07) \times 10^{-3} \text{ s}^{-1}$, intercept = $(1.2 \pm 0.4) \times 10^{-10} \text{ M/s}$; red line: $(2.6 \pm 0.1) \times 10^{-3} \text{ s}^{-1}$, intercept = $(9 \pm 7) \times 10^{-11} \text{ M/s}$.

values than the one obtained in the absence of catalase ($(7 \pm 2) \times 10^{-3} \text{ s}^{-1}$, Fig. 4.3), but are within the same order of magnitude. Given the much lower scatter observed in Fig. 4.6, the values obtained from it probably provide the more reliable estimate of the apparent first-order rate constant, k_{app} , for R103Q-catalyzed reduction of nitrite to $\text{NO} \cdot$ by TMPD. As explained earlier, the scatter seen in Figs. 4.3-4.5 was probably due to higher than usual levels of oxygen in the glovebox when those experiments were performed. The y-intercepts of the $V_0(\text{CatNO})$ and $V_0(\text{TMPD}_{\text{ox}})$ vs $[\text{R103QccNiR}]$ lines were also much lower than those seen in Fig 4.3, $(1.2 \pm 0.4) \times 10^{-10} \text{ M/s}$ and $(9 \pm 7) \times 10^{-11} \text{ M/s}$, respectively, compared to $(2 \pm 2) \times 10^{-9} \text{ M/s}$ in Fig. 4.3. This is also consistent with background oxygen levels being much lower in the Fig. 4.6 data set. Presumably, in all cases, TMPD oxidation in the absence of enzyme was primarily due to

background oxygen, though a very small amount of NO· generation appears to also be taking place in the absence of enzyme, since the intercept of the $V_0(\text{CatNO})$ vs $[\text{R103QccNiR}]$ line in Fig. 4.6 is non-zero.

4.4. Discussion

The ccNiR-catalyzed production of free NO· from nitrite under weakly reducing conditions can be understood in terms of Scheme 3.3, which for convenience is reproduced below as Scheme 4.3. A detailed kinetic study of wtccNiR-catalyzed reduction of nitrite by



weak reductants, such as ferrocyanide or TMPD, showed that the nitrite-loaded active site, $\text{Fe}_{\text{H1}}^{\text{III}}(\text{NO}_2^-)$ in Scheme 4.3, is first reduced to $\text{Fe}_{\text{H1}}^{\text{II}}(\text{NO}_2^-)$, which was detectable in stopped-flow

experiments.⁴ The only other species that accumulated to detectable levels was the 2-electron reduced $\{\text{Fe}_{\text{H1}}\text{NO}\}^7$ moiety. However, the kinetic studies suggested that the majority of free $\text{NO}\cdot$ was most likely released from a transient $\{\text{Fe}_{\text{H1}}\text{NO}\}^6$, which never accumulates to detectable levels.⁴ In Scheme 4.3, $\text{Fe}_{\text{H1}}^{\text{II}}(\text{NO}_2^-)$ is first dehydrated to form $\{\text{Fe}_{\text{H1}}\text{NO}\}^6$, which can then either be reduced by 1-electron to generate $\{\text{Fe}_{\text{H1}}\text{NO}\}^7$ (right branch, Scheme 4.3), or release free $\text{NO}\cdot$ to regenerate the 5-coordinate ferric active site ($\text{Fe}_{\text{H1}}^{\text{III}}$), which then picks up nitrite to continue the cycle (left branch, Scheme 4.3). As shown on the right of Scheme 4.3, the kinetic studies of Shahid et al. provided strong evidence that $\{\text{Fe}_{\text{H1}}\text{NO}\}^7$ also releases free $\text{NO}\cdot$, which leaves a vacancy at the ferrous active site ($\text{Fe}_{\text{H1}}^{\text{II}}$) that can be filled by nitrite to produce $\text{Fe}_{\text{H1}}^{\text{II}}(\text{NO}_2^-)$.⁴ However, $\text{NO}\cdot$ release from $\{\text{Fe}_{\text{H1}}\text{NO}\}^7$ is much slower than release from the $\{\text{Fe}_{\text{H1}}\text{NO}\}^6$ transient: $k \sim 10^{-3} \text{ s}^{-1}$ compared to 0.05 s^{-1} .⁴

The spectropotentiometric studies of R103QccNiR presented in Chapter 3 appeared to show that the nitrite-loaded variant active site reduces at lower potentials than the nitrite-loaded wild type, and generates species that are spectroscopically distinct from the $\{\text{Fe}_{\text{H1}}\text{NO}\}^7$ produced in the wild type under equilibrium conditions.^{4, 9} Nevertheless, the results presented in this chapter show that free $\text{NO}\cdot$ can be produced when mixtures of nitrite and R103QccNiR are exposed to even the weak reductant, TMPD. The most likely source of free $\text{NO}\cdot$ is an $\{\text{Fe}_{\text{H1}}\text{NO}\}^6$ moiety, as extensive model studies have shown that $\{\text{Fe}_{\text{H1}}\text{NO}\}^6$ species are typically much more substitutionally labile than $\{\text{Fe}_{\text{H1}}\text{NO}\}^7$ ones.^{2, 10-15} It's possible that the heme-associated spectral component that appears during spectropotentiometric titration (Fig. 3.5), or during the catalytic reduction of nitrite to $\text{NO}\cdot$ by TMPD (Figs. 4.1 and 4.2), corresponds to formation of an $\{\text{Fe}_{\text{H1}}\text{NO}\}^6$ moiety. However, such a conjecture will need to be backed up by future studies using EPR or

other spectroscopic methods, and for now, the kinetic evidence appears to argue against it. The first-order rate constant for R103QccNiR-catalyzed $\text{NO}\cdot$ and TMPD_{ox} formation is $(2.6 \pm 0.1) \times 10^{-3} \text{ s}^{-1}$, provided by the slope of the Fig. 4.6 lines, which is about 20 \times lower than the rate constant attributed to $\text{NO}\cdot$ formation by release from wtccNiR $\{\text{Fe}_{\text{H1}}\text{NO}\}^6$.⁴ For the wild type case, the magnitude of the rate constant governing $\text{NO}\cdot$ release appears to be greatly influenced by the position of the equilibrium between $\text{Fe}_{\text{H1}}^{\text{II}}(\text{NO}_2^-)$ and $\{\text{Fe}_{\text{H1}}\text{NO}\}^6$, which must lie far in the direction of $\text{Fe}_{\text{H1}}^{\text{II}}(\text{NO}_2^-)$, since $\{\text{Fe}_{\text{H1}}\text{NO}\}^6$ is never detected.⁴ If the heme-associated spectral component that appears during spectropotentiometric titration (Fig. 3.5), or during the catalytic reduction of nitrite to $\text{NO}\cdot$ by TMPD (Figs. 4.1 and 4.2), corresponded to formation of a readily detectable, substitutionally labile $\{\text{Fe}_{\text{H1}}\text{NO}\}^6$ moiety, one would expect to see a larger, rather than a smaller, rate constant for $\text{NO}\cdot$ release, because it would indicate that the equilibrium between $\text{Fe}_{\text{H1}}^{\text{II}}(\text{NO}_2^-)$ and $\{\text{Fe}_{\text{H1}}\text{NO}\}^6$ now favors the latter species. Therefore, it appears more likely that the heme-associated spectral component that appears under weakly reducing conditions is not $\{\text{Fe}_{\text{H1}}\text{NO}\}^6$. Further studies of the reduced heme species will be presented in Chapter 5.

4.5. References

1. Einsle, O.; Messerschmidt, A.; Stach, P.; Bourenkov, G. P.; Bartunik, H. D.; Huber, R.; Kroneck, P. M. H., Structure of cytochrome c nitrite reductase. *Nature* **1999**, *400* (6743), 476-480.
2. Bamford, V. A.; Angove, H. C.; Seward, H. E.; Thomson, A. J.; Cole, J. A.; Butt, J. N.; Hemmings, A. M.; Richardson, D. J., Structure and spectroscopy of the periplasmic cytochrome c nitrite reductase from Escherichia coli. *Biochemistry* **2002**, *41* (9), 2921-2931.
3. Shahid, S. A mechanistic investigation of cytochrome c nitrite reductase catalyzed reduction of nitrite to ammonia: the search for catalytic intermediates. University of Wisconsin-Milwaukee, Milwaukee, WI, 2020.
4. Shahid, S.; Ali, M.; Legaspi-Humiston, D.; Wilcoxon, J.; Pacheco, A. A., A kinetic investigation of the early steps in cytochrome c nitrite reductase (ccNiR)-catalyzed reduction of nitrite. *Biochemistry* **2021**, *60*, 2098-2115.
5. Purwar, N.; McGarry, J. M.; Kostera, J.; Pacheco, A. A.; Schmidt, M., Interaction of nitric oxide with catalase: structural and kinetic analysis. *Biochemistry* **2011**, *50*, 4491-4503.

6. Koebke, K. J.; Pauly, D. J.; Lerner, L.; Liu, X.; Pacheco, A. A., Does the oxidation of nitric oxide by oxymyoglobin share an intermediate with the metmyoglobin-catalyzed isomerization of peroxynitrite? *Inorg. Chem.* **2013**, *52*, 7623-7632.
7. Koebke, K. J.; Waletzko, M. T.; Pacheco, A. A., Direct monitoring of the reaction between photochemically generated nitric oxide and *Mycobacterium tuberculosis* truncated hemoglobin N wild type and variant forms: an assessment of computational mechanistic predictions. *Biochemistry* **2016**, *55*, 686-696.
8. Ali, M. Probing the early steps in the catalytic reduction of nitrite to ammonia, catalyzed by cytochrome c nitrite reductase. University of Wisconsin-Milwaukee, Milwaukee, WI, 2019.
9. Ali, M.; Stein, N.; Mao, Y.; Shahid, S.; Schmidt, M.; Bennett, B.; Pacheco, A. A., Trapping of a putative intermediate in the cytochrome c nitrite reductase (ccNiR)-catalyzed reduction of nitrite: implications for the ccNiR reaction mechanism *J. Am. Chem. Soc.* **2019**, *141*, 13358-13371.
10. Hoshino, M.; Ozawa, K.; Seki, H.; Ford, P. C., Photochemistry of Nitric-Oxide Adducts of Water-Soluble Iron(III) Porphyrin and Ferrihemoproteins Studied by Nanosecond Laser Photolysis. *J. Am. Chem. Soc.* **1993**, *115* (21), 9568-9575.
11. Bohle, S. D.; Hung, C.-H., Ligand-promoted rapid nitric oxide dissociation from ferrous porphyrin nitrosyls. *J. Am. Chem. Soc.* **1995**, *117*, 9584-9585.
12. Ellison, M. K.; Scheidt, W. R., Synthesis, molecular structures, and properties of six-coordinate [Fe(OEP)(L)(NO)]⁺ derivatives: Elusive nitrosyl ferric porphyrins. *J. Am. Chem. Soc.* **1999**, *121* (22), 5210-5219.
13. Ali, M.S; A Unique Approach of Preparing 3,3-Disubstituted Oxindoles from Acyclic Tetrasubstituted Aldehydes: Total Synthesis of (-)-Coerulescine and (-)-Coixspirolactam A, Part B, Synthetic Scope of Brønsted Acid Catalyzed Reactions of Carbonyl Compounds and Ethyl Diazoacetate, university of wisconsin milwaukee, **(2021)**.
14. Hunt, A. P.; Lehnert, N., Heme nitrosyls: electronic structure implications for function in biology. *Acc. Chem. Res.* **2015**, *48*, 2117-2125.
15. Praneeth, V. K. K.; Paulat, F.; Berto, T. C.; De Beer George, S.; Nather, C.; Sulok, C. D.; Lehnert, N., Electronic structure of six-coordinate iron(III) - porphyrin NO adducts: the elusive iron (III) - NO(radical) state and its influence on the properties of these complexes. *J. Am. Chem. Soc.* **2008**, *130*, 15288-15303.

Chapter-5

Reactivity of Nitrite-Loaded R103QccNir with Hexaammineruthenium(II)

5.1. Overview

This chapter presents a kinetic study of the reactions that take place when nitrite-loaded R103Q ccNiR is mixed with hexaammineruthenium(II). With a midpoint potential of 50 mV vs SHE,¹ hexaammineruthenium(II) is a substantially weaker reducing agent than the MV_{red} used in the standard assay (Chapter 2), but also a significantly stronger reducing agent than TMPD (Chapter 4). With wild type ccNiR, even the weakest of reductants, such as TMPD or ferrocyanide, were able to reduce the enzyme active site to a $\{Fe_{H1}NO\}^7$ state.^{2, 3} When TMPD was used as the electron donor, a transient 1-electron reduced intermediate, likely $Fe_{H1}^{II}(NO_2^-)$, was also detected.³ The results presented in Chapter 4 provide no evidence for nitrite-loaded R103Q ccNiR reduction to either $\{Fe_{H1}NO\}^7$ or $Fe_{H1}^{II}(NO_2^-)$, presumably because the midpoint potential for the variant's heme 1 reduction is significantly lower than that of the wild type (Chapter 3). Nevertheless, R103Q ccNiR does catalyze reduction of nitrite by TMPD, and an as-yet unidentified reduced species accumulates very slowly, when the nitrite-loaded variant is exposed to TMPD (Chapter 4). The experiments presented in this chapter aimed to explore the changes at the nitrite-loaded active site under more strongly reducing conditions than those provided by TMPD.

5.2. Materials and methods

5.2.1. General materials

Hexaammineruthenium(III)chloride, sodium nitrite and D-glucose were purchased from Acros Organics, while HEPES free acid and its sodium salt were obtained from Thermo Fisher Scientific. Argon (high purity grade) was from AirGas. The R103Q ccNiR from *S. oneidensis* that was used in the experiments was purified as described in Chapter 2 and stored in millimolar aliquots at $-80\text{ }^{\circ}\text{C}$ until needed. Aliquots of frozen enzyme could be transferred through the glovebox antechamber, where they were thawed and diluted with degassed buffer (Section 4.2.1). Bovine liver catalase was purchased from Sigma-Aldrich and handled as described in Chapter 4.

5.2.2. Buffer and stock solution preparation.

Unless otherwise stated, all experiments were carried out in 50 mM HEPES buffer, pH=7. This was prepared in 300 mL batches and degassed by purging with argon for three hours in a Schlenk apparatus. After putting the apparatus under a slight vacuum, it was brought through the antechamber of the glovebox, at which point the degassed buffer was transferred to a capped bottle for storage. Stock solutions of D-glucose for the stopped-flow experiments, 0.1 M sodium nitrite, 10 mM hexaammineruthenium(III), and 60 μM R103Q ccNiR, were made inside the glovebox using the degassed HEPES buffer. The 10 mM hexaammineruthenium(III) solution was then reduced to hexaammineruthenium(II) by applying to it a potential using a potentiostat (Section 2.2); the extent of reduction was controlled by adjusting the applied potential.

5.2.3. Reduction of nitrite loaded R103Q ccNiR by hexaammineruthenium(II)

5.2.3.1. Long timescale kinetics experiments. Spectral changes that took place over a 60-minute time period after mixing nitrite-loaded R103Q with hexaammineruthenium(II) (hereafter referred to as “Ru^{II}”) were monitored by UV/Visible spectroscopy using a Cary 50 Bio spectrophotometer housed in a glovebox. Two sets of experiments were performed; the first set used pure Ru^{II}, the second 1:1 mixtures of Ru^{II} and hexaammineruthenium (III) (hereafter referred to as “Ru^{III}”). The mixture could be prepared either by mixing fully reduced and fully oxidized Ru, or by poisoning Ru^{III} at its midpoint potential with the potentiostat.

In a typical experiment, an aliquot of Ru^{II} stock was added to a cuvette already containing R103Q ccNiR and nitrite; the total solution volume was always 1 mL. The reagents were rapidly mixed using a cuvette mixer 68 (Fireflysci P68 mixer for semi-micro cuvettes), and data collection was immediately initiated. Spectra were collected every 15 s for 1 h in the range 300 nm - 800 nm (240 scans total). Data were collected in csv format and later analyzed by using programs written for Mathcad 15.0 (PTC Software) and Origin 9.0 (Microcal Software).^{4, 5} Experiment replicates were performed at varying Ru^{II}, nitrite, and R103Q ccNiR concentrations.

5.2.3.2. stopped-flow experiments. A single mixing SX-20 stopped-flow spectrophotometer (Applied Photophysics) was used to monitor the rapid kinetic changes that followed mixing of nitrite-loaded R103QccNiR with pure Ru^{II}. A mixture of 20 mM α -D-glucose and 200 U/mL *Aspergillus niger* glucose oxidase enzyme (MP biomedical) was used to scrub oxygen from the stopped-flow apparatus prior to use. Lyophilized glucose oxidase and glucose were dissolved in buffer inside the glovebox, and the solution was transferred to a tonometer

whose stopcocks and caps were greased with Apiezon M Economical High-Vacuum Lubricant. The sealed tonometer was removed from the glovebox and connected to one of the stopped-flow loading ports, from which both stopped flow syringes and the observation cell could subsequently be filled with the scrubbing solution, according to the instructions provided in the SX-20 manual. This solution was left in the stopped-flow overnight to make the system completely anaerobic, after which it was washed out with anaerobic 50 mM HEPES, pH=7.0 buffer, again following the SX-20 manual instructions. Stock reagent solutions were made in the glovebox as described previously in section 5.2.2. From these, one solution containing approximately 1 μ M R103ccNiR and 2 mM nitrite in 50 mM HEPES, pH = 7.0 was prepared and transferred into one tonometer, while 50 mM HEPES, pH = 7.0 solutions containing pure Ru^{II} were used to fill a second tonometer. A tonometer containing only buffer was also prepared in the glovebox, and the solution from this tonometer was used to wash out the glucose-glucose oxidase scrubbing solution (see above), and to blank the stopped-flow spectrophotometer. The tonometer containing nitrite-loaded R103QccNiR was used to fill one of the stopped-flow drive syringes, while the one containing the Ru^{II} solutions was used to fill the other. The solutions were mixed 1:1 by the stopped-flow drive piston. Each experiment was repeated at least four times; the first two datasets were typically discarded, and the third onward signal averaged. All the data were collected in photodiode array (PDA) mode. Data were collected in csv format and later analyzed by using programs written for Mathcad 15.0 (PTC Software) and Origin 9.0 (Microcal Software).³

5.3. Results

5.3.1. Reactivity of nitrite-loaded R103Q ccNiR with pure hexaammineruthenium(II) on the timescale of hours

Figure 5.1a shows the spectral changes observed after mixing 1.15 μM R103QccNiR with 4.7 mM nitrite and 1.0 mM pure Ru^{II} , in a pH 7 HEPES buffer. SVD analysis showed that three spectral components were needed to faithfully reconstruct a noise-reduced absorbance matrix. The SVD-treated data were then fit to Eq 5.1 using a global fitting routine (red traces, Fig.

$$A_{\lambda,t} = \Lambda_{0(\lambda)} + \Lambda_{1(\lambda)}f_1(t) + \Lambda_{2(\lambda)}f_2(t) \quad \text{Eq. 5.1a}$$

$$f_1(t) = \frac{k_{app1}}{k_{app2} - k_{app1}} \left[\exp(-k_{app1}t) - \exp(-k_{app2}t) \right] \quad \text{Eq. 5.1b}$$

$$f_2(t) = \frac{1}{k_{app2} - k_{app1}} \left\{ k_{app2} \left[1 - \exp(-k_{app1}t) \right] - k_{app1} \left[1 - \exp(-k_{app2}t) \right] \right\} \quad \text{Eq. 5.1c}$$

5.1a).^{4, 5} In Eq.5.1, $A_{\lambda,t}$ is the absorbance obtained at wavelength λ and time t , and $\Lambda_0 - \Lambda_2$ are the spectral components. Component Λ_0 is present at $t = 0$, Λ_1 grows in exponentially at a rate governed by k_{app1} and then decays exponentially at a rate governed by k_{app2} , and Λ_2 grows in as Λ_1 decays, at a rate governed by both k_{app1} and k_{app2} . Note that Λ_0 should decay exponentially as Λ_1 grows in, at a rate governed by k_{app1} . When Λ_0 is treated as a constant, Λ_1 and Λ_2 will appear as difference spectra. Figure 5.1b shows an absorbance vs. time slice from the Fig. 5.1a data set, obtained at 409 nm, which is the Soret maximum for R103Q ccniR. The blue trace is experimentally obtained, the red one is the least-squares best fit to Eq. 5.1.

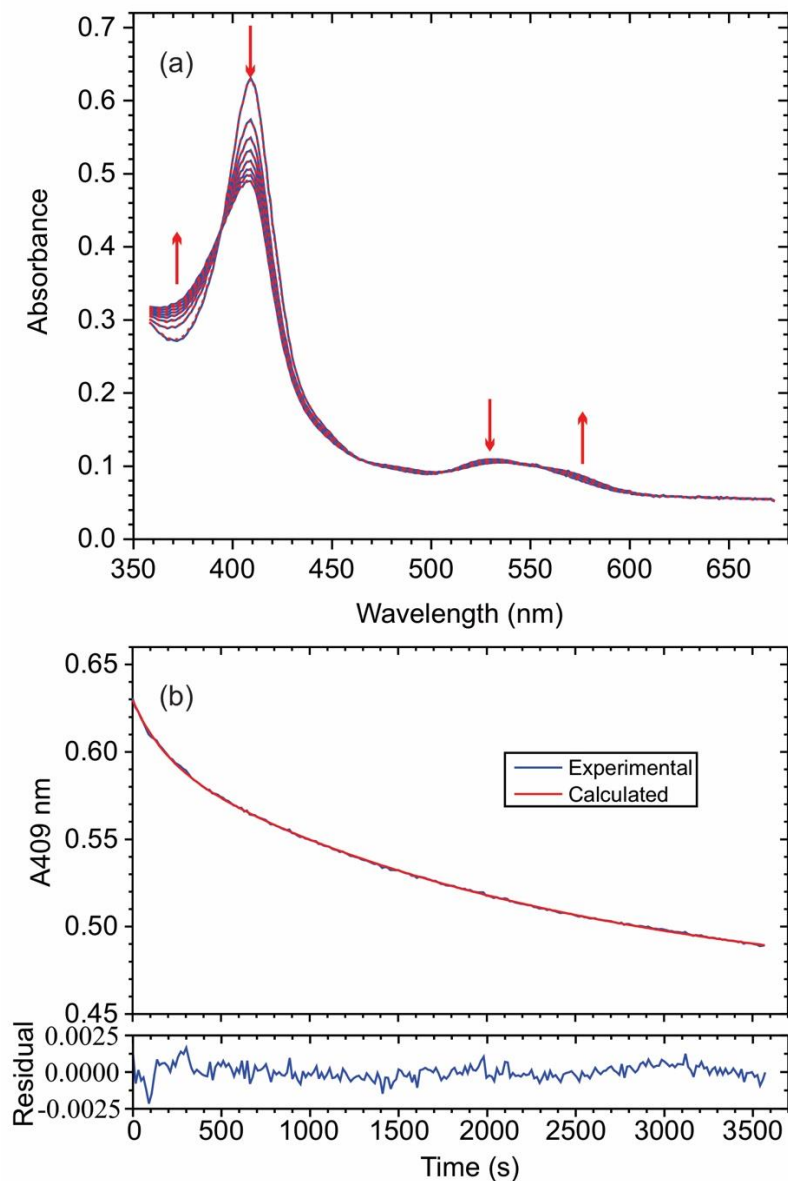


Figure 5.1. (a) Blue traces: UV/Vis spectral changes observed after mixing 1.15 μM R103QccNiR with 4.7 mM nitrite and 1.0 mM pure Ru^{II} , in a pH 7 HEPES buffer. Dashed red traces: least-squares best fit with Eq. 5.1. The reaction mixture was monitored at 15s intervals, but for clarity, the selected traces are at 600 s intervals. (b) Blue trace: absorbance vs. time slice taken at the 409 nm maximum of the data set above. Red trace: least-squares best fit with Eq. 5.1.

The blue trace in Fig. 5.2a shows the spectral component Λ_0 that was obtained by fitting the Fig. 5.1a data to Eq. 5.1. The component Λ_0 was in turn fit with the independently obtained extinction coefficient spectra of fully oxidized R103QccNiR (R103Q_{ox}) and nitrite; nitrite absorbs only slightly, and 1 mM Ru^{II} has negligible absorbance, in this wavelength range. The results of fitting Λ_0 in this experiment were very different from those seen when fitting data obtained from reduction of nitrite-loaded R103Q ccNiR with TMPD (Chapter 4, Fig. 4.2a). After mixing nitrite-loaded R103Q with TMPD, the spectrum obtained immediately after mixing was still well fit by the spectrum of R103Q_{ox}. On the other hand, the best fit of Λ_0 in Fig. 5.2a with the R103Q_{ox} extinction coefficient spectrum leaves a substantial residual spectrum (Fig. 5.2b), with absorbance increases at 423 nm and 551 nm, and a decrease at 402 nm, a pattern that is characteristic of low-spin c-heme reduction.^{6, 7} In our earlier studies of wtccNiR reduction by weak reductants in the presence of nitrite,^{2, 3} we found that the difference spectra obtained upon heme 1 active site reduction lacked the 551 nm peak but did exhibit the absorbance increase at 423 nm and decrease at 402 nm. The presence of the 551 nm peak in Fig. 5.2b therefore suggests that one of the bis-His ligated low-spin hemes (Fig. 1.2) was reduced within the mixing time. The highest-potential heme after heme 1 in wtccNiR is heme 4 (Fig. 1.2), so we tentatively ascribe the appearance of the 551 nm peak to reduction of heme 4 that takes place within the mixing time. Though reduction of nitrite-loaded heme 1 in wtccNiR doesn't generate a sharp 551 nm peak, it does result in a broad absorbance increase centered around 555 nm, both upon formation of the transient species $[\text{Fe}_{\text{H1}}^{\text{II}}(\text{NO}_2^-)]$,³ and upon formation of $\{\text{Fe}_{\text{H1}}\text{NO}\}$.^{7, 2} The residual Fig. 5.2b spectrum exhibits such a broad absorbance increase underlying the sharp

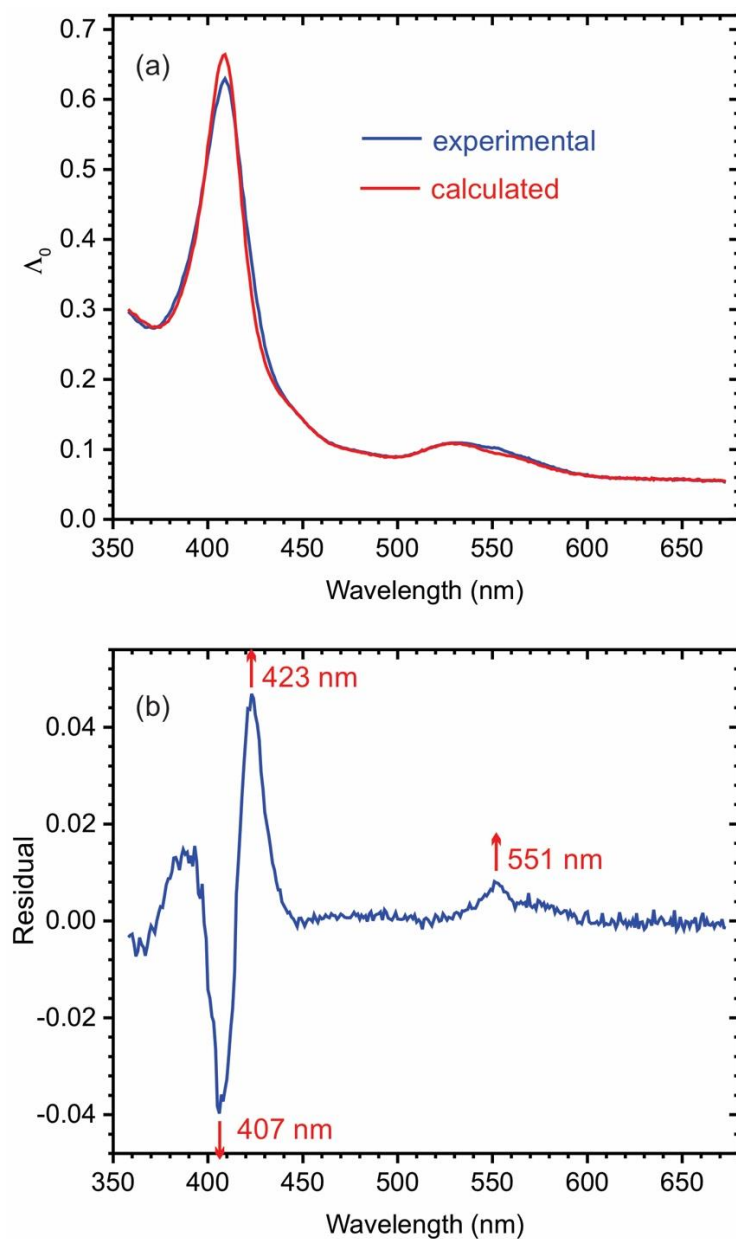


Figure 5.2. (a) Blue trace: spectral component Λ_0 generated by fitting the SVD-processed Fig. 5.1 data with Eq. 5.1. Red trace: least-squares best fit obtained using known extinction coefficient spectra of R103Q_{ox} and nitrite. (b) Difference spectrum obtained by subtracting the red spectrum in Fig. 5.2a from the blue one.

551 nm peak, which suggests that both heme 1 and heme 4 have been reduced within the mixing time and are contributing to the Λ_0 residual.

Figure 5.3 shows the spectral components (a) Λ_1 and (b) Λ_2 that were obtained by fitting the Fig. 5.1a data to Eq. 5.1. Λ_1 appears with a half-life of about two minutes, while Λ_2 appears with a half-life of about 30 minutes; neither half-life varies appreciably when the initial Ru^{II} concentration is varied from 200 μM – 1 mM (Fig. 5.4). The components have broadly similar appearances but exhibit notable small differences. Most importantly, Λ_1 has prominent negative peaks at 524 and 553 nm, together with a noticeable shoulder at 423 nm. These features, which are much less prominent in Λ_2 (the 423 shoulder is absent altogether), are diagnostic for bis-His ligated low-spin heme re-oxidation and show that the non-active site heme (likely heme 4) that reduces within the mixing time then re-oxidizes with a half-life of about two minutes. The main features in Λ_1 and Λ_2 are the absorbance increase at 375-380 nm and decrease at ~ 410 nm. The features probably indicate the formation of a common species and are spectrally distinct only because the features associated with bis-His coordinate low-spin heme re-oxidation mix into Λ_1 more than into Λ_2 . The amplitude of Λ_1 is only about a quarter that of Λ_2 . Notably, Λ_1 and Λ_2 are very reminiscent of the spectral components that were obtained in the spectropotentiometric titration of R103Q ccNiR described in Chapter 3 (Fig. 3.5), and also in the reaction of nitrite-loaded R103Q ccNiR with TMPD described in Chapter 4 (Fig. 4.1). The significance of this observation is discussed in Section 5.4.

Nitric oxide trapping studies using catalase (Section 4.3.2) showed that free $\text{NO}\cdot$ was generated when nitrite-loaded ccNiR was mixed with pure Ru^{II} . Figure 5.5 shows that the rate of

CatNO formation was linearly dependent on [R103Q ccNiR], at least up to 0.6 μM R103Q. The slope of the line is $(7.6 \pm 0.1) \times 10^{-3} \text{ s}^{-1}$, which is about $3\times$ higher than observed when TMPD is

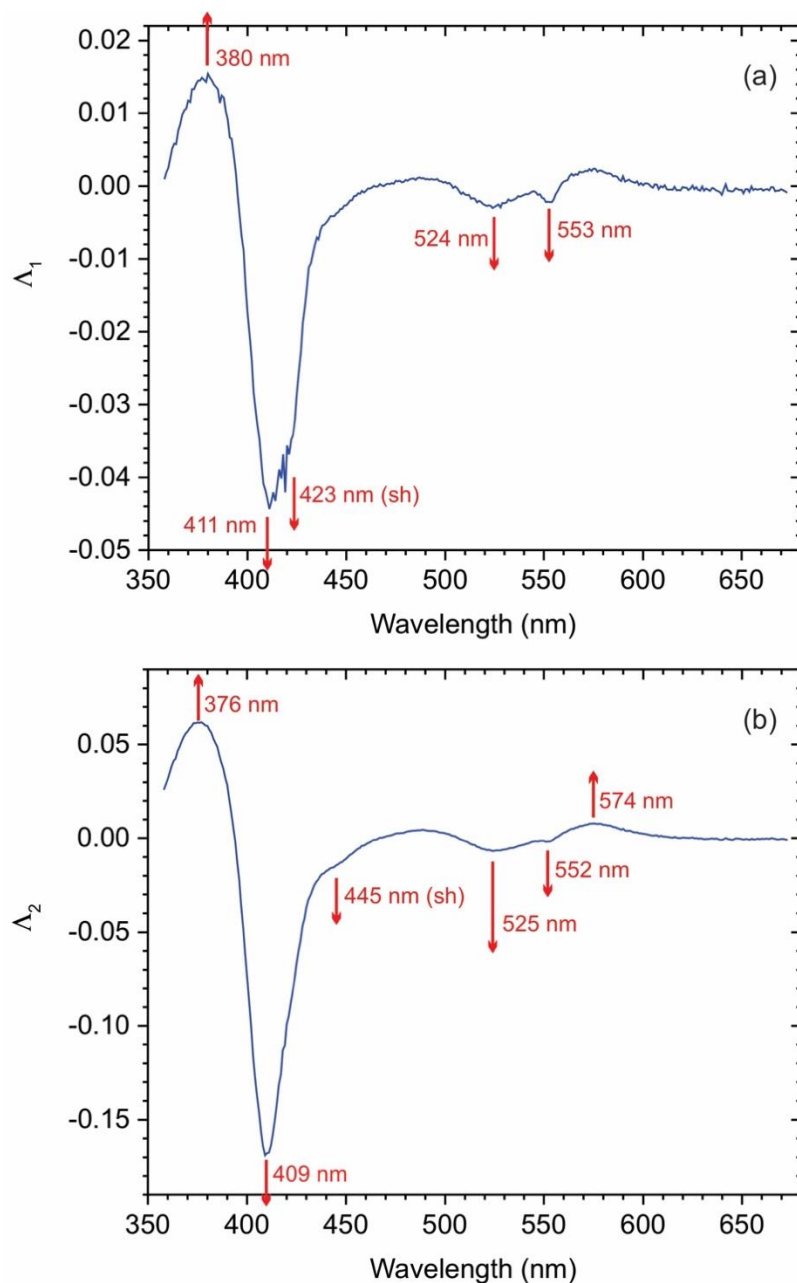


Figure 5.3. Spectral components (a) Λ_1 and (b) Λ_2 that were obtained by fitting the Fig. 5.1a data to Eq. 5.1.

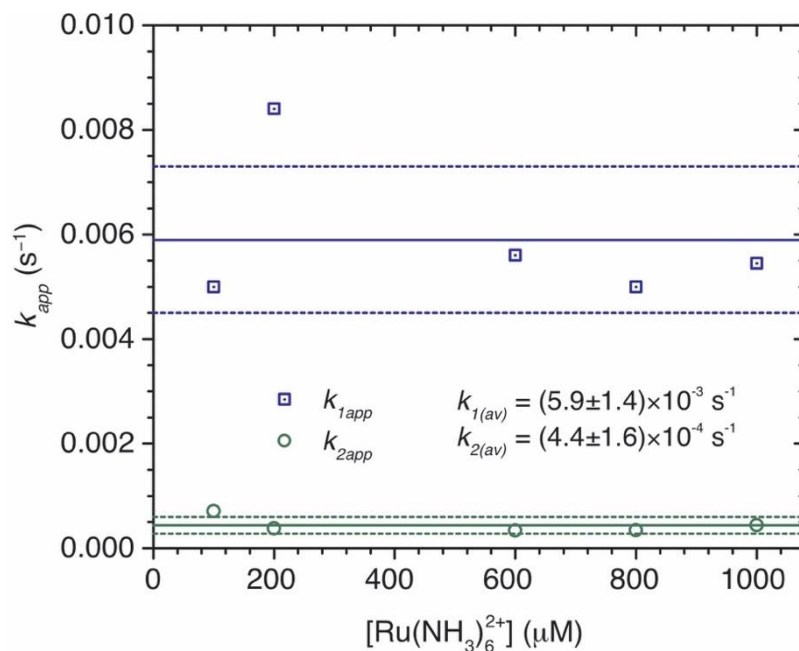


Figure 5.4. Dependence on $[\text{Ru}^{\text{II}}]$ of the k_{1app} and k_{2app} values obtained from fitting data like those of Fig. 5.1a to Eq. 5.1. In all cases, $[\text{NO}_2^-] = 2 \text{ mM}$ and $[\text{R103QccNiR}] \sim 1.2 \text{ } \mu\text{M}$.

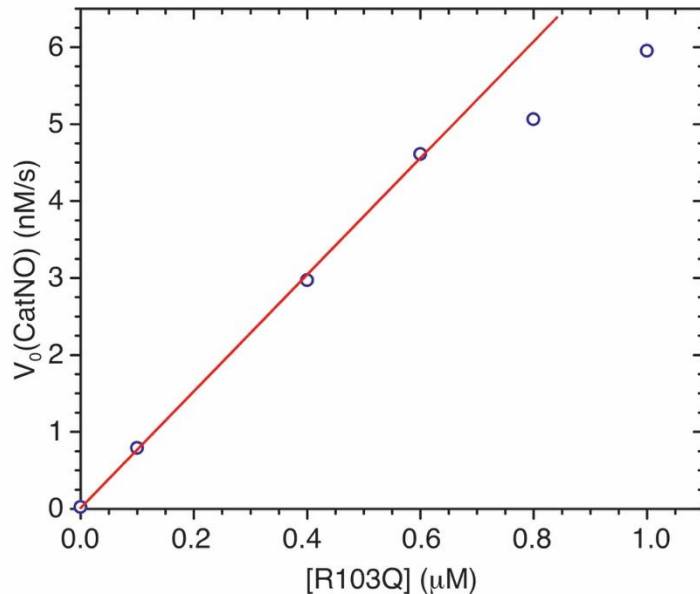


Figure 5.5. Blue circles: initial rate of CatNO formation vs R103QccNiR concentration; The red line is the linear least-squares best fit to the first four points of the data set (slope = $(7.6 \pm 0.1) \times 10^{-3} \text{ s}^{-1}$). The data set was collected at pH 7.0, with a nitrite concentration of 2 mM, a Ru^{II} concentration of 400 μM and a catalase concentration 4 μM .

the reductant $((2.54 \pm 0.07) \times 10^{-3} \text{ s}^{-1}$, Section 4.3.2). Thus, the rate of NO^\bullet formation is modestly higher when the stronger reductant is the electron source. In Fig. 5.5, the intercept is effectively zero $((1 \pm 5) \times 10^{-11} \text{ nM/s})$. Beyond $0.6 \text{ } \mu\text{M}$ R103Q, the dependence appears to deviate from linearity; however, this is probably an artifact. It appears that, at high R103Q concentrations, the rate of CatNO formation when pure Ru^{II} is the reductant becomes high enough that significant CatNO is formed during the mixing time, and consequently one is no longer measuring the initial rate of CatNO formation in these experiments.

5.3.2. Stopped-flow investigation of nitrite-loaded R103Q ccNiR's reactivity with pure hexaammineruthenium(II)

To study the fast reduction of nitrite-loaded R103Q ccNiR with pure Ru^{II} , a stopped-flow experiment was conducted with $\sim 1 \text{ } \mu\text{M}$ R103Q, 2 mM nitrite, and $400 \text{ } \mu\text{M}$ Ru^{II} . SVD analysis of time-resolved spectra collected during 1s- and 10s-intervals with the instrument in diode array mode showed that three spectral components were needed to faithfully reconstruct a noise-reduced absorbance matrix. The SVD-treated data were then fit to Eq 5.2 using a global fitting

$$A_{\lambda,t} = \Lambda_{3(\lambda)} + \Lambda_{4(\lambda)} f_1(t) + \Lambda_{5(\lambda)} f_2(t) \quad \text{Eq. 5.2a}$$

$$f_1(t) = \frac{k_{app3}}{k_{app4} - k_{app3}} \left[\exp(-k_{app3}t) - \exp(-k_{app4}t) \right] \quad \text{Eq. 5.2b}$$

$$f_2(t) = \frac{1}{k_{app4} - k_{app3}} \left\{ k_{app4} \left[1 - \exp(-k_{app3}t) \right] - k_{app3} \left[1 - \exp(-k_{app4}t) \right] \right\} \quad \text{Eq. 5.2c}$$

routine. Equation 5.2 is identical in form to Eq. 5.1, but the rate constants and spectral components are renamed to distinguish them from the components obtained by fitting the Fig. 5.1 spectra. The absolute time-resolved spectra obtained by stopped-flow are not shown here

because the differences between them are too small to be informative. However, Fig. 5.6 shows the absorbance changes seen at two representative wavelengths, 403 nm (blue traces) and 422 nm (green traces), together with the least-squares best fits at those wavelengths (red traces). These fits were obtained with the rate constants $k_{app3} = 34 \text{ s}^{-1}$ and $k_{app4} = 0.67 \text{ s}^{-1}$, which correspond to half-lives of 20 ms and 1s, respectively. Figure 5.7 shows the spectral component Λ_3 obtained by fitting the stopped-flow data with Eq. 5.2. According to the model, this is the spectrum present at $t = 0$, and it can be assigned to fully oxidized R103Q, showing that no significant heme reduction took place in the mixing time. Figure 5.8a shows the spectral component Λ_4 that grew in exponentially with a half-life of 20 ms. This component shows prominent positive signals at 552 nm and 525 nm; such signals are associated with reduction of ccNiR's bis-His ligated hemes but not of active site reduction.^{2,3,8} Therefore, it appears that a bis-His ligated heme, probably heme 4 (Section 5.3.1), is the first to be reduced when nitrite-loaded ccNiR is exposed to pure Ru^{II} . Figure 5.8b shows the spectral component Λ_5 that grew in exponentially with a half-life of 1s. This spectrum has prominent positive signals at 552 nm and 570 nm; further heme 4 reduction could be contributing to the 552 nm signal; however, taken together, the 552 nm and 570 nm signals form a pattern similar to the one that was rapidly generated when nitrite-loaded wild type ccNiR was reduced by TMPD in stopped-flow experiments.³ In those experiments, the pattern-generating species was tentatively assigned as the 1-electron reduced heme 1 with nitrite bound, $\text{Fe}_{\text{H1}}^{\text{II}}(\text{NO}_2^-)$.³ The negative signals at 401nm-403nm, and the positive ones at 422nm, in Figs. 8a and 8b, are diagnostic of c-heme reduction of either the ccNiR active site or of one of the bis-His ligated hemes.^{3,9} Thus, it appears that, when nitrite-loaded ccNiR is exposed to pure Ru^{II} , heme 4 is first reduced on the millisecond timescale,

after which the active site is reduced with a half-life of about 1s, probably to generate the 1-electron reduced species $\text{Fe}_{\text{H1}}^{\text{II}}(\text{NO}_2^-)$. Reduction of the active site may or may not be accompanied by further reduction of heme 4.

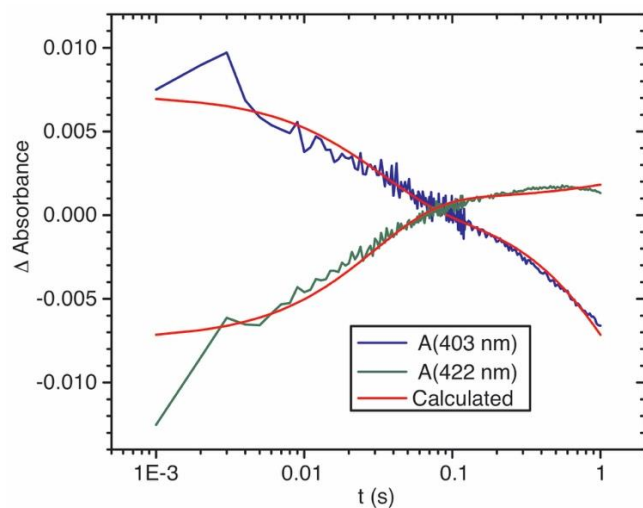


Figure 5.6. Spectral changes seen at 403 nm (blue trace) and 422 nm green trace upon mixing $\sim 1 \mu\text{M}$ R103Q ccniR, 2 mM nitrite, and 400 μM Ru^{II} . Red traces: least-squares fit of the data to Eq. 5.2.

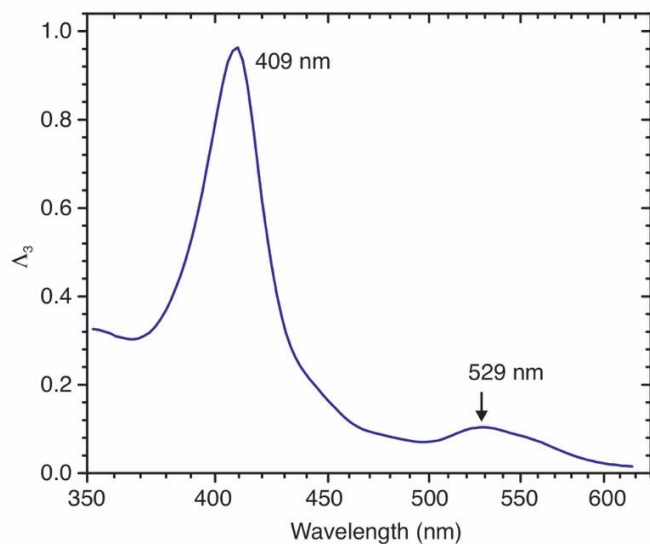


Figure 5.7. Spectral component Λ_3 generated by fitting the SVD-processed stopped-flow data with Eq. 5.2. According to the Eq. 5.2 model, this component represents the spectrum present at $t = 0$.

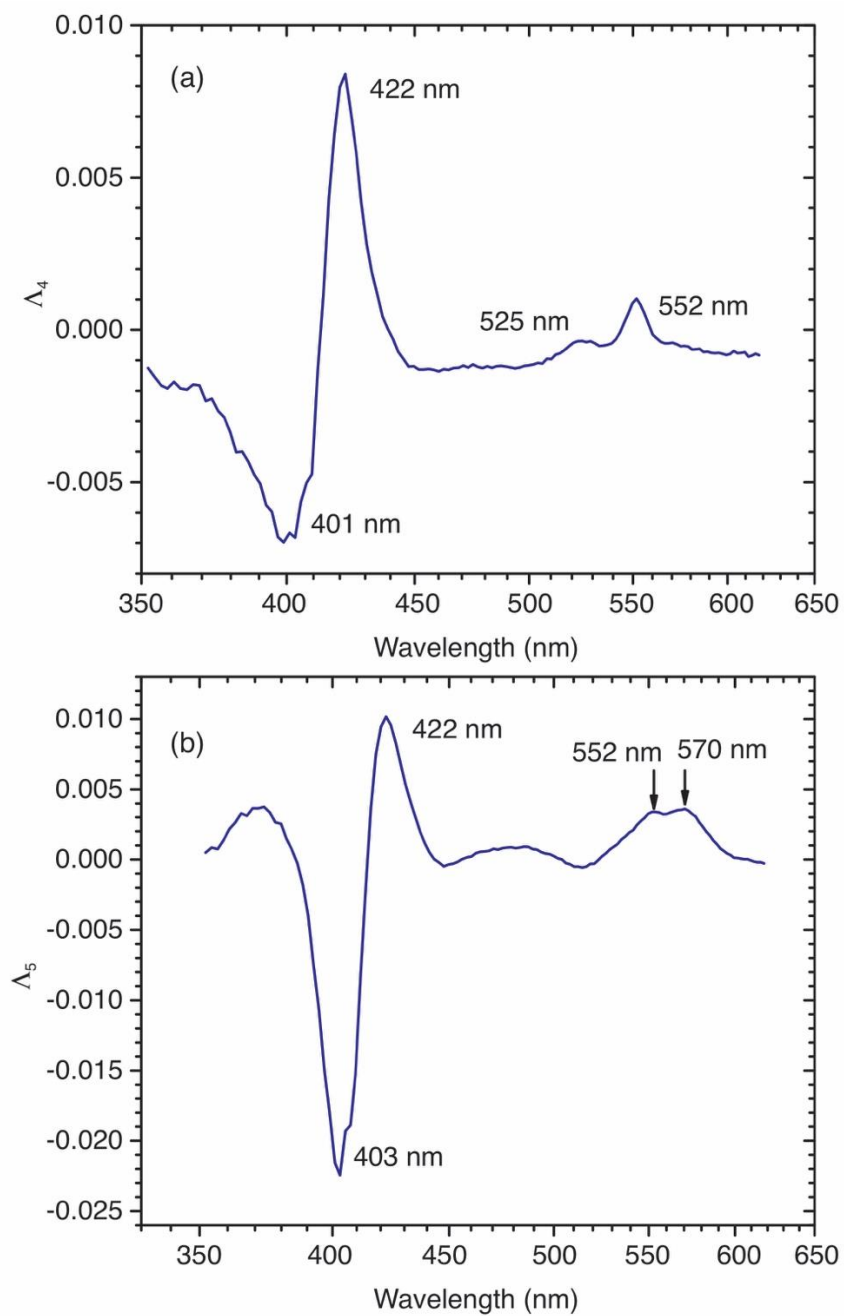


Figure 5.8. Spectral components (a) Λ_4 and (b) Λ_5 that were obtained by fitting the stopped-flow data to Eq. 5.2. The component Λ_4 grew in with a half-life of about 20 ms, while Λ_5 grew in with a half-life of about 1s.

5.3.3. Reactivity of nitrite-loaded R103Q ccNiR with 1:1 Ru^{II}:Ru^{III} on the timescale of hours

Figure 5.9a shows the spectral changes observed after mixing 1.6 μ M R103QccNiR with 2 mM nitrite and a 1:1 mixture of Ru^{II}:Ru^{III} (600 μ M total ruthenium) in a pH 7 HEPES buffer. The Ru^{II}:Ru^{III} mixture was generated electrochemically by applying a potential of 50 mV vs SHE to a stock solution of Ru^{III} (50 mV is the midpoint potential for Ru^{III} reduction). SVD analysis showed that only two spectral components were needed to faithfully reconstruct a noise-reduced absorbance matrix. The SVD-treated data were then fit to Eq 5.3 using a global fitting routine (red traces, Fig. 5.9a).^{4, 5} In Eq.5.3, $A_{\lambda,t}$ is the absorbance obtained at wavelength λ and

$$A_{\lambda,t} = \Lambda_{6(\lambda)} + \Lambda_{7(\lambda)} [1 - \exp(-k_{app5}t)] \quad \text{Eq. 5.3}$$

time t , Λ_6 is the spectral component present at $t = 0$, and Λ_7 is a spectral component that grows in exponentially at a rate governed by k_{app5} . Note that Λ_6 should decay exponentially as Λ_7 grows in, at a rate governed by k_{app5} . As before, when Λ_6 is treated as a constant, Λ_7 will appear as a difference spectrum. Figure 5.9b shows an absorbance vs. time slice from the Fig. 5.9a data set, obtained at 409 nm, the Soret maximum for R103Q ccNiR. The blue trace is experimentally obtained, the red one is the least-squares best fit to Eq. 5.3.

The blue trace in Fig. 5.10 shows the spectral component Λ_6 generated by fitting the SVD-processed Fig. 5.9 data with Eq. 5.3, while the dashed red trace is the least-squares best fit obtained using known extinction coefficient spectra of R103Q_{ox} and nitrite. In contrast to the Λ_0 obtained when nitrite-loaded R103Q was reduced with pure Ru^{II} (Fig. 5.2), the fit of the Fig. 5.10 Λ_6 with R103Q_{ox} and nitrite is excellent, showing that no appreciable heme reduction takes place in the mixing time (10 – 50 s). In the Fig. 5.1 experiment, pure Ru^{II} was able to rapidly

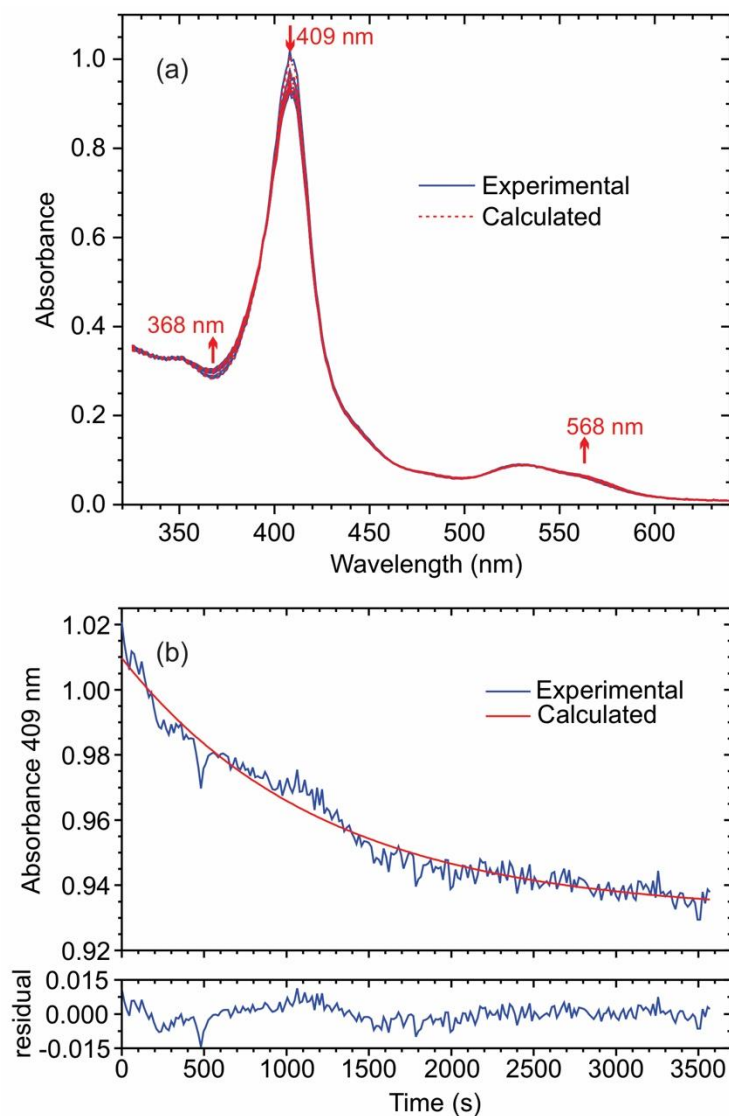


Figure 5.9. (a) Blue traces: UV/Vis spectral changes observed after mixing 1.6 μM R103QccNiR with 2 mM nitrite and a 1:1 mixture of $\text{Ru}^{\text{II}}:\text{Ru}^{\text{III}}$ (600 μM total ruthenium) in a pH 7 HEPES buffer. Dashed red traces: least-squares best fit with Eq. 5.3. The reaction mixture was monitored at 15s intervals, but for clarity, the selected traces are at 600 s intervals. (b) Blue trace: absorbance vs. time slice taken at the 409 nm maximum of the data set above. Red trace: least-squares best fit with Eq. 5.3.

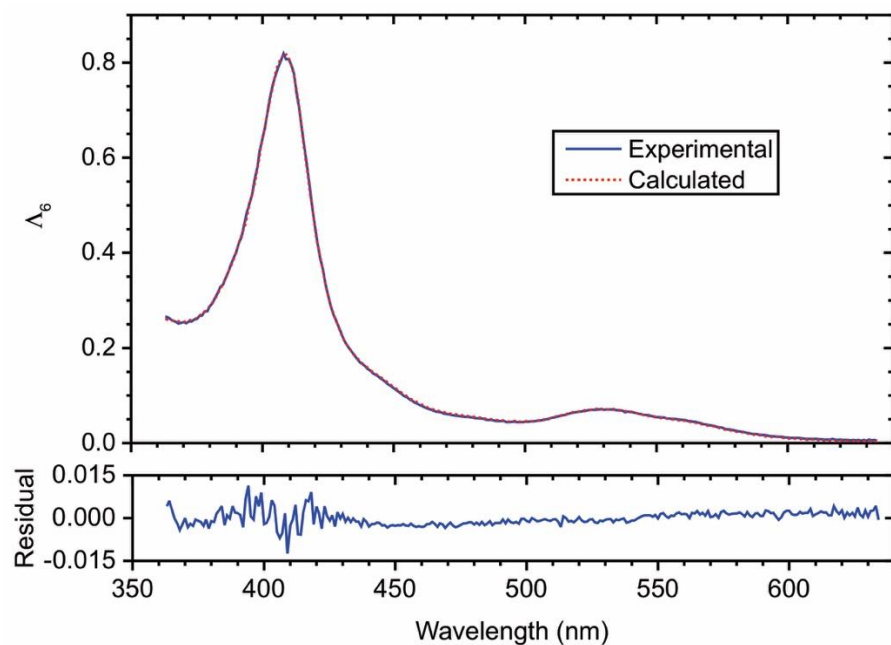


Figure 5.10. Blue trace: spectral component Λ_6 generated by fitting the SVD-processed Fig. 5.9 data with Eq. 5.3. Dashed red trace: least-squares best fit obtained using known extinction coefficient spectra of R103Q_{ox} and nitrite.

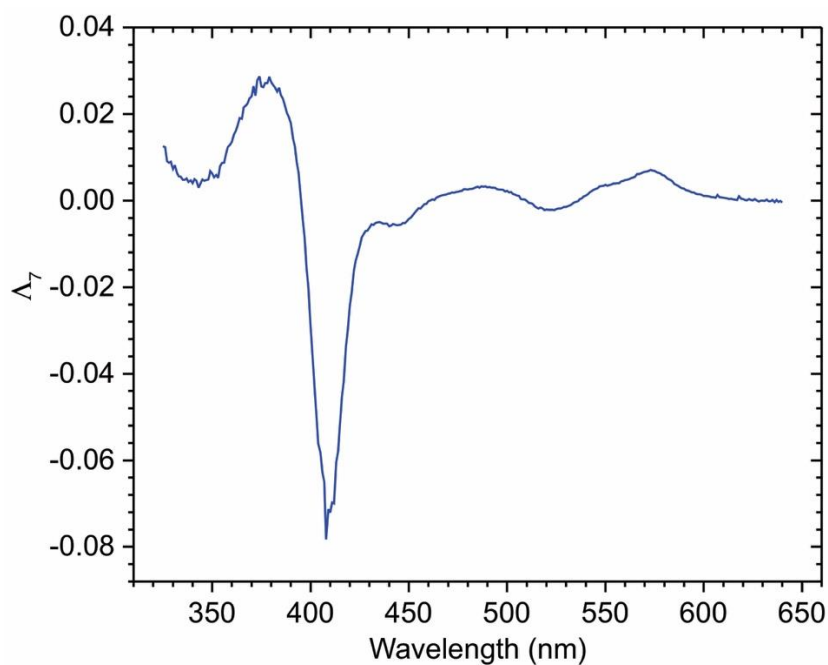


Figure 5.11. Spectral component Λ_7 generated by fitting the SVD-processed Fig. 5.9 data with Eq. 5.3. Note the similarity to Λ_2 in Fig. 5.3, the spectrum obtained at infinite time when nitrite-loaded R103Q ccNiR was reduced with pure Ru^{II}.

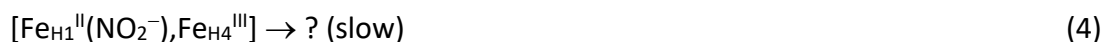
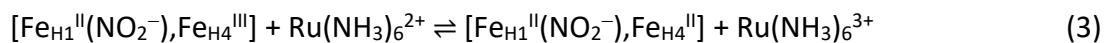
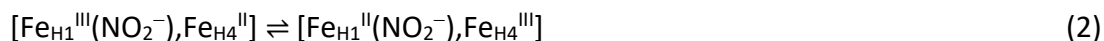
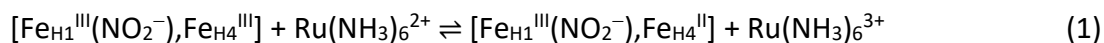
reduce a 6-coordinate bis-his ligated low-spin heme, probably heme 4, which has the second-highest midpoint potential after the active site heme (about -100 mV vs SHE).⁹ This in turn seemed to facilitate active site heme reduction, as evidenced by the broad absorbance band underlying the sharp 551 nm band in the Λ_0 spectrum of Fig. 5.2.^{2,3} The 1:1 Ru^{II}:Ru^{III} mixture of the Fig. 5.9 experiment poises the solution at +50 mV vs SHE, and at this higher potential, heme 4 reduction is inaccessible, which in turn appears to have made fast active site heme reduction inaccessible.

Fig. 5.11 shows the spectral component Λ_7 generated by fitting the SVD-processed Fig. 5.9 data with Eq. 5.3. This component is identical in its essential features to Λ_2 generated by fitting the Fig. 5.1 data, obtained when nitrite-loaded R103Q ccNiR was reduced with pure Ru^{II}, to Eq. 5.1. The only notable difference between Figs. 5.11 and 5.3b is the absence of a 551 nm feature in Fig. 5.11, which is consistent with there having been no initial heme 4 reduction when the enzyme is reduced in a 1:1 mixture of Ru^{II} and Ru^{III}. Furthermore, the Fig. 5.11 spectral component also appears to be the same or very similar to the one seen when nitrite-loaded R103Q ccNiR is exposed to the weak reductant TMPD for an hour (Chapter 4, Fig. 4.2), or in spectropotentiometric titrations of nitrite loaded R103Q ccNiR (Chapter 3, Fig. 3.4), or even in spectropotentiometric titrations of a different variant, H257Q ccNiR.¹⁰ This is a very important observation that will be discussed in Section 5.4.

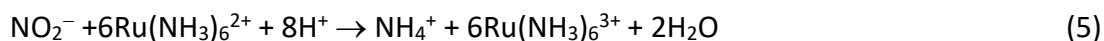
5.4. Discussion

Scheme 5.1 outlines a minimal mechanism proposed to explain the observed reactivity of nitrite-loaded R103Q ccNiR with Ru^{II} that was presented in this chapter. The first three steps are the fast ones that were monitored in the stopped flow experiments (Section 5.3.2, Figs. 5.6-5.8). Initially, heme 4 is reduced by Ru^{II} on the millisecond timescale (Scheme 5.1, step 1), probably establishing a rapid equilibrium. On a slower timescale ($t_{0.5} \sim 1s$), heme 1 is reduced by intramolecular electron transfer from heme 4 (Scheme 5.1, Step 2), which allows further reduction of heme 4 to generate a 2-electron reduced intermediate (Scheme 5.1, Step 3). Steps 1-3 can take place only when pure Ru^{II} is used as the electron donor. When Ru^{II} is mixed 1:1 with Ru^{III} (Section 5.3.3), neither heme 1 nor heme 4 is initially reduced. Presumably, this is because the Ru^{III} shifts equilibria 1 and 3 in Scheme 5.1 to the left.

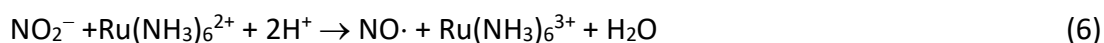
Reduction of R103Q ccNiR:



Possibly catalyzed by 2-electron reduced R103Q ccNiR:



Possibly catalyzed by both 1- and 2-electron reduced R103QccNiR:



Scheme 5.1. Minimal mechanism proposed to explain the reactivity of nitrite-loaded R103Q ccNiR with Ru^{II}. Fe_{H1} refers to active site heme 1 and Fe_{H4} to heme 4 (Fig. 1.2b)

Over a longer timescale ($t_{0.5} \sim 2$ min) heme 4 re-oxidizes, as evidenced by the disappearance of the diagnostic signals at 524 nm and 553 nm in Fig. 5.3a (Section 5.3.1). This re-oxidation probably tracks catalytic oxidation of Ru^{II} to Ru^{III} by nitrite. The NO^\cdot trapping experiments (Figs. 4.6 and 5.5) show that reduced R103Q ccNiR can catalyze reduction of nitrite to NO^\cdot by Ru^{II} (Scheme 5.1, Step 5), but it is also possible that, at high $\text{Ru}^{\text{II}}:\text{Ru}^{\text{III}}$ concentration ratios, the two-electron reduced $[\text{Fe}_{\text{H1}}^{\text{II}}(\text{NO}_2^-), \text{Fe}_{\text{H4}}^{\text{II}}]$ species can catalyze the 6-electron reduction of nitrite to ammonia (Scheme 5.1, Step 6). As Ru^{II} is oxidized to Ru^{III} , equilibria 1 and 3 in Scheme 5.1 shift to the left.

Finally, on a very long timescale ($t_{0.5} \sim 30$ min), reduced R103Q ccNiR is converted to the as-yet uncharacterized form with the spectrum seen in Figs. 5.3 and 5.11 (Scheme 5.1, Step 4). This species is only generated under reducing conditions in the presence of nitrite; however, they need not be strongly reducing conditions. The same species or one very like it was generated when the applied potential was 0.05 V vs SHE (1:1 $\text{Ru}^{\text{II}}:\text{Ru}^{\text{III}}$, Fig. 5.11), and even when the reducing agent was TMPD ($\mathcal{E}_m = 0.26$ V vs SHE, Fig. 4.1).

The fact that nitrite-loaded R103Q heme 1 reduces so much more slowly than heme 4 suggests that there is a kinetic barrier to heme 1 reduction that is not seen for the wild type. Stopped-flow studies of the reaction between nitrite-loaded wild type ccNiR and TMPD showed that even a weak reductant like TMPD rapidly and directly reduced the nitrite-loaded heme 1, first to $\text{Fe}_{\text{H1}}^{\text{II}}(\text{NO}_2^-)$, and then to the 2-electron reduced $\{\text{Fe}_{\text{H1}}\text{NO}\}^7$ form.³ Even when pure Ru^{II} is used as a reductant, there is no evidence of heme 4 reducing before nitrite-loaded heme 1 in wtccNiR (David Koltermann, personal communication). A possible explanation, supported by

crystallographic evidence,¹¹ and by the theoretical studies of Bykov and Neese,¹² is that R103 helps to orient the bound nitrite in the position optimal for subsequent heme reduction.

The results presented in this chapter and in Chapter 4 force a re-interpretation of the spectropotentiometric results presented in Chapter 3, and also of the analogous results reported earlier for nitrite-loaded H257Q ccNiR,¹⁰ as well as still unreported spectropotentiometric results for nitrite-loaded Y206F ccNiR (Steven Reinhardt, personal communication). All three spectropotentiometric experiments generated species with difference spectra that looked very similar to the ones seen in Figs. 5.3 and 5.11, which appeared to be formed in 1-electron reduction steps (see for example Fig. 3.4). However, given how slowly the species with the Fig. 5.3 and 5.11 spectral characteristics are formed, it now seems likely that equilibrium was never achieved during the spectropotentiometric titrations, and that the observed spectral changes were partially or wholly under kinetic control.

It's striking that species with the Fig. 5.3 and 5.11 spectral characteristics are generated for all three active site variants (R103Q, H257Q, Y206F) under mildly reducing conditions in the presence of nitrite, and yet such a species is never seen when the nitrite-loaded wild type is exposed to mildly reducing conditions. One reasonable conjecture is that the species is a side product that lies off the catalytic pathway; indeed, it may be that one of the essential functions of the residues R103, H257, and Y206, acting in concert, is to prevent the formation of this species. EPR and other spectroscopic studies of the species with the Fig. 5.3 and 5.11 spectral characteristics are planned for the near future, and in the longer term, it may be possible to characterize the species crystallographically as well.

5.5. References

1. Hong, S. L.; Barclay, D. J.; Anson, F. C., Formal potentials and cyclic voltammetry of some ruthenium ammine complexes. *Inorg. Chem.* **1972**, *11*, 1460-1466.
2. Ali, M.; Stein, N.; Mao, Y.; Shahid, S.; Schmidt, M.; Bennett, B.; Pacheco, A. A., Trapping of a putative intermediate in the cytochrome c nitrite reductase (ccNiR)-catalyzed reduction of nitrite: implications for the ccNiR reaction mechanism *J. Am. Chem. Soc.* **2019**, *141*, 13358-13371.
3. Shahid, S.; Ali, M.; Legaspi-Humiston, D.; Wilcoxon, J.; Pacheco, A. A., A kinetic investigation of the early steps in cytochrome c nitrite reductase (ccNiR)-catalyzed reduction of nitrite. *Biochemistry* **2021**, *60*, 2098-2115.
4. Koebke, K. J.; Pauly, D. J.; Lerner, L.; Liu, X.; Pacheco, A. A., Does the oxidation of nitric oxide by oxymyoglobin share an intermediate with the metmyoglobin-catalyzed isomerization of peroxynitrite? *Inorg. Chem.* **2013**, *52*, 7623-7632.
5. Koebke, K. J.; Waletzko, M. T.; Pacheco, A. A., Direct monitoring of the reaction between photochemically generated nitric oxide and *Mycobacterium tuberculosis* truncated hemoglobin N wild type and variant forms: an assessment of computational mechanistic predictions. *Biochemistry* **2016**, *55*, 686-696.
6. Arciero, D. M.; Balny, C.; Hooper, A. B., Spectroscopic and Rapid Kinetic-Studies of Reduction of Cytochrome-C554 by Hydroxylamine Oxidoreductase from *Nitrosomonas-Europaea*. *Biochemistry* **1991**, *30* (48), 11466-11472.
7. Marritt, S. J.; Kemp, G. L.; Xiaoe, L.; Durrant, J. R.; Cheesman, M. R.; Butt, J. N., Spectroelectrochemical characterization of a pentaheme cytochrome in solution and as electrocatalytically active films on nanocrystalline metal-oxide electrodes. *J. Am. Chem. Soc.* **2008**, *130*, 8588-8589.
8. Lehnert, N.; Coruzzi, G.; Hegg, E.; Seefeldt, L.; Stein, L. Feeding the world in the 21st century: grand challenges in the nitrogen cycle.
9. Stein, N.; Love, D.; Judd, E. T.; Elliott, S. J.; Bennett, B.; Pacheco, A. A., Correlations between the electronic properties of *Shewanella oneidensis* cytochrome c nitrite reductase (ccNiR) and its structure: effects of heme oxidation state and active site ligation. *Biochemistry* **2015**, *54*, 3749-3758.
10. Shahid, S. A mechanistic investigation of cytochrome c nitrite reductase catalyzed reduction of nitrite to ammonia: the search for catalytic intermediates. University of Wisconsin-Milwaukee, Milwaukee, WI, 2020.
11. Einsle, O.; Messerschmidt, A.; Huber, R.; Kroneck, P. M. H.; Neese, F., Mechanism of the six-electron reduction of nitrite to ammonia by cytochrome c nitrite reductase. *J. Am. Chem. Soc.* **2002**, *124* (39), 11737-11745.
12. Bykov, D.; Neese, F., Substrate binding and activation in the active site of cytochrome c nitrite reductase: a density functional study. *J. Biol. Inorg. Chem* **2011**, *16*, 417-430.

Chapter 6

Conclusions and Suggestions for Further Study

The results presented in this thesis provide several important clues about the functional role of the conserved active site amino acid R103 in *S. oneidensis* ccNiR. The results from Chapter 2 show that, under standard assay conditions which use the strong reducing agent methyl viologen monocation radical (MV_{red}) as an electron source, activity of the R103Q ccNiR variant is only 20% that of the wild type for both nitrite and hydroxylamine reduction. By contrast, for the H257Q ccNiR variant studied earlier by Shahid,¹ the MV_{red} turnover rate was found to be almost zero when nitrite was the electron acceptor but comparable to that of the wild type when reducing hydroxylamine. A species formally containing hydroxylamine bound to the heme 1 active site has long been proposed as a catalytic intermediate (Scheme 1.3),^{2, 3} and our group has previously proposed the final 2-electron reduction that formally converts hydroxylamine to ammonia to be rate limiting in ccNiR-catalyzed reduction of nitrite to ammonia (Scheme 1.4).⁴⁻⁶ The fact that nitrite- and hydroxylamine reduction by MV_{red} are attenuated by the same amount in the R103Q variant suggests that loss of R103 is disrupting the final 2-electron reduction. On the other hand, loss of H257 appears to affect the early stages in nitrite reduction almost exclusively because nitrite reductase activity almost disappears in H257Q whereas hydroxylamine reductase activity is largely unaffected.¹

Nitrite-loaded R103Q ccNiR's behavior under weakly reducing conditions differs substantially from that of the wild type, though it is still capable of catalyzing reduction of nitrite to nitric oxide when TMPD (Chapter 4) or hexaammineruthenium(II) (Chapter 5) is the electron

donor. The nitric oxide turnover rate is higher when the stronger Ru^{II} reductant is used, but only by ~3×; in either case the rate of free nitric oxide formation is low, as it is in the wild type.

Regardless of the weak reductant used, a reduced R103Q ccNiR species with a characteristic UV/Vis absorbance spectrum is generated in an exponential process, with a half-life of 30 minutes, in the presence of nitrite. Interestingly, a species with a very similar UV/Vis spectrum is seen when nitrite-loaded H257Q is reduced under mild conditions.¹ On the other hand, when the nitrite-loaded wild type ccNiR is reduced under mild conditions (applied potentials above 0 mV vs SHE), the nitrite-loaded active site is converted to a species that has been identified as the 2-electron reduced {Fe_{H1}NO}⁷; this species has a substantially different UV/Vis spectrum from that obtained when R103Q or H257Q are reduced. We conjecture that the species generated upon reduction of R103Q or H257Q lies off the catalytic pathway, and that R103, H257, and possibly Y206, all conserved active site residues, act in concert to prevent the formation of this species. Indeed, this may be one of the key functions of these residues. EPR and other spectroscopic studies of the putative dead-end enzyme species are planned for the near future.

When 400 μM pure Ru^{II} was used as the electron donor to reduce nitrite-loaded R103Q ccNiR, a UV/Vis stopped-flow study showed that one of the bis-His ligated low-spin hemes (Fig. 1.2) was reduced with a half-life of about 20 ms and before the active site. The reduced heme is probably heme 4, which in wild type ccNiR has the second-highest midpoint potential after the active site.⁸ Active-site reduction took place over 1 – 5 s ($t_{0.5}$ ~1s), and appeared to be mediated by heme 4 (Scheme 5.1, Chapter 5). We tentatively assign the reduced active site species to be [Fe_{H1}^{II}(NO₂⁻)]; that is, a ferrous heme with nitrite as axial ligand (Scheme 5.1). Importantly, the

fact that nitrite-loaded R103Q heme 1 reduces so much more slowly than heme 4 suggests that there is a kinetic barrier to heme 1 reduction that is not seen for the wild type. Stopped-flow studies of the reaction between nitrite-loaded wild type ccNiR and TMPD showed that even a weak reductant like TMPD rapidly and directly reduced the nitrite-loaded heme 1, first to $\text{Fe}_{\text{H1}}^{\text{II}}(\text{NO}_2^-)$, and then to the 2-electron reduced $\{\text{Fe}_{\text{H1}}\text{NO}\}^7$ form.⁶ Even when pure Ru^{II} is used as a reductant, there is no evidence of heme 4 reducing before nitrite-loaded heme 1 in wtccNiR (David Koltermann, personal communication). A possible explanation, supported by crystallographic evidence,² and by the theoretical studies of Bykov and Neese,⁹ is that R103 helps to orient the bound nitrite in the position optimal for subsequent heme reduction.

Over a longer timescale ($t_{0.5} \sim 2$ min) heme 4 re-oxidized, as evidenced by the disappearance of signals diagnostic of bis-his heme reduction (Fig. 5.3a, Chapter 5). We propose that this re-oxidation tracks catalytic oxidation of Ru^{II} to Ru^{III} by nitrite, which concomitantly forms nitric oxide, ammonia, or both (Scheme 5.1, Chapter 5). As mentioned above, the reduced active site slowly ($t_{0.5} \sim 30$ min) converts to a spectroscopically distinct species that is not observed for the wild type enzyme. This species is generated even under very weakly reducing conditions (with TMPD or 1:1 $\text{Ru}^{\text{II}}:\text{Ru}^{\text{III}}$ mixtures as electron donors) where no bis-His ligated heme reduction is observed (Chapters 4 and 5).

The top priority in future studies will be the identification by spectroscopic or crystallographic methods of the putative off-path intermediate that forms when nitrite loaded R103Q (and probably H257Q) is exposed to weak reductants. Identifying this species is likely to provide insight into one of the functions of R103 in the enzyme active site. A systematic stopped-flow study of the reaction between nitrite-loaded R103Q and pure Ru^{II} could also be very

informative. The current study used a single Ru^{II} concentration (400 μM) which generated a relatively small amount of the transient 1-electron reduced species [Fe_{H1}^{III}(NO₂⁻), Fe_{H4}^{II}] (Scheme 5.1, Chapter 5). It is likely that the heme 4 reduction rate is first-order in [Ru^{II}], in which case it may be possible to generate a higher concentration of the 1-electron reduced species at higher Ru^{II} concentrations. Then, the 1-electron reduced species could be trapped using the rapid freeze-quench method and studied by EPR spectroscopy. Previous EPR-spectropotentiometric studies of wtccNiR by our group showed that hemes 1, 3, and 4 interact magnetically in a complicated way, such that the characteristic spectrum of isolated heme 3 is not observed until both hemes 1 and 4 have been reduced.⁸ A rapid-freeze quench experiment in which heme 4 was reduced to a diamagnetic ferrous state would allow the interaction between hemes 1 and 3 to be studied in isolation, something that is not possible under equilibrium conditions where heme 4 reduces after heme 1.

References

1. Shahid, S. A mechanistic investigation of cytochrome c nitrite reductase catalyzed reduction of nitrite to ammonia: the search for catalytic intermediates. University of Wisconsin-Milwaukee, Milwaukee, WI, 2020.
2. Einsle, O.; Messerschmidt, A.; Huber, R.; Kroneck, P. M. H.; Neese, F., Mechanism of the six-electron reduction of nitrite to ammonia by cytochrome c nitrite reductase. *J. Am. Chem. Soc.* **2002**, *124* (39), 11737-11745.
3. Bykov, D.; Plog, M.; Neese, F., Heme-bound nitroxyl, hydroxylamine, and ammonia ligands as intermediates in the reaction cycle of cytochrome c nitrite reductase: a theoretical study. *J. Biol. Inorg. Chem.* **2014**, *19*, 97-112.
4. Youngblut, M.; Pauly, D. J.; Stein, N.; Walters, D.; Conrad, J. A.; Moran, G. R.; Bennett, B.; Pacheco, A. A., *Shewanella oneidensis* cytochrome c nitrite reductase (ccNiR) does not disproportionate hydroxylamine to ammonia and nitrite, despite a strongly favorable driving force. *Biochemistry* **2014**, *53*, 2136-2144.
5. Ali, M.; Stein, N.; Mao, Y.; Shahid, S.; Schmidt, M.; Bennett, B.; Pacheco, A. A., Trapping of a putative intermediate in the cytochrome c nitrite reductase (ccNiR)-catalyzed reduction of nitrite: implications for the ccNiR reaction mechanism *J. Am. Chem. Soc.* **2019**, *141*, 13358-13371.
6. Shahid, S.; Ali, M.; Legaspi-Humiston, D.; Wilcoxon, J.; Pacheco, A. A., A kinetic investigation of the early steps in cytochrome c nitrite reductase (ccNiR)-catalyzed reduction of nitrite. *Biochemistry* **2021**, *60*, 2098-2115.
7. Enemark, J. H.; Feltham, R. D., Principles of Structure, Bonding and Reactivity for Metal Nitrosyl Complexes. *Coord. Chem. Rev.* **1974**, *13*, 339-406.
8. Stein, N.; Love, D.; Judd, E. T.; Elliott, S. J.; Bennett, B.; Pacheco, A. A., Correlations between the electronic properties of *Shewanella oneidensis* cytochrome c nitrite reductase (ccNiR) and its structure: effects of heme oxidation state and active site ligation. *Biochemistry* **2015**, *54*, 3749-3758.
9. Bykov, D.; Neese, F., Substrate binding and activation in the active site of cytochrome c nitrite reductase: a density functional study. *J. Biol. Inorg. Chem* **2011**, *16*, 417-430.

Curriculum Vitae

SHAHAMA ALAM

Summary

- Five years of experience working in diverse areas of chemical Biology, bioinorganic enzymology, and bio-analytical Chemistry; that include, but not limited to, enzyme characterization, protein purification and crystallization, bio-catalytic organic transformation, bio-conjugation.
- Expert in cell and enzyme-based assays (e. g. colorimetric assay), cell culture, bioanalytical techniques, small molecular docking in enzyme, computational modeling of enzyme kinetics (e.g., initial rate calculation) and electrochemistry.
- Ability to multitask effectively in handling high-pressure work situations and proven competency to work as a team player.

Education:

- Ph.D. in Biological Inorganic Chemistry and structural biology, University of Wisconsin Milwaukee, WI, USA, under the supervision of **Prof. Arsenio Andrew Pacheco**
May 2022
- MS in Applied Chemistry & Chemical Engineering; University of Dhaka, Bangladesh
2011
- BS in Applied Chemistry & Chemical Engineering; University of Dhaka, Bangladesh
2010

Research and Teaching Experience

1. Designed and executed extensive Spectro-potentiometric experiments to characterize cytochrome c nitrite reductase (ccNiR), and to trap putative intermediates of ccNiR-catalyzed nitrite reduction.
2. Performed steady-state kinetics analysis of ccNiR-catalyzed nitrite reduction by weak reducing agents.
3. Site directed mutation of cytochrome c nitrite reductase (ccNiR) enzyme and gene expression in *Shewanella Oneidensis* bacteria & New Mechanistic insight of R103Q ccNiR.
4. Highly experienced in Protein purification, Process scale chromatography and filtration process, (Tangential flow filtration (TFF) & formal flow filtration), Flow Cytometry etc.
5. Experienced Operating, maintaining, and troubleshooting chromatography workstations, process scale up, and technology transfer Knowledge and working in a cGMP environment.
6. Hands on experience at Cyclic voltammetry, Mass Spectroscopy, Liquid Chromatography, Protein HPLC (SEC, Ion exchange chromatography, RP), NMR, UV-Vis, GC.
7. Capable of process sample independently and analyze samples
8. Good expertise at data management, problem solving and data processing & writing analytical method and validation report, machine troubleshooting & Good Documentation practices (GDP)
9. Supervised undergraduate researchers handling instruments and doing research projects

10. Graduate Teaching & Research Assistant, Lab technicians UWM. Experience in both General and Biochemistry

Technical Skills

Gene expression and cloning • Large scale bacterial cell culture (45L) of *S. Oneidensis* for bulk protein purification • Chromosomal and plasmid DNA extraction and DNA sequencing • Site directed mutation of active site of enzyme • Real time polymerase chain reaction (RT-PCR), Process scale chromatography Filtration,

Biochemistry Skills

• Protein purification large scale (50L) • Design kinetic and assay model • Molecular biology assay • ELISA,

Pyridine Hemochromagen Assay • Hydrophobic Interaction, Affinity chromatography/ Size Exclusion chromatography • Column packing, preparation and regeneration, Tangential flow filtration • Northern/ Western/ Southern Blot, Gel electrophoresis, • Bioinformatics for new protein characterization and drug target optimization and immunohistochemical staining.

Analytical Skills

Specialized Instrumentation: LC-MS, GC-MS, NMR (Nuclear Magnetic Resonance), HPLC, FPLC, fluorescence spectroscopy, Flow cytometry, colony picker, UV-Vis, time-resolved UV-Vis Spectroscopy, EPR Spectro-potentiometry, stopped-flow (XS20 Applied Photo physics), LASER-initiated time-resolved UV-Vis spectroscopy, ultra-and high-speed centrifuges, Schlenk Line System, BASI- Electrochemical Analyzers, oxygen-free glove boxes (MBraun) for handling air-sensitive enzymes.

Software Skills

Protein molecule visualization system (PyMol), Mathcad and MATLAB, Origin 8/9, CorelDRAW, UNICORN™ 7 Software based on AKTA pure system, Cary Win UV Software, Pro-Data View/ SX (Applied Photo-physics) analyzing stopped-flow spectral based Kinetics, SPSS-Statistical Analysis, SAS etc.

Conference and Seminar Presentation

• Shahama Alam, A. Andrew Pacheco; 'Probing the Mechanism Cytochrome c Nitrite Reductase Enzyme and Its Variants' On the preceding of Midwest enzyme conference October 2021.

• Shahama Alam, A. Andrew Pacheco; 'New Mechanistic Insight of Cytochrome c Nitrite Reductase Enzyme' On the preceding of Midwest Enzyme Chemistry Conference, Illinois Institute of Technology, October 2020.

•Shahama Alam, A. Andrew Pacheco; 'Probing the Mechanism Cytochrome c Nitrite Reductase Enzyme and Its Variants under weak reducing Agent' On the preceding of University of Wisconsin Milwaukee, Chemistry and Biochemistry Symposium (May 2021).

Publications

1. Shahama Alam, A. Andrew Pacheco, J Wilcoxon, "The effects of an R103Q mutation on the chemical and physical properties of the enzyme cytochrome c nitrite reductase (ccNiR)" Manuscript on preparation.
2. Shahama Alam, Steven Reinhardt, Shahid Shahid, A. Andrew Pacheco, J Wilcoxon, "Trapping an intermediate for the enzyme cytochrome c Nitrite reductase (ccNiR) variant R103Q, H257Q, Y206F in presence of weak reducing agent" Manuscript on preparation.

Training

1. Chemical disposal training,
2. Bio safety training

Scholarships/Awards

- UWM (University of Wisconsin Milwaukee) Chancellor Fellowship Award (Spring, 2017-present)

References: Available upon request